Dislocation Dynamics for High Strain-Rate Plasticity: Inertial and Thermal Effects

by

Eleanor Y. K. Mak

A thesis
presented to the University of Waterloo
in fulfillment of the
thesis requirement for the degree of
Master of Applied Science
in
Civil Engineering

Waterloo, Ontario, Canada, 2017

I hereby declare that I am the sole author of this thesis. This is a true copy of the thesis, including any required final revisions, as accepted by my examiners.

I understand that my thesis may be made electronically available to the public.

Abstract

There has been a trend of miniaturization in recent technological advances, particularly through the development of microelectromechanical systems (MEMS). To cope with the demand for increasing performance from ever smaller components, alternatives to traditional scaling techniques is required, for example, by exploiting scale-dependent material properties. The investigation of material behaviour through computer simulations is an attractive alternative to experimental techniques which are limited by scale and cost.

Metallic crystalline solids are commonly the material of choice for MEMS components. The majority of a metal's capacity for deformation is irreversible, otherwise known as *plasticity*. The dislocation – a defect in the crystal structure at the atomic level – acts as the microscopic carrier of plasticity. The Discrete Dislocation Dynamics (DD) family of numerical models serves as a bridge between an atomistic and a continuum description of plasticity at the mesoscale. In continuum models, plasticity is captured through the homogenization of localized effects induced by dislocation activity. With DD models, the activity of discrete dislocations is instead explicitly simulated. Conventional DD models are purely mechanical and are based on a quasi-static formulation. For the purpose of high strain-rate loading scenarios, they fail to capture the localized thermal effects which emerge, as well as the inertial effects which are particularly relevant. As such, the fully Dynamic and coupled Thermo-Mechanical Dislocation Dynamics model (DTM-DD) was developed in this thesis to address the limitations of existing DD models in the context of high strain-rate plasticity. Inertia was included via an elastodynamic description of material behaviour and the consideration of dislocation mass; and thermal influences, through thermo-mechanical coupling and the temperature dependence of dislocation parameters.

Using the DTM-DD, the high strain-rate plastic behaviour of metals was investigated. The interaction and interference of elastic waves was observed; and the implications and convergence of dynamic dislocation motion was determined. The framework of extension load testing was presented to investigate the influence and strain-rate sensitivity of system and dislocation parameters to inertial and thermal effects. The selection of the thermal boundary condition was identified to significantly influence the simulated material response. The nature of temperature dependence, as investigated through parameter studies of dislocation drag and nucleation strength, was shown to be a competition between influences causing material softening and hardening. The DTM-DD was extended to investigate the effect of loading rate on the nano-indentation of a thin film sample. Loading rate-dependent propagation of dislocation nucleation and slip as a plastic front was observed. Ultimately, the investigations using the DTM-DD demonstrate that the interplay between inertial and thermal effects are highly complex in a fully dynamic and thermo-coupled system.

Acknowledgements

With the completion of this thesis, it is already time for this chapter to close and another to open. This thesis would not have been possible without the many individuals who have encouraged me along the way. I would like to express my appreciation for the care and support that was provided to me.

First and foremost, I would like to thank my research supervisor Dr. Robert Gracie for his continued guidance and invaluable technical insight through the course of this degree. I am particularly grateful for his confidence in my abilities, and for the independence I was given to freely explore, learn, and ask questions; all of which, I believe, has made me a much better researcher today.

Next, I wish to thank to my colleagues Endrina Rivas and Mike Yetisir for their support (and antics) both in and outside of research. As well, additional thanks to my friends from undergraduate who have been alongside me for the ride: Brian Jo, Stanley Fong, Kyle Balkos, Adam Morrison, and Ryan Barrage. Graduate school has its ups and downs, but it always helps to have the best of friends at your side.

Furthermore, my thanks to Ernst Remij for his words of encouragement.

Finally, I would like to thank my loving family for their unwavering support all this time.

Table of Contents

List of Tables

List of Figures

Chapter 1

Introduction

Within the last few decades of research in materials science, a significant paradigm shift has occurred: the focus of contemporary research has shifted from pure experimentalism to focus on computer simulations [1]. This is not a surprise given the trend of miniaturization in recent technological advances. Progress in computational simulation techniques has advanced hand-in-hand with the explosive growth in the research and development of microelectromechanical systems (MEMS) [2]. MEMS, and more recently nano-systems (NEMS), are ubiquitous in the engineered technology which pervade our everyday lives. Their use is widespread, with applications in the automotive industry, biomedical technologies, and the development of consumer electronics, to name just a few. In the drive towards continued miniaturization, it is no longer feasible to continue with only traditional scaling techniques, i.e. simply making components smaller. Rather, it is necessary to address the properties of the materials being used themselves, for example, to exploit scale-dependent material properties, or even the realization of novel materials with engineered scale-dependent characteristics [3]. Due to the scale of the engineering problem as well as increasing costs, computer simulations for virtual testing and design are an attractive alternative to traditional experimental techniques. As such, materials modeling naturally arises from the need to understand material behaviour. The development of an accurate and realistic simulation tool with predictive capacity is requisite to establish the theory behind, as well as comprehensively characterize, material behaviour.

Metallic crystalline solids (metals) possess highly desired thermal, mechanical, or electrical attributes; hence their prevalence in MEMS components. The focus of the research presented in this thesis is to understand the behaviour of metals through the development of computer models. To fully characterize the behaviour of a material requires an understanding of both the reversible elastic, and the irreversible inelastic – otherwise known as

plastic – behaviour. For metals in particular, elastic behaviour is expressed only for small deformations. In this way, linear elasticity theory describes a small fraction of a metal's capacity for deformation; and plasticity, the remaining majority.

Plasticity theory arose from the study of metals in the late 19^{th} century. First, through experimental trials by Tresca in 1864; then followed by development of yield criteria and flow rules by Saint-Venant, Levy, Von Mises, Hencky, and Prandtl [4]. By the mid-1940s, Prager, Hill, Drucker, and Koiter among others, united plasticity under a single comprehensive framework of the classical theory established through macroscopic investigations [4]. In parallel, beginning with Volterra in 1907, Taylor, Orowan, Polanyi, and finally codified by Hirth and Lothe [5] in their seminal book entitled "Theory of Dislocations", studied the role of dislocations – defects in the crystal structure at the atomic level – as the microscopic carrier of crystal plasticity [6].

The creation of, by the words of Van der Giessen [7], an "ultimate theory of plasticity" requires the treatment of plasticity at multiple scales. In numerical simulation, each characteristic spatial and temporal scale requires a different type of model (Fig. 1.1). The behaviour of an individual dislocation is captured at the atomic level through Molecular Dynamic (MD) simulations. Moving up to the continuum mesoscale, dislocation mechanisms, the interactions of hundreds to thousands of dislocations, are explicitly modeled in Discrete Dislocation Dynamics (DD) simulations. Alternatively, the influence of a collective of dislocations is homogenized at the continuum scale, forming continuum mechanics-based (CM) crystal plasticity models. Crystal plasticity then scales to macroscopic phenomenological models by recognizing that metals are simply an aggregate of grains, or a polycrystal; and the scale transition is a further homogenization from the continuum level [8].

A multi-scale approach to plasticity requires understanding of scale-specific behaviour, scale-dependent material properties, and the multiphysical phenoma which arise at each characteristic length scale [8]. As the size and physical time of simulations have increased due to improvements in the performance of numerical methods and computing power, the length- and time-scales of the three previously independent model types (MD, DD, and CM) now overlap [9].

The greatest challenge in unifying the size-scale transitions along this spectrum of plasticity models remains at the scale of DD, where discrete dislocation effects are significant but the relevant length- and time-scales are too large for MD simulation [9]. DD provides a framework to explicitly simulate the motion and interaction of dislocations at the mesoscale. Ideally, parameters of a DD model would be derived from a fundamental description of atomic structure via MD. DD then allows for the bridging between the atomistic and the continuum descriptions of plasticity by providing the quantitative input for the

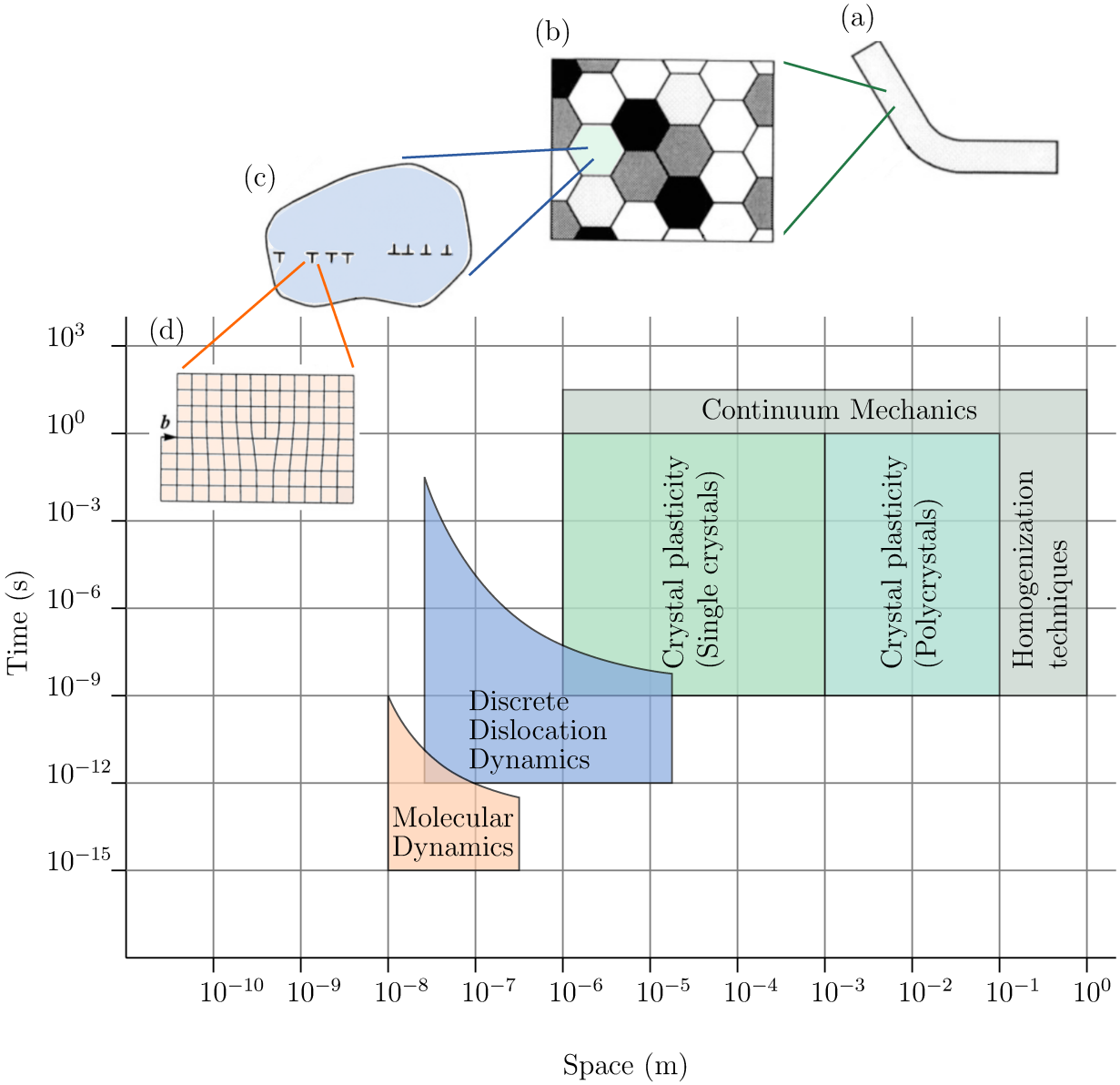

Figure 1.1: Spectrum of characteristic spatial and temporal scales of plasticity models: (a) macroscopic, (b) crystal plasticity, (c) discrete dislocation plasticity (mesoscale), and (d) atomistic. Adapted from [8, 9].

phenomenological constitutive rules in crystal plasticity (CM).

A wide variety of DD models have been developed to date to investigate the response of metals under loading [10]. In experimental trials, ex. by [11,12], material response was observed to transition from loading rate – specifically, strain-rate – independent to dependent behaviour as loading rate was increased. Multiphysical phenomena that are not apparent at lower rates, for example localized temperature increase and thermal softening due to dislocation motion, emerge during this transition and increase the complexity of material behaviour [6]. As such, simulations to date tend to overestimate material strength. Furthermore, as the loading rate is increased, inertial considerations are required to accurately capture the finite traveling time of elastic waves propagating through a medium.

Conventional DD models neglect both thermal and inertial considerations as they are typically purely mechanical, and the term "dynamics" in Dislocation Dynamics refers to the time evolution of the dislocation structure as opposed to elastodynamics. Attempts have been made to address the elastodynamics of the high strain-rate plasticity problem but neglect thermal effects, ex. by [13–15]. Conversely, the Thermo-Mechanically coupled DD model (TM-DD) introduced by [6] addresses thermal effects but instead neglects inertial considerations. As such, the fully Dynamic and Thermo-Mechanically coupled DD model (DTM-DD) presented in this thesis fills this gap in existing DD development by simultaneously considering both inertial and thermal effects. The inertial considerations required at high strain-rate loading are incorporated through dynamic terms. Strain-rate sensitive thermal effects are captured through thermo-mechanical coupling. The competing influences of thermal, inertial, and strain-rate effects are investigated under the unifying framework of the DTM-DD. Ultimately, the DTM-DD serves as a systematic improvement to the predictive accuracy and realistic complexity in the simulation of high strain-rate plasticity.

1.1 Research Objectives

The primary research goal of this thesis is to investigate material properties and multiphysical phenomena specific to the mesoscale, particularly thermal and inertial effects and strain-rate sensitivity, at high strain-rates. A fully Dynamic coupled Thermo-Mechanical Dislocation Dynamics model (DTM-DD) is developed to simulate high strain-rate plasticity.

The primary research objectives are as follows:

1. **Formulation and development of the DTM-DD**

In order to capture inertial effects in a DD simulation, the description of the equilibrium of forces acting at a material point, which forms the basis of the computational model, must include inertia. The strong and weak forms are formulated for the initial boundary problem which describes the fully dynamic coupled thermo-mechanical system. The discrete form is derived using the eXtended Finite Element Method (XFEM) and considers a collection of edge dislocations in the continuum. The mechanical, thermal, and coupled thermo-mechanical constitutive relationships and boundary conditions are identified. The existing TM-DD framework by Skiba [6] is recast with elastodynamics to form the fully Dynamic coupled Thermo-Mechanical Dislocation Dynamics model (DTM-DD) and implemented in MATLAB$^{\text{TM}}$.

2. Formulation and development of dislocation mechanisms for the DTM-DD

Dislocation behaviour – which includes its motion, heat generation, and interactions – is explicitly simulated in the DTM-DD. A set of dislocation parameters and mechanisms is developed for the DTM-DD to characterize and regulate the behaviour of a collection of edge dislocations in a continuum. Thermal and inertial considerations are incorporated into the description of dislocation behaviour: temperature dependence is incorporated into dislocation parameters; and dynamics, into dislocation motion for a consistent dynamic perspective in the DTM-DD.

3. Utilize the DTM-DD to investigate thermal and inertial effects on high strain-rate material behaviour

The role of thermal and inertial effects on the high strain-rate plastic behaviour of metallic solids is investigated using the developed DTM-DD model. Inertial considerations are independently incorporated firstly in the description of material behaviour, and secondly in dislocation motion. The former allows externally-induced and dislocation-generated wave behaviour to be captured in simulation. As such, the resulting wave interaction and interference patterning is studied. The latter has a strong influence on dislocation behaviour; and so, the impact of dynamic dislocation motion with respect to strain-rate is investigated. The DTM-DD is then applied to the framework of extension load testing to explore the sensitivity of dislocation parameters to strain-rate and temperature dependence through parameter studies. Finally, the DTM-DD is extended to investigate loading rate effects through the simulation of the nano-indentation of a thin film specimen.

1.2 Scope of Study and Research Limitations

The scope of this research is to present a coupled thermo-mechanical Dislocation Dynamics model with inertial considerations. The developed model provides a framework to investigate material behaviour particularly under high stain-rate loading.

For simplicity, simulations are limited to the small deformation of isotropic, homogeneous materials in two-dimensions with thermo-mechanical coupling. Macroscale constitutive models for isotropic response, also with thermo-mechanical coupling, are used to describe the mesoscopic elastic response.

Plasticity is captured through the simulation of explicit dislocation mechanisms at the mesoscale using the framework of Dislocation Dynamics. A planar approach for Dislocation Dynamics imposes an additional plane strain constraint to the simulations.

Dislocation behaviour in three-dimensions is highly complex. The simplification to two-dimensions most significantly reduces the scope of applicable dislocation mechanisms and the complexity of their implementation. The focus of this thesis was not to develop an exhaustive list of subroutines to fully characterize dislocation behaviour. Rather, several key dislocations mechanisms are presented in detail, the implementation discussed, and their strain-rate and temperature sensitivity investigated in the context of high strain-rate scenarios.

Ultimately, the goal of this research is to characterize the strain-rate regimes where inertial and temperature effects, in particular strain-rate and temperature dependency, become crucial for greater accuracy in the depiction of material behaviour at high strain-rates.

Chapter 2

Background and Research Context

The plastic deformation of crystalline solids is attributed to the mechanisms of crystallographic defects – known as dislocations – at the atomic level [16]. The manifestation of plastic flow is the direct consequence of the generation and collective motion of individual dislocations within an elastic continuum [15]. The creation, behaviour, and interaction of dislocations at this scale is characterized by the so-called *Theory of Dislocations* [5].

A variety of computational models have been developed to simulate plasticity across a spectrum of characteristic spatial and temporal scales, from the behaviour of single dislocations to continuum-level crystal plasticity. The method of Dislocation Dynamics (DD) at the mesoscale provides a bridge between atomic and continuum plasticity models [17]. This family of models is characterized by the explicit simulation of a collective of discrete dislocations. The term "dynamics" in DD referring to the time-dependent evolution of dislocation structures [10].

In this chapter, first, the *Theory of Dislocations* is presented. Dislocations are introduced to provide context for a subsequent discussion of their simulation in the DD framework. The numerical implementation of the dislocation features discussed in this chapter are provided in Ch. 4. Next, an overview is provided of established DD techniques and computational models implemented in both two- and three-dimensions. Particular attention is paid to models based on the eXtended Finite Element Method (XFEM) as it forms the basis of the research presented in this thesis. Finally, the discussion is directed to the effect of strain-rate on material behaviour, with a focus on high strain-rates, within the context of DD simulations.

2.1 Dislocation Theory

The structure of crystalline solids (crystals) is defined by the ordered, symmetric, and periodic nature of its constituents, ex. atoms and molecules [18]. The lattice structure of an ideal crystal is described by the repetitive translation of a unit cell, the smallest group of constituents that contains the repeating pattern.

In 1907, Volterra introduced continuum theory describing the elastic fields generated by crystallographic defects in an otherwise perfectly ordered crystal lattice [19]. Subsequently, Taylor [20], Orowan [21–23], and Polanyi [24] independently postulated in 1934 that the movement of these defects at low stress levels allows for permanent deformation without fundamentally altering the crystalline nature of the lattice. The term "dislocation" was coined by Taylor to refer to these defects at the atomic scale [20]. The study of dislocations and their behaviour have since become central in understanding the strength and plasticity of crystalline materials.

Hirth & Lothe [5] present a mesoscale theory describing dislocation interaction mechanisms, termed *Theory of Dislocations*. Plasticity in crystalline materials is attributed to the generation, movement, and interactions of dislocations which occur on specifically oriented slip planes based on the packing arrangement of the crystal structure [25]. The yield point of a material is the threshold where its behavior under loading transitions from elastic to plastic, i.e. from recoverable to permanent deformation. In the *Theory of Dislocations*, this transition corresponds to a stress of state where dislocations and their interactions activate [5]. As a material is loaded past its yield point, the density of dislocations increases and the motion of dislocations becomes hindered by inter-dislocation interactions. In this way, the impedance of plastic deformation at the microscale is reflected in the relative hardening of the material at the macroscale.

The topics of crystal structure, dislocations, and their properties are extensively and comprehensively covered in a variety of foundational texts, for example, [5, 25, 26]. Here, for context, an overview of the main features of dislocations is provided: dislocations, their types, and the Burgers vector is introduced; and dislocation mobility is presented.

2.1.1 Types of Dislocations and the Burgers Vector

Dislocations are classified into two main types: edge and screw. In reality, dislocations are typically "mixed" in three-dimensions, having characteristics of both edge and screw; or decomposed into "partial" dislocations to facilitate movement through the crystal structure [5].

An edge dislocation is where an additional half plane of atoms is introduced into (or removed from) the crystal lattice, schematically shown in Fig. 2.1a. The dislocation line runs along the bottom of the inserted plane. The dislocation "core" refers to where the distortion to the crystal structure is greatest which, for an edge dislocation, is at the dislocation line. The character of the atomic planes is preserved but the neighbouring crystal structure is distorted. In contrast, a screw dislocation is a line discontinuity in the crystal structure, schematically shown in Fig. 2.1b. The atom planes perpendicular to the dislocation line are turned into a spiral ramp [16].

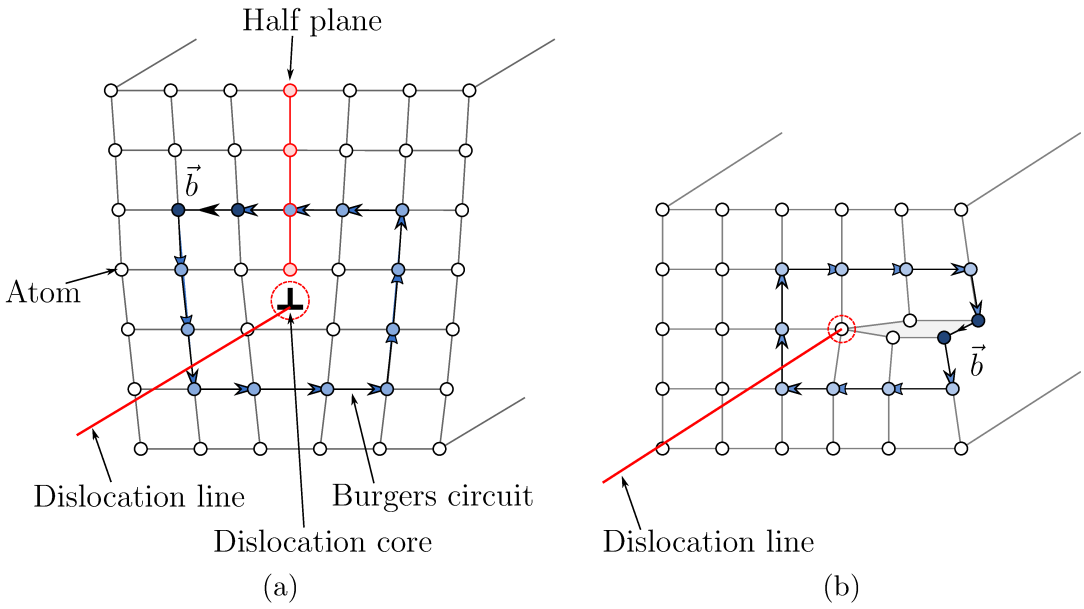

Figure 2.1: Schematic of dislocation of the (a) Edge type, with the half plane and core shown; and (b) Screw type. The dislocation line for each dislocation type is indicated in red.

The Burgers vector of a dislocation describes the magnitude and direction of the dislocation's distortion to the crystal lattice. In Fig. 2.2, a circuit is drawn around an edge dislocation core, and below it, another around perfect crystal. If the same atom-to-atom sequence is followed for the circuit enclosing the core as for the one not, i.e. the same number of jumps in each direction, it is apparent that the start and end atoms are not the same for the two loops. The loop is called the Burgers circuit, and the Burgers vector is defined as the closure failure [16]. For an edge dislocation, the Burgers vector is perpendicular to the dislocation line (Fig. 2.1a); and for a screw dislocation, it is parallel (Fig. 2.1b).

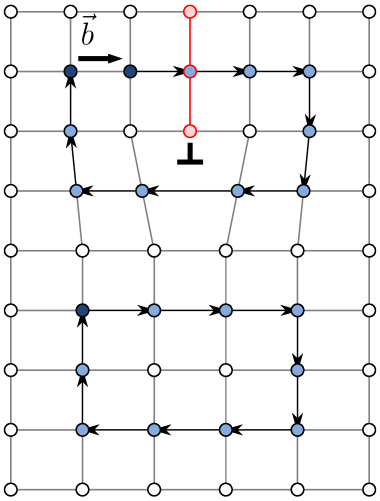

Figure 2.2: Definition of the Burgers vector via the closure failure of the Burgers circuit for an edge dislocation. Adapted from [16].

2.1.2 Modeling of Dislocations

The three-dimensional physical problem is simplified into a two-dimensional one through the assumption of plane strain conditions following the method proposed by Van der Giessen & Needleman [27]. The planar method is discussed in detail in Sec. 2.2.1. The treatment of dislocations in the planar method is adopted in the DTM-DD model. Presently, it is important to note the implications of this method on the scope of simulatable dislocations and dislocation mechanisms. Most importantly, the planar simplification reduces the scope of the simulated dislocations to infinite, straight edge dislocations. In this way, screw dislocations are implicitly assumed to not govern dislocation effects. We then focus on the theory and implementation of mechanisms pertinent to edge dislocations only for the purpose of discussion in this chapter.

2.1.3 Mobility of Dislocations

The movement of dislocations is directly manifested in plastic deformation of crystalline solids. The characterization of dislocation mobility is then critical in defining the character of dislocation motion in DD. Contributions to the elastic fields in a system are from (1) long-range stress fields originating from boundary conditions or other external stimuli, and (2) short-range fields from the lattice distortion generated by the presence of dislocations. The

minimization of the elastic energy in the system is the driving mechanism for dislocation movement. Thus, dislocation motion is a dissipative process, which occurs in such a way to minimize the energy within the system [5].

Dislocation motion is classified primarily into glide or climb motion which is defined with respect to the direction of motion and the crystal structure. The collective movement of dislocations generates "slip" which is manifested in the plasticity of a crystalline solid. The deformation of crystals by slip tends to occur on atomic planes with the greatest planar packing density (close-packed planes); and also in the directions with the highest linear packing density (close-packed directions) [5]. Dislocation glide is motion on-, and climb is motion perpendicular to such a crystallographic plane. Climb is a diffusion-assisted process which, particularly under high strain-rate loading, is too slow to be significant [10]. In this way, dislocation climb is neglected in this work and only glide motion is simulated.

A glide plane is described as a line of motion in a slip direction on a slip plane. A dislocation moves in the direction perpendicular to its dislocation line, and individual atoms slip in the direction parallel to the Burgers vector. In the case of an edge dislocation, the dislocation moves in the same direction as its Burgers vector (Fig. 2.3a). The sense of the Burgers vector is governed by the slip direction. A slip system is the set of all parallel glide planes on a particular slip plane. This motion causes one half of the crystal to be displaced relative to other, or a shear displacement which gives rise to shear strains.

The set of slip systems are unique to each type of crystal structure. For example, the preferred slip planes of face-centered cubic (fcc) crytals are along the "face diagonals". Planes $\{111\}$ are the most densely packed, and the $\{111\} < 110 >$ directions in particular have been identified as the primary slip system in fcc crystals (Fig. 2.4) [5]. Four slip planes with three slip directions on each plane results in twelve possible slip systems for fcc crystals.

In the planar DTM-DD model, slip systems are defined as straight lines within the domain of study, oriented to resemble the crystallography of the material. Sources and obstacles are represented as points on these slip plane lines. Edge dislocations are similarly modeled as points with its additional half-plane of atoms extending out-of-plane.

Schmid [29] postulated that the dislocation slip which drives plastic deformation occurs when the applied shear stress, resolved along the slip direction on the slip plane, reaches a critical value τ_{crit}; and also that material yield will occur on the slip system first to reach τ_{crit} [29]. The critical resolved shear stress of single crystals under applied tensile stress has been determined experimentally through the measurement of yield stress as a function of crystal orientation. The resolved shear stress on a slip plane parallel to the slip direction

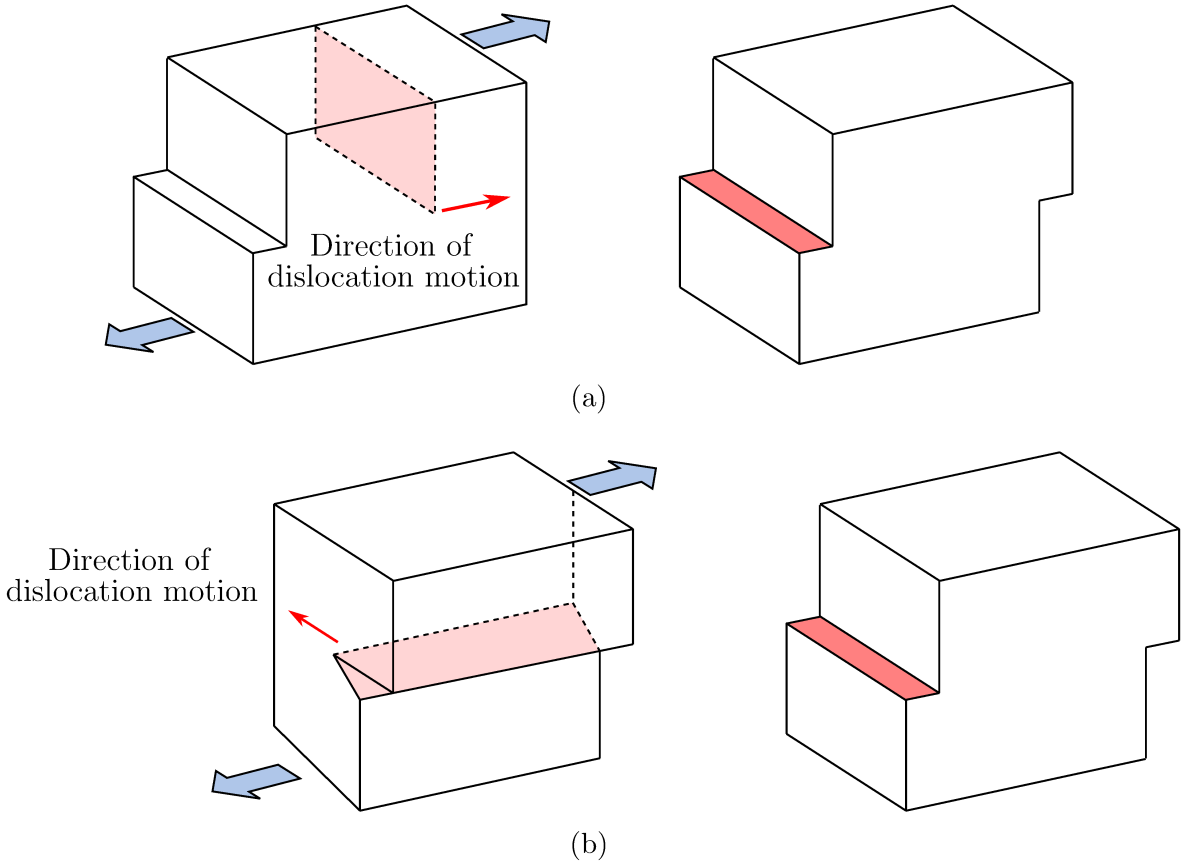

Figure 2.3: Glide motion of a dislocation of (a) Edge type, and (b) Screw type. The direction of motion of the dislocation line is indicated in red. The net plastic deformation of the two dislocation types is equivalent. Adapted from [28].

is determined by Schmid's Law (Fig. 2.5):

$$\tau = \sigma cos\phi cos\lambda = m\sigma \tag{2.1}$$

where $\sigma = F/A$ is the applied tensile stress, where F is the applied force, and A is the cross-sectional area; ϕ is the angle between the applied stress and the normal to the slip plane; λ is the angle between the applied stress and the slip direction; and m is known as the *Schmid factor*. The resolved shear stress serves as an activation criteria for dislocation nucleation.

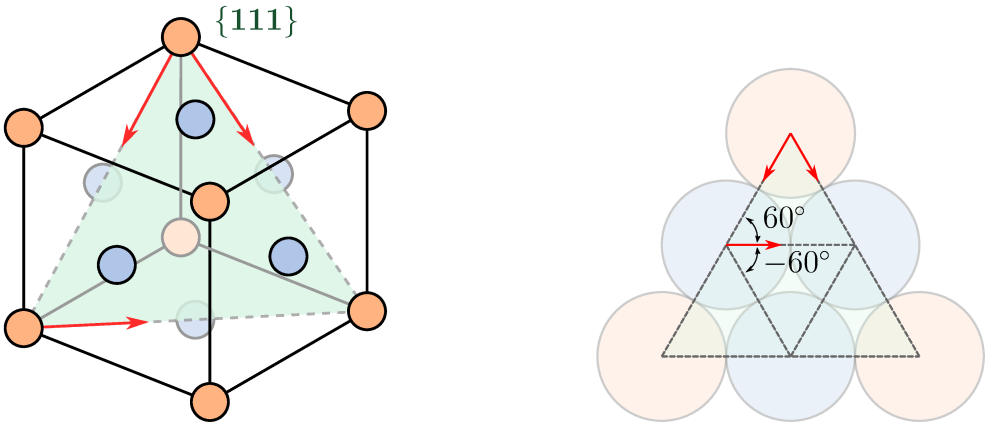

(a) (b)

Figure 2.4: (a) Reference cube of face-centered cubic crystal with slip plane {111}. (b) Assumed glide plane orientation on slip plane {111}.

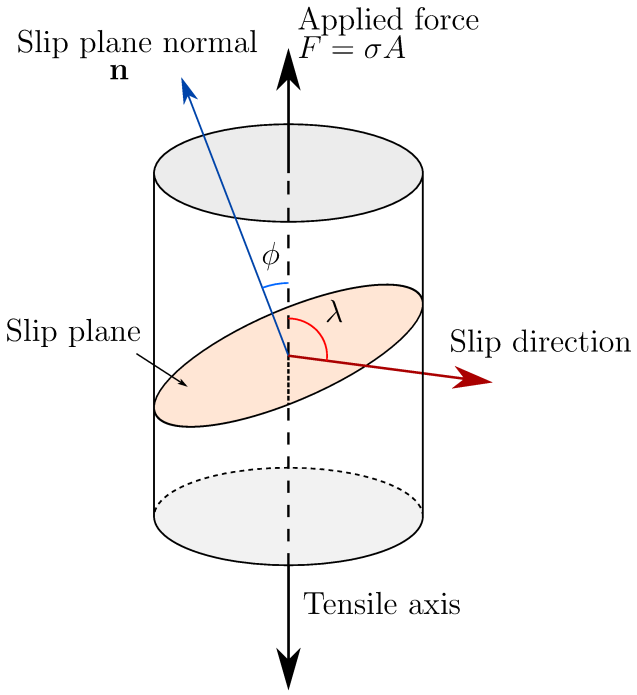

Figure 2.5: The resolved shear stress acts on the slip plane parallel to the slip direction as determined by Schmid's Law.

2.1.4 Dislocation Sources

Dislocation multiplication occurs through several mechanisms, for example, from Frank-Read sources and Bardeen-Herring climb sources; or via cross-slip mechanisms, among others [5]. The current work is based on the planar DD assumption that cross-slip mechanisms are not dominant. As well, diffusive dislocation climb motion was assumed to be too slow to be significant in a high strain-rate setting. As such, we focus on the Frank-Read source as the mechanism for dislocation nucleation following [27]. The Frank-Read process is described in detail by [5].

The Frank-Read source is a dislocation segment pinned at its ends. Under applied stress, the segment bows out on its glide plane. For a shear stress state under a critical value, the segment maintains a metastable equilibrium due to the balancing force of the line tension in the segment. Conversely, when the resolved stress state acting on the segment exceeds the critical activation stress τ_{nuc}^{FR}, i.e. $|\tau| \geq \tau_{nuc}^{FR}$, no stable equilibrium state exists and the segment continues to bow out into a loop. Finally, a critical configuration is reached when a portion of the resulting loop is annihilated, creating a stable closed loop and restoring the original configuration of the pinned segment. The Frank-Read process occurs over a time period of t_{nuc} and the dislocation dipole is generated at a mutual distance of L_{nuc}^{FR} in the configuration shown in Fig. 2.6.

2.2 Techniques of Dislocation Dynamics

Dislocations are crystallographic defects which distort an otherwise perfectly ordered crystal lattice. Each dislocation can be comprehensively described by the position and orientation of its core (the centre of the dislocation line where the distortion effect is the greatest) and the direction of its motion. In DD, the dislocations are treated as singularities within an elastic continuum representing the crystal. Long-range interactions between dislocations are governed by overlapping self-induced elastic fields, as well as fields due to external tractions. Short-range interactions are regulated by dislocations mechanisms (e.g. pinning, annihilation) between proximate dislocations [5].

Short-range interactions are governed by constitutive rules: typically activation or occurrence criteria are specified, for example, in the form of a critical separation distance or limiting stress state. In a similar fashion, the motion of dislocations as induced by external loads is governed by mobility laws. As well, the generation of dislocations is subject to a set of nucleation rules which define the conditions which activate the generation mechanism, the process by which it happens, and the state of new dislocations. These constitutive rules

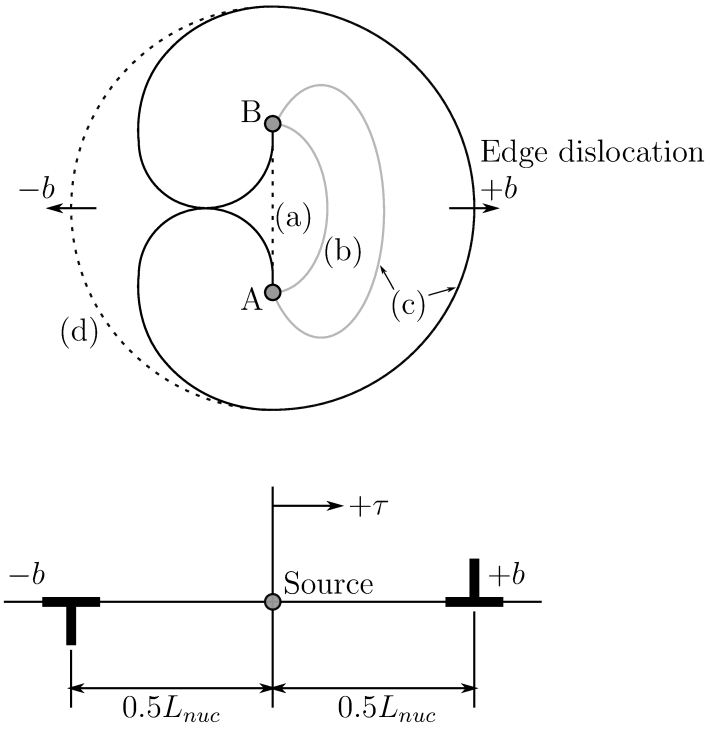

Figure 2.6: The pinned dislocation segment of a Frank-Read source in two-dimensions (a) is pinned at ends A and B; (b) bowed out in a metastable equilibrium; and (c) and (d) reaching the critical configuration of the Frank-Read mechanism. The dislocation dipole is generated at a mutual distance of L_{nuc}^{FR} for a resolved shear stress $\tau > 0$ in the convention shown. For $\tau < 0$, the signs of the Burgers vector b is reversed. Adapted from [5, 27].

regulate the evolution of the dislocation microstructure and are specific to each particular implementation of the DD method.

A large variety of DD models have been developed to date. Three-dimensional models (ex. [17, 30–33]) are fairly robust due to their ability to accommodate many degrees of freedom and types of dislocation interactions, and to provide realistic results. However, their accuracy is associated with a large computational expense, and hence trade-offs in model size and complexity, as well as simulation runtime [10, 34]. For this reason, two-dimensional models (ex. [35–38]) are an attractive alternative. The motion of dislocation lines in three-dimensional space is reduced to the planar motion of points. However, realistic dislocation motion is appreciably impacted by line tension and interaction mechanisms

which can only be captured in three-dimensions. In this way, two-dimensional models have a limited capacity to fully capture the physics of crystal plasticity in a truly accurate and quantitative manner. Instead, since two-dimensional models are relatively simple and not constrained in the same manner as three-dimensional models with respect to computational expense, they are an excellent tool to study plasticity trends qualitatively. As such, two-dimensional models have been extensively used to investigate a variety of dislocation-dependent features, for example, size and geometric effects, fracture mechanics and crack propagation, fatigue, and creep [10].

The majority of DD models may be grouped under two main techniques of implementation: (1) models based on the principle of superposition; and (2) models based on the eXtended Finite Element Method (XFEM). As the current work falls under the XFEM family, greater emphasis is placed on the discussion of XFEM and XFEM models.

2.2.1 Models of Superposition

In DD models based on the principle of superposition, dislocation slip is modeled as strong discontinuities in a continuum displacement field of a finite domain [39]. The resulting elastic problem is difficult to treat both analytically and numerically. Analytical solutions are known to introduce $20-30\%$ error for crystal lattices, as in the two-dimensional isotropic models by Schwarz [5,32]. For three-dimensional models, ex. by Kubin et al. [40], analytical solutions take the form of Green's functions which were historically not readily available for complex boundaries, material interfaces, or anisotropic mediums [41]. Additionally, the solution of infinite domain integrals for anisotropic materials is very computationally demanding even in single material systems [42]. In this way, earlier superposition models were highly restricted in their flexibility and capability. However, recent superposition models utilize current developments of Green's functions and significantly improve on their predecessors. For example, recent models have been presented that incorporate anisotropic elasticity [43–46]. Superposition models remain widely used primarily due to the relative ease of use.

The image field model – or the so-called Planar DD method (DDP) – introduced by Van der Giessen & Needleman [27] simplifies the system into two-dimensions using an assumption of plane strain. The planar approximation restricts the DDP to the simulation of infinite straight edge dislocations and implicitly assumes that cross-slip does not govern dislocation mechanisms [27]. In the conventional formulation, plasticity is described through the collective quasi-static motion of dislocations explicitly represented as line singularities within a linear-elastic solid [15]. Thus, slip systems are defined as straight lines within the

domain of study, oriented to resemble the crystallography of the material. Sources and obstacles are represented as points on these slip plane lines; and edge dislocations, also as points with its additional half-plane of atoms extending out-of-plane [15]. The primary components in the evolution of the dislocation system are: (1) dislocation motion i.e. the translation of dislocations along their slip plane via glide; (2) nucleation of dislocation pairs from discrete sources; and (3) dislocation interaction which includes the pinning of dislocations at obstacles and the annihilation of opposing dislocations [27].

The complex elastic problem is decomposed using the principle of linear superposition (Fig. 2.7). First, the analytical infinite domain solution of each individual dislocation is considered. The analytical solutions are known, and the result of the interaction between dislocation fields is easily determined [10]. Second, an "image" stress field is numerically determined using standard finite elements. It is imposed to correct the collective infinite domain solutions for the true boundary conditions of the finite domain [47]. Although the DDP introduces restrictions to the setup of the model as well as the types of dislocations and dislocation mechanisms that can be simulated, it is relatively simple and robust in its implementation, and flexible enough to accommodate arbitrary boundary conditions [10].

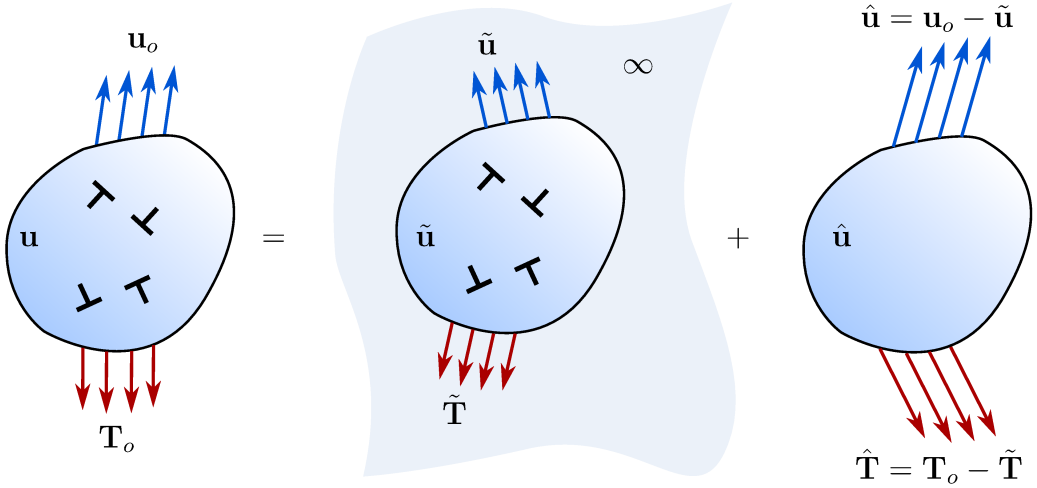

Figure 2.7: Principle of superposition: the solution of the domain with dislocations is decomposed into analytical infinite domain solution fields for the dislocations ($\tilde{\bullet}$) and the "image field" ($\hat{\bullet}$). Adapted from [27].

In spite of its advantages, computational expense is an inherent weakness of superposition models due to the use of superposition. The driving force of each of the n_d dislocations in a domain requires the superposition of n_d infinite domain solutions. This results in an n_d^2 dependence in computational costs [42]. Due to the use of standard finite elements,

it is also computationally expensive to (1) determine the "image" stress field; and (2) capture the slip across a glide plane, i.e. the displacement discontinuity within a single element caused by a dislocation, even only in an average sense [42]. When dislocation cores approach a boundary, the computational cost is further compounded by the large amount of quadrature points required for the accurate numerical integration of tractions at the boundary [42].

2.2.2 eXtended Finite Element Method Models

The application of the eXtended Finite Element Method (XFEM) to DD is a relatively recent development. This family of models can model material anisotropy, arbitrary interfaces, and grain boundaries with relative ease without the use of analytical solutions or superposition principles [42]. XFEM was first applied to two-dimensional crack propagation problems in elastic domains to avoid remeshing of the domain [48,49], and subsequently extended to three-dimensional crack modelling [50], nonlinear fracture mechanics [51], shear band growth [52], among other applications.

The classical finite element (FE) mesh requires that element edges coincide with domain boundaries and discontinuities [42]. This requirement is particularly troublesome for problems based on evolving discontinuities. The domain must be constantly remeshed to conform to the changing geometry of a discontinuity network which is computationally expensive [53]. Thus, the principle advantage of the XFEM is the ability to model arbitrary discontinuities in a finite element mesh without remeshing.

Interpolation in the classical FE method uses standard shape functions based on polynomials through the Partition of Unity Method (PUM) by Babuska & Melenk [54]. The functions $\check{N}_j(\mathbf{x})$ form a partition of unity in a n-dimensional domain Ω through the relationship

$$\sum_{j \in \check{\mathcal{S}}} \check{N}_j(\mathbf{x}) = 1 \tag{2.2}$$

where $\check{\mathcal{S}}$ is a set of mesh nodes.

Based on the PUM, enrichments can be locally introduced to improve the discrete approximation based on the physics of the problem, for example, to reflect singularities or jumps [53]. In planar XFEM models, dislocations are represented as points of singularity within an elastic continuum following the Volterra description of the dislocation [19,55,56]. In the Volterra model, an elastic solid is cut and the two surfaces of the cut are displaced and reattached generating an elastic field (Fig. 2.8). The cut corresponds to the dislocation

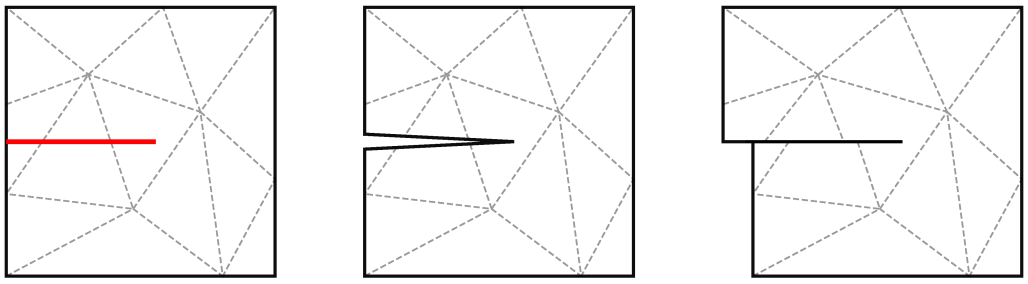

Figure 2.8: Volterra description of the dislocation. The magnitude of the lattice distortion is represented by the relative displacement of the two sides of the reattached cut. Adapted from [42]

plane of motion, and the relative displacement between the cut surfaces is a measure of dislocation strength. The distortion in the crystal structure generated by the presence of a dislocation is represented by its Burgers vector, $\mathbf{b}$ [42].

Ventura et al. [56] apply the PUM to correct a standard displacement approximation from classical FE by incorporating the discontinuous displacement fields in the Volterra model using enrichments. The enriched displacement approximation in XFEM takes the standard form of

$$\mathbf{u}^h(\mathbf{x}) = \underbrace{\sum_{i\in\mathcal{S}} N_i(\mathbf{x})\mathbf{u}_i}_{\text{FEM}} + \underbrace{\sum_{j\in\check{\mathcal{S}}} \check{N}_j(\mathbf{x})\psi(\mathbf{x})\mathbf{a}_j}_{\text{XFEM enrichment}}, \qquad \mathbf{x}\in\Omega \tag{2.3}$$

where $\psi(\mathbf{x})$ is the enrichment function; N_i and $\mathbf{u}_i$, and $\check{N}_j(\mathbf{x})$ and $\mathbf{a}_j$, are the shape functions and degrees of freedom corresponding to the standard and enriched nodes i and j in sets $\mathcal{S}$ and $\check{\mathcal{S}}$, respectively. The first term on the right-hand-side corresponds to the classical FE approximation and the second term is the enrichment. In order to maintain the correct displacement approximation at element edges, the enrichment field is shifted such that the enrichments disappear at element edges:

$$\mathbf{u}^h(\mathbf{x}) = \sum_{i\in\mathcal{S}} N_i(\mathbf{x})\mathbf{u}_i + \sum_{j\in\check{\mathcal{S}}} \check{N}_j(\mathbf{x})[\psi(\mathbf{x}) - \psi(\mathbf{x}_i)]\mathbf{a}_j, \qquad \mathbf{x}\in\Omega \tag{2.4}$$

The terms in the resulting discrete form are expressed as integrals. Depending on the choice of enrichment function, the smoothness of the integrals may be affected and it becomes difficult to evaluate them numerically using standard Gauss quadrature [6]. Gracie et

al. [42] proposed the use of tangential enrichments to explicitly model edge dislocations as interior discontinuities. Subsequently, Gracie et al. [57] and Ventura et al. [58] investigated core enrichments and suggested alternatives for enrichment schemes. A Heaviside step function enrichment is used in Belytschko et al. [59] to describe the jump in displacement across a crack line which is highly analogous to the strong displacement discontinuity of the Volterra dislocation model. Weak form integrals simplify to polynomials using a step enrichment function and can be easily evaluated using standard Gauss quadrature [6].

The XFEM treatment of Gracie et al. [42] and Belytschko et al. [59] is blended in the work by Skiba through the use of tangential Heaviside enrichment functions to explicitly model edge dislocations as interior discontinuities [6]. Skiba presents a novel thermo-mechanical coupling in an XFEM DD model (the TM-DD) which captures heat generation by dislocation motion as well as includes the effect of heat conduction [6]. Deformation of crystalline solids was investigated at rates between $10^3\ s^{-1}$ and $10^4\ s^{-1}$. The increasing importance of thermal effects corresponding to increasing strain-rates was observed. Thermocoupling is necessary for increased accuracy of DD models, particularly for high rate simulations [6,60]. The work presented in this thesis follows the method behind the TM-DD.

2.3 Effect of Strain-Rate

The division of material behaviour into two distinct strain-rate regimes is readily apparent in the relationship between yield point and strain rate in Fig. 2.10. Yield point behaviour is logarithmically-linear to strain-rate at low strain rates under $10^3\ s^{-1}$ (Fig. 2.9) [11]. Experimental trails and mesoscale plasticity studies are largely performed at these lower rates [10]. A small amount of hardening is apparent at low rates but experimental results indicate that the system generally hardens with increasing strain-rates [61].

At low strain-rates, a system is perturbed slowly enough such that the timescale of load application is significantly greater than that of the signal transmission through the domain. Although there is in fact a finite time required for elastic signals to travel, it reasonable to assume that the elastic fields of both the external tractions and of the moving dislocations are propagated instantaneously throughout the entire medium [15]. In the same manner, dislocations may be assumed to instantaneously reach terminal glide velocity [15]. As such, the system effectively evolves from one state of mechanical equilibrium to another. Consequently, a *quasi-static* assumption is well-justified for simulations at low strain-rates.

Comparatively the timescale of the application is instead less than the that of the signal transmission through the domain under high strain-rate loading. Elastic fields cannot be

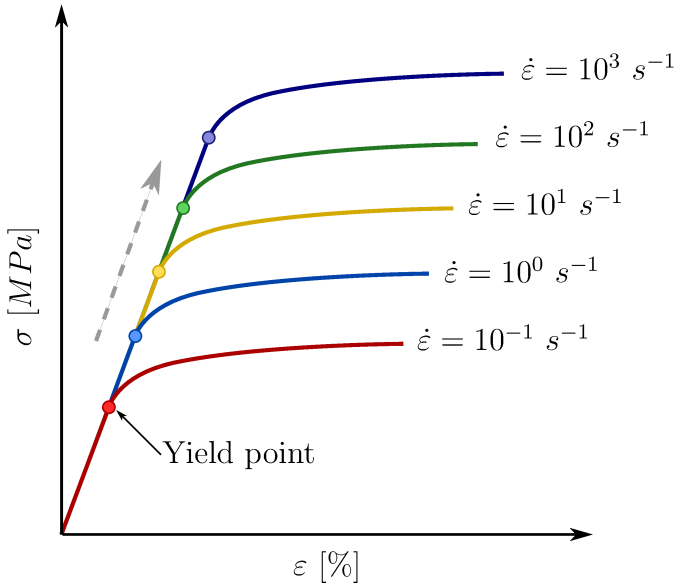

Figure 2.9: Schematic of stress-strain curves at low strain-rates $\dot{\varepsilon} \leq 10^3\ s^{-1}$. Yield point is logarithmically-linear to strain-rate in this regime. Adapted from [10].

assumed to be transmitted instantaneously throughout the domain. Instead, the system evolves through the propagation and interaction of elastic waves, as opposed to between states of mechanical equilibrium. Thus, systems under high strain-rate loading are fully *dynamic*. The inclusion of inertial terms which capture the finite traveling time of elastic signals is necessary to fully describe wave propagation behaviour through the medium.

A transition region between strain-rates of $10^4\ s^{-1}$ and $10^6\ s^{-1}$ occurs where the yield-point-strain-rate behaviour suddenly upturns and material behaviour becomes highly strain-rate dependent (Fig. 2.10). This implies that the fundamental mechanism of plastic flow is different between the two strain-rate regimes [10]. Several theories attempt to explain the shift in mechanism, for example by [63, 64]. Follansbee et al. [11] and Reggazoni et al. [12] propose a particularly well-received theory: this change in mechanism is due to a corresponding change in the regime of dislocation motion, from thermally activated to drag-controlled. Multiphysical phenomena that are not apparent at lower rates emerge during this transition and increase the complexity of material behaviour [6]. For example, significant localized heating and overall thermal softening in material behaviour has been observed with the formation of localized shear bands at high rates [65–67].

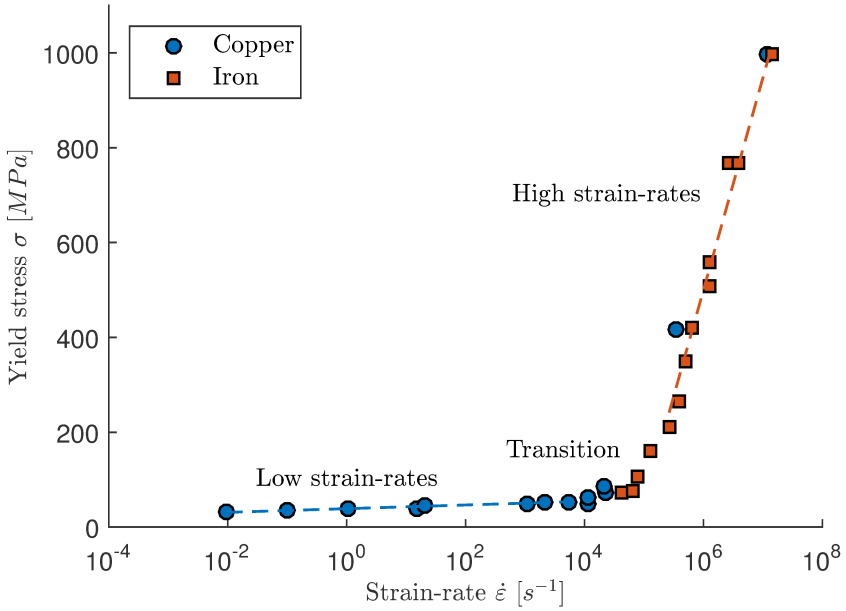

Figure 2.10: Experimentally determined yield point behaviour for copper and iron with respect to strain-rate. A sudden upturn in the yield stress occurs in region of $\dot{\varepsilon} = 10^4\ s^{-1}$. Adapted from [10, 62].

2.4 High Strain-Rate Dislocation Dynamics Models

Conventional DD models (including DDP) are (1) based on a quasi-static formulation, neglecting inertial terms; and (2) purely mechanical, neglecting or underestimating the significance of thermal softening.

Recognizing that a quasi-static formulation is not necessarily justified at high strain-rates, some attempts have been made to address the dynamics of a high rate problem. Implicitly so, Roos et al. [13] modified the elastic dislocation solutions to reflect the higher dislocation velocities associated with high strain-rate loading. Shehadeh et al. [14] employed a hybrid quasi-static dynamic implementation of the superposition method for single crystal copper simulations shocked at strain-rates greater than $10^6\ s^{-1}$. The elastic fields of the medium were adjusted for dynamics, i.e. an elastodynamic solution, but a quasi-static description of dislocation fields was retained [10].

The Dynamic Discrete Dislocation Plasticity (D3P) model by Gurrutxaga-Lerma et al. [15] was first to treat elastic dislocation fields as fully time-dependent within an elastodynamic continuum. The D3P is a purely mechanical model based on the superposition method

and was applied to shock loading scenarios with strain-rates in the excess of $10^6\ s^{-1}$. A comparative study between quasi-static and dynamic formulations utilizing D3P concluded that non-physical phenomena arise as an artefact of the quasi-static approximation [15]. Most notably, it was observed that sources were activated by dislocation fields transmitted ahead of the plastic front. They conclude that this artefact can be avoided by simply solving the elastodynamic equations in lieu of the elastostatic ones used in the conventional DD formulation. Thus, the quasi-static assumption is not a justifiable one for high strain-rate simulations and it is then necessary to capture dynamic effects in corresponding DD models.

This presents a clear direction for the systematic improvement of existing DD models, for example, the TM-DD as proposed by Skiba [6]. In the context of high strain-rate plasticity, the inclusion of thermal effects through thermo-mechanical coupling was identified as crucial for simulation accuracy. However, for simplicity as a novel method, the TM-DD was formulated based on the conventional quasi-static assumption which is not justified given the simulation context. As such, the research presented in this thesis aims to address this discrepancy: the existing TM-DD is augmented with inertial terms such that the full dynamics required for the investigation of high strain-rate plasticity is captured while thermal influences are preserved.

Chapter 3

Formulation and Numerical Implementation

In this section, the strong, weak, and discrete forms are developed for the initial boundary value problem of the fully dynamic thermo-mechanically coupled system in the presence of dislocations using the eXtended Finite Element Method (XFEM).

3.1 Strong Form

Consider a domain Ω which contains n_d dislocations and is bounded by Γ (Fig. 3.1). The boundary Γ is decomposed into the sets Γ_T, Γ_h, Γ_u, and Γ_t, such that

$$\begin{aligned} \Gamma_T \cap \Gamma_h = \emptyset \quad \text{and} \quad \Gamma_T \cup \Gamma_h = \Gamma \\ \Gamma_u \cap \Gamma_t = \emptyset \quad \text{and} \quad \Gamma_u \cup \Gamma_t = \Gamma \end{aligned} \tag{3.1}$$

where the subscripts T, h, u, and t correspond to the part of the boundary of the domain with temperature, flux, displacement, and surface traction conditions, respectively. For dislocation α, let the active part of the glide plane (i.e., where slip has occurred) and its core location be denoted as Γ_d^α and Ω_d^α, respectively. Following this, we denote $\Gamma_d = \cup_\alpha \Gamma_d^\alpha$ and $\Omega_d = \cup_\alpha \Omega_d^\alpha$ for $\alpha \in [1, n_d]$. The strain energy is unbounded in the core region and bounded elsewhere (Ω_d/Ω) [42].

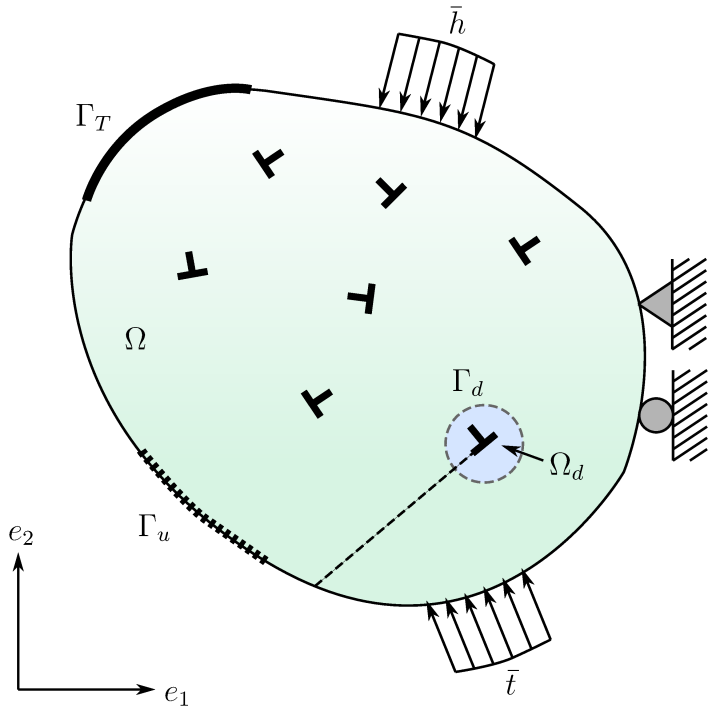

Figure 3.1: Definition of system boundary and domain. Adapted from [6, 53]

The differential equations that govern the coupled model are the heat equation and the equation of motion:

$$C_p \rho \dot{\boldsymbol{\Theta}}(\mathbf{x}, t) + \nabla \cdot \mathbf{q} = S(\mathbf{x}, t) \tag{3.2}$$

$$\nabla \cdot \boldsymbol{\sigma} + \mathbf{g} = \rho \ddot{\mathbf{u}} \tag{3.3}$$

where $\boldsymbol{\Theta}$ is the absolute temperature change from a stress-free reference temperature Θ_0 at the point $x \in \Omega$ at time t, $\mathbf{q}$ is the heat flux density, S is the body heat source which varies with position and time, the superimposed dot represents the material time derivative, $\boldsymbol{\sigma}$ is the Cauchy stress tensor, $\mathbf{g}$ is the body force, and $\ddot{\mathbf{u}}$ is the acceleration. Material properties of the body including mass density, specific heat capacity, and coefficient of thermal conductivity are denoted as ρ, C_p, and k, respectively.

The differential equations are constrained by their respective boundary conditions. The Dirichlet and initial boundary conditions are:

$$\Theta(\mathbf{x}, t) = \bar{\mathbf{T}} \quad \text{on} \quad \Gamma_T \tag{3.4}$$

$$\Theta(\mathbf{x}, t_0) = \mathbf{T}_0 \quad \text{on} \quad \Omega \tag{3.5}$$

$$\mathbf{u}(\mathbf{x}, t) = \bar{\mathbf{d}} \quad \text{on} \quad \Gamma_u \tag{3.6}$$

$$\mathbf{u}(\mathbf{x}, t_0) = \mathbf{d}_0 \quad \text{on} \quad \Omega \tag{3.7}$$

Similarly, the Neumann conditions are:

$$\mathbf{q} \cdot n = \bar{\mathbf{h}} \quad \text{on} \quad \Gamma_h \tag{3.8}$$

$$\boldsymbol{\sigma} \cdot n = \bar{\mathbf{t}} \quad \text{on} \quad \Gamma_t \tag{3.9}$$

where the heat flux h and surface traction $\bar{\mathbf{t}}$ are imposed quantities on the applicable boundaries.

The modeling of edge dislocations is based on the dislocation models of Volterra [19] and Eshelby [55]. An elastic solid is cut and reattached such that the two surfaces of the cut are displaced relative to one another (Fig. 2.8). The internal discontinuity in the displacement field represents a measure of the magnitude of the lattice distortion as described by the Burgers vector of the dislocation. For an edge dislocation, the Burgers vector – and so also *slip* – is along its glide plane. As such, the system is additionally subjected to an internal boundary condition

$$[|\mathbf{u}|] = b^\alpha \bar{\mathbf{e}}_t \equiv \mathbf{b}^\alpha \quad \text{on} \quad \Gamma_d^\alpha \tag{3.10}$$

where $[|\mathbf{u}|]$ is the jump in displacement across Γ_d^α, $\bar{\mathbf{e}}_t$ is the unit vector tangent to the glide plane, and $\mathbf{b}^\alpha$ is the Burgers vector of dislocation α. The strong of the coupled thermomechanical problem is presented in (3.2) to (3.10).

The constitutive relation of heat flux $\mathbf{q}$ and stress $\boldsymbol{\sigma}$ are defined by Fourier's Law and Hooke's Law in (3.11) and (3.12), respectively.

$$\mathbf{q} = -k \nabla \Theta(\mathbf{x}, t) \tag{3.11}$$

$$\boldsymbol{\sigma} = \mathbf{C} : \boldsymbol{\varepsilon} - \boldsymbol{\lambda} \boldsymbol{\Theta} \tag{3.12}$$

where k is the thermal conductivity; $\nabla\Theta$ is the temperature gradient; $\boldsymbol{\lambda} = \mathbf{C} : \boldsymbol{\gamma}$; and $\mathbf{C}$ and $\boldsymbol{\gamma}$ is the tensor of elastic moduli and coefficients of linear thermal expansion, respectively.

A small strain, linear elastic formulation was adopted from [42] such that strain is expressed using the symmetric displacement gradient

$$\boldsymbol{\varepsilon} = \frac{1}{2} \left(\nabla^\top \mathbf{u} + \nabla \mathbf{u} \right) \tag{3.13}$$

Finally, the body heat source S in (3.2) is defined over domain and time. First introduced by Skiba [6], the heat generation within the domain is characterized by the motion of

individual dislocations The total heat generated is expressed as a linear combination of dirac-delta functions:

$$S(\mathbf{x},t) = \sum_{\alpha=1}^{n_d} s_\alpha(t)\delta(\mathbf{x}-\mathbf{x}_\alpha) \tag{3.14}$$

where $s_\alpha(t)$ and $\mathbf{x}_\alpha$ is the heat generated and the position of dislocation α at time t, respectively.

3.2 Weak Form

The weak form is to find $\Theta(\mathbf{x},t)$ and $\mathbf{u}(\mathbf{x},t)$ that the initial conditions in (3.5) and (3.7) are satisfied and

$$\int_\Omega \omega C_p \rho \dot{\Theta} d\Omega + \int_\Omega \nabla\omega(k\nabla\Theta)d\Omega = \int_\Omega \omega S(\mathbf{x},t)d\Omega - \int_{\Gamma_h} \omega \bar{\mathbf{h}} d\Gamma, \quad \forall\omega \in \mathcal{W} \tag{3.15}$$

$$\begin{aligned} \int_\Omega \nabla\boldsymbol{\varsigma}^T \cdot \mathbf{C} : (\nabla_s \mathbf{u})d\Omega - \int_\Omega \nabla\boldsymbol{\varsigma}^T \cdot \boldsymbol{\lambda}\Theta d\Omega + \int_\Omega \boldsymbol{\varsigma}^T \cdot \rho\ddot{\mathbf{u}} d\Omega \\ = \int_{\Gamma_t} \boldsymbol{\varsigma}^T \cdot \bar{\mathbf{t}} d\Gamma + \int_\Omega \boldsymbol{\varsigma}^T \cdot \mathbf{g} d\Omega, \quad \forall\boldsymbol{\varsigma} \in \boldsymbol{\Sigma} \end{aligned} \tag{3.16}$$

Functions Θ, $\mathbf{u}$, ω, and $\boldsymbol{\varsigma}$ belong to suitable function spaces $\mathcal{W}$, $\boldsymbol{\Sigma}$, $\mathcal{W}_0$, and $\boldsymbol{\Sigma}_0$, respectively.

3.3 Discrete Form

3.3.1 Temperature Field

The temperature field is assumed to be continuous over the domain and described by the standard finite element approximation:

$$\Theta^h(\mathbf{x},t) = \sum_{I\in\mathcal{S}} N_I^\theta(\mathbf{x}) T_I(t), \qquad \forall\mathbf{x} \in \Omega \tag{3.17}$$

where N_I^θ are the standard finite element shape functions corresponding to temperature, T_I is the time dependent nodal temperature change, and $\mathcal{S}$ is the set of all nodes in the domain.

3.3.2 Displacement Field

In the XFEM approach to DD, enrichments are prescribed in addition to the standard finite element approximation for displacement to satisfy the internal boundary condition in (3.10) [42, 57]. The enrichments reflect the discontinuities created by the presence of edge dislocations.

An edge dislocation α is described by the location of its core, the orientation of its glide plane, and its Burgers vector $\mathbf{b}^\alpha$ [6,42]. Level set functions are used to describe the position of the core relative to the glide plane, as well as specify the active part of the glide plane (i.e. where slip has occurred). Corresponding to each dislocation α, let there be two affine functions $f^\alpha(\mathbf{x}) = \alpha_0 + \alpha_i \mathbf{x}_i$ and $g^\alpha(\mathbf{x}) = \beta_0 + \beta_i \mathbf{x}_i$ such that $f^\alpha(\mathbf{x}) \perp g^\alpha(\mathbf{x})$. The glide plane of dislocation α is defined as the signed distance $f^\alpha(\mathbf{x}) = 0$; and the location of the core, by where $f^\alpha(\mathbf{x}) = 0$ and $g^\alpha(\mathbf{x}) = 0$ intersect. The active part of the glide plane Γ_d^α is defined where $f^\alpha(\mathbf{x}) = 0$ and $g^\alpha(\mathbf{x}) > 0$ (Fig. 3.2).

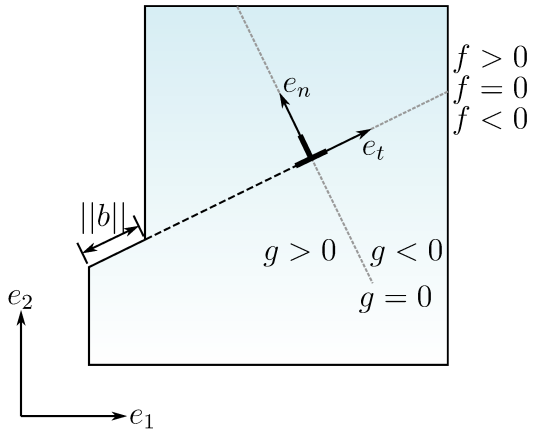

Figure 3.2: Illustration of level set functions f and g for a dislocation. The magnitude of the lattice distortion generated by the presence of the edge dislocation is represented by Burgers vector $\mathbf{b}$. Adapted from [42].

The XFEM enrichment introduces a jump in the displacement field across the glide plane in the manner of the Volterra model. For an edge dislocation, this lattice distortion is defined in the direction tangential to the slip plane, i.e. in the direction of the Burgers vector $\mathbf{b}^\alpha$. The tangential step enrichment following Gracie et al. [42, 57] is adopted and locally applied only to the nodes of elements intersected by the active part of the glide plane. Let

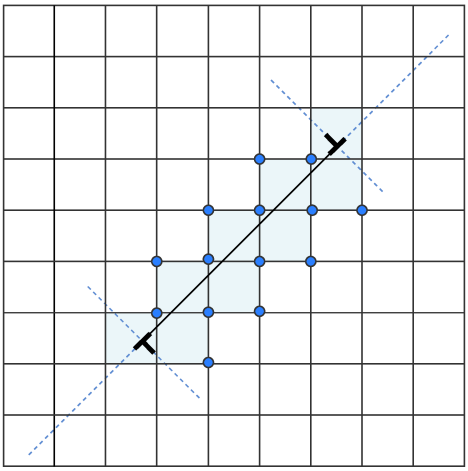

Figure 3.3: Illustration of enriched elements and nodes. Nodes in the set S^α are represented by blue circles. Shaded elements contain one or more enriched nodes.

the subset $\mathcal{S}^\alpha \in \mathcal{S}$ as the set of nodes with supports cut by Γ_d^α as illustrated in Fig. 3.3. The XFEM local displacement approximation for a domain with n_d edge dislocations is

$$\mathbf{u}^h(\mathbf{x},t) = \underbrace{\sum_{I\in\mathcal{S}} N_I^u(\mathbf{x})\mathbf{d}_I(\mathbf{x},t)}_{\text{FEM}} + \underbrace{\sum_{\alpha=1}^{n_d} \mathbf{b}^\alpha \sum_{J\in\mathcal{S}^\alpha} N_J^u(\mathbf{x})\left[H(f^\alpha(\mathbf{x},t)) - H(f^\alpha(\mathbf{x}_J,t))\right]}_{\text{XFEM enrichment}} \tag{3.18}$$

$$H(z) = \begin{cases} 1 & ,\text{if } z > 0 \\ 0 & ,\text{otherwise} \end{cases} \tag{3.19}$$

where N_I^u are the standard FEM shape functions, $\mathbf{d}_I$ are the nodal degrees of freedom, $\mathbf{b}^\alpha$ are the Burgers vectors of dislocation α, $\mathbf{x}_J$ are the coordinates of node J, f^α is the signed distance fo Γ_d^α, and H is the Heaviside step function in (3.19).

Acceleration is approximated as the derivative of (3.18) with respect to time. Since the Burgers vector of the dislocation remains constant in time, the enriched term evaluates to zero and acceleration is defined as in standard FEM.

3.3.3 Discrete Form

The semi-discrete system of equations is obtained using Galerkin's method with field approximations (3.17) and (3.18) and weak forms (3.15) and (3.16):

$$\begin{bmatrix} \mathbf{M}^{uu} & 0 \\ 0 & 0 \end{bmatrix} \begin{Bmatrix} \ddot{\mathbf{u}} \\ \ddot{\mathbf{\Theta}} \end{Bmatrix} + \begin{bmatrix} \mathbf{C}^{uu} & 0 \\ 0 & \mathbf{C}^{\Theta\Theta} \end{bmatrix} \begin{Bmatrix} \dot{\mathbf{u}} \\ \dot{\mathbf{\Theta}} \end{Bmatrix} + \begin{bmatrix} \mathbf{K}^{uu} & \mathbf{K}^{u\Theta} \\ 0 & \mathbf{K}^{\Theta\Theta} \end{bmatrix} \begin{Bmatrix} \mathbf{u} \\ \mathbf{\Theta} \end{Bmatrix} = \begin{bmatrix} \mathbf{F}^{u,ext} \\ \mathbf{F}^{\Theta,ext} \end{bmatrix} + \begin{bmatrix} \mathbf{F}^{\alpha} \\ \mathbf{F}^{TM} \end{bmatrix} \tag{3.20}$$

where $\mathbf{u} = \begin{bmatrix} \mathbf{d}_1 & \mathbf{d}_2 & \dots & \mathbf{d}_n \end{bmatrix}^T$ and $\mathbf{\Theta} = \begin{bmatrix} T_1 & T_2 & \dots & T_n \end{bmatrix}^T$ are the standard displacement nodal degrees of freedom and the nodal temperature changes, respectively, for n number of nodes. The sub-matrices are individually defined in (3.21) to (3.30). The structural damping term $\mathbf{C}^{uu}$ is introduced to the discrete equation but is not explicitly part of the strong form. It is noted that Burgers vector $\mathbf{b}^{\alpha}$ are to be prescribed and so appear on the right hand side of (3.20) in $\mathbf{F}^{\alpha}$. The external nodal forces induced in the elastic continuum through the introduction of dislocation α is represented by $\mathbf{F}^{\alpha}$.

$$\mathbf{M}^{uu}_{IJ} = \int_{\Omega} \mathbf{N}^{uT}_{I} \rho \mathbf{N}^{u}_{J} d\Omega, \qquad I, J \in \mathcal{S} \tag{3.21}$$

$$\mathbf{C}^{uu}_{IJ} = \alpha^{\xi} \mathbf{M}^{uu}_{IJ} + \beta^{\xi} \mathbf{K}^{uu}_{IJ}, \qquad I, J \in \mathcal{S} \tag{3.22}$$

$$\mathbf{C}^{\Theta\Theta}_{IJ} = \int_{\Omega} \mathbf{N}^{\Theta T}_{I} C_p \rho \mathbf{N}^{\Theta}_{J} d\Omega, \qquad I, J \in \mathcal{S} \tag{3.23}$$

$$\mathbf{K}^{uu}_{IJ} = \int_{\Omega} \mathbf{B}^{uT}_{I} \mathbf{C} \mathbf{B}^{u}_{J} d\Omega, \qquad I, J \in \mathcal{S} \tag{3.24}$$

$$\mathbf{K}^{u\Theta}_{IJ} = \int_{\Omega} \mathbf{B}^{uT}_{I} \boldsymbol{\lambda} \mathbf{N}^{\Theta}_{J} d\Omega, \qquad I, J \in \mathcal{S} \tag{3.25}$$

$$\mathbf{K}^{\Theta\Theta}_{IJ} = \int_{\Omega} \mathbf{B}^{\Theta T}_{I} k \mathbf{B}^{\Theta}_{J} d\Omega, \qquad I, J \in \mathcal{S} \tag{3.26}$$

$$\mathbf{F}^{u,ext}_{I} = \int_{\Gamma_t} \mathbf{N}^{uT}_{I} \bar{\mathbf{t}} d\Gamma + \int_{\Omega} \mathbf{N}^{uT}_{I} \mathbf{g} d\Omega, \qquad I \in \mathcal{S} \tag{3.27}$$

$$\mathbf{F}_I^{\Theta,ext} = -\int_{\Gamma_h} \mathbf{N}_i^{\Theta^T} \bar{\mathbf{h}} d\Gamma, \qquad I \in \mathcal{S} \tag{3.28}$$

$$\mathbf{F}_I^{TM} = -\int_{\Omega} \mathbf{N}_I^{\Theta^T} S(\mathbf{x}, t) d\Omega, \qquad I \in \mathcal{S} \tag{3.29}$$

$$\mathbf{F}_I^{\alpha} = \sum_{\alpha=1}^{n_d} \int_{\Omega} \mathbf{B}_I^{u^T} \mathbf{C} \mathcal{B}_{\alpha}^{u} \mathbf{b}^{\alpha} d\Omega, \qquad I \in \mathcal{S} \tag{3.30}$$

where

$$\mathbf{N}_I^u = \begin{bmatrix} N_I^u(\mathbf{x}) & 0 \\ 0 & N_I^u(\mathbf{x}) \end{bmatrix} \tag{3.31}$$

$$\mathcal{N}_{\alpha}^{u} = \sum_{J \in \mathcal{S}^{\alpha}} \begin{bmatrix} N_J^u(\mathbf{x}) \mathcal{H}_J^f \alpha & 0 \\ 0 & N_J^u(\mathbf{x}) \mathcal{H}_J^f \alpha \end{bmatrix} \tag{3.32}$$

$$\mathbf{B}_I^u = \begin{bmatrix} N_I^u(\mathbf{x})_{,x} & 0 \\ 0 & N_I^u(\mathbf{x})_{,y} \\ N_I^u(\mathbf{x})_{,y} & N_I^u(\mathbf{x})_{,x} \end{bmatrix} \tag{3.33}$$

$$\mathbf{B}_I^{\Theta} = \begin{bmatrix} N_I^{\Theta}(\mathbf{x})_{,x} \\ N_I^{\Theta}(\mathbf{x})_{,y} \end{bmatrix} \tag{3.34}$$

$$\mathcal{B}_{\alpha}^{u} = \sum_{J \in \int^{\alpha}} [\mathcal{B}_J^u] \tag{3.35}$$

$$\mathcal{B}_J^u = \begin{bmatrix} N_J^u(\mathbf{x})_{,x} \mathcal{H}_J^{\alpha} & 0 \\ 0 & N_J^u(\mathbf{x})_{,y} \mathcal{H}_J^{\alpha} \\ N_J^u(\mathbf{x})_{,y} \mathcal{H}_J^{\alpha} & N_J^u(\mathbf{x})_{,x} \mathcal{H}_J^{\alpha} \end{bmatrix} \tag{3.36}$$

$$\mathcal{H}_J^{\alpha} = H(f^{\alpha}(\mathbf{X})) - H(f^{\alpha}(\mathbf{x}_J)) \tag{3.37}$$

3.4 Time Integration

Equation (3.20) is solved sequentially. First, given nodal displacements $\mathbf{u}^s$ and temperature $\mathbf{\Theta}^s$ at time t^s, a Crank-Nicolson scheme is used to obtain nodal temperature $\mathbf{\Theta}^{s+1}$ at time t^{s+1} [68]. The solution scheme of the parabolic thermal problem is as follows:

$$\bar{\mathbf{K}}^{s-1}\mathbf{\Theta}^s = \hat{\mathbf{F}}^{s,s-1} \tag{3.38}$$

where

$$\bar{\mathbf{K}}^s = \left(\mathbf{C}^{\Theta\Theta} + \frac{\Delta t}{2}\mathbf{K}^{\Theta\Theta}\right)^s \tag{3.39}$$

$$\hat{\mathbf{F}}^{s,s-1} = \mathbf{C}^{\Theta\Theta}\left(\Theta + \frac{\Delta t}{2}\dot{\Theta}\right)^{s-1} + \frac{\Delta t}{2}\left(\mathbf{F}^{\Theta,ext} + \mathbf{F}^{TM}\right)^s \tag{3.40}$$

where Δt denotes the size of the time step; the superscripted s indicates the time step, i.e. $(\bullet)^{s\pm1}$ denotes time $t \pm \Delta t$.; and the superimposed dot represents the first material time derivative.

Next, given the nodal displacements $\mathbf{d}^s$ and $\mathbf{d}^{s-1}$, and nodal temperatures $\mathbf{\Theta}^{s+1}$ a second-order explicit central-difference method is used to update the mechanical problem. Thus, a one time-step lag in the thermal effect is introduced to the mechanical solution. The solution scheme of the hyperbolic mechanical problem is as follows:

$$\ddot{\mathbf{u}}^s = \mathbf{M}^{-1}\left((\mathbf{F}^{u,ext} + \mathbf{F}^{\alpha})^s - \mathbf{C}^{uu}\dot{\mathbf{u}}^{s-\frac{1}{2}} - \mathbf{K}^{uu}\mathbf{u}^s\right) \tag{3.41}$$

$$\dot{\mathbf{u}}^{s+1/2} = \dot{\mathbf{u}}^{s-1/2} + \ddot{\mathbf{u}}^s\Delta t \tag{3.42}$$

$$\mathbf{u}^{s+1} = \mathbf{u}^s + \dot{\mathbf{u}}^{s+1/2}\Delta t \tag{3.43}$$

where Δt denotes the size of the time step; the superscripted s indicates the time step, i.e. $(\bullet)^{s\pm1}$ denotes time $t \pm \Delta t$; and the superimposed dot and double dot represent the first and second material time derivative, respectively.

3.4.1 Critical Time Step and Damping

The critical time step for the elastic domain problem Δt^{Ω}_{crit} is limited by the maximum eigenfrequency of the system ω_{max} and influenced by damping [69]. The linear eigenfrequencies of the system ω_i are obtained by assuming a solution (3.44) for the free vibration

equation of motion for the system (3.45) and solving the expression of the determinant in (3.46).

$$\mathbf{u} = \mathbf{U}sin(\omega_i t + \alpha) \tag{3.44}$$

$$[\mathbf{M}]\ddot{\mathbf{u}} + [\mathbf{K}]\mathbf{u} = \mathbf{F}^{ext} \tag{3.45}$$

$$|\mathbf{K} - \omega_i^2 \mathbf{M}| = 0 \tag{3.46}$$

A small amount of numerical damping is provided to control high frequency oscillations. Damping was assumed to be of the Rayleigh type, i.e. linearly proportional to mass and stiffness through the relationship in (3.22). The proportionality coefficients α^{ξ} and β^{ξ} for material damping term $\mathbf{C}^{uu}$ are determined as follows

$$\beta^{\xi} = \frac{2(\xi_1 \omega_{n,1} - \xi_2 \omega_{n,2})}{\omega_{n,1}^2 - \omega_{n,2}^2} \tag{3.47}$$

$$\alpha^{\xi} = 2\xi_1 \omega_{n,1} - \beta^{\xi} \omega_{n,1}^2 \tag{3.48}$$

where ξ_1 and ξ_2 are the damping ratios, and $\omega_{n,1}$ and $\omega_{n,2}$ are the eigenfrequencies of the first and second modes of vibration. Due to a lag in velocity using a second-order explicit method, the critical time step is decreased due to damping [69]:

$$\Delta t_{crit}^{\Omega} = \frac{2}{\omega_{n,max}} (\sqrt{\xi_n^2 + 1} - \xi_n) \tag{3.49}$$

where ξ is the primary damping ratio.

Chapter 4

Implementation of Dislocation Theory

The conventional DD formulation describes plasticity through the collective motion of dislocations in a linear-elastic solid [10]. The behaviour of dislocations is explicitly simulated and regulated by interaction mechanisms described in the *Theory of Dislocations* by [5]. The DTM-DD follows the planar method of the DDP proposed by Van der Giessen & Needleman [27] whereupon the three-dimensional physical problem is simplified into a two-dimensional one. As a result of this spatial simplification, only infinite straight edge dislocations are simulated under plane strain conditions as cross-slip mechanisms are implicitly assumed to not govern dislocation mechanisms.

Edge dislocation lines are reduced to points on the planar domain and are characterized by the location of its core and the orientation of its Burgers vector. Dislocation motion is assumed to be restricted along its glide plane in the form of glide-only motion; collectively, this motion is manifested as *slip*. Slip systems are defined as straight lines within the domain and oriented to resemble the crystallography of a chosen material. Dislocation sources and obstacles are also modeled as points on slip plane lines.

In this chapter, the implementation of key dislocation mechanisms in the DTM-DD is discussed. First, the topic of dislocation mobility is addressed: the phenomenological equations and significant terms within are presented, ex. the Peach-Koehler driving force, dislocation mass, and dislocation drag. Commentary is provided on the definition of dislocation parameters and selection of values used in simulation. The characterization of a dislocation as a moving heat source, and the mechanisms of dislocation nucleation and interaction are introduced. Finally, the computational algorithm of the DTM-DD is pre-

sented.

4.1 Mobility

The concept of dislocation motion was introduced in Sec. 2.1.3. As the DTM-DD is intended for high strain-rate simulations, climb motion is neglected and only glide motion, i.e. along dislocation slip planes, is considered. The phenomenological equation of dislocation motion is presented with its numerical scheme, and key terms are discussed. Newtonian physics presents a balance between applied force and induced motion. The induced motion, in reality, is fully dynamic. The DTM-DD captures the dynamics of dislocation motion in addition to the elastodynamics in the thermocoupled domain. The force driving dislocation motion is expressed by the Peach-Koehler force which includes both thermal and dynamic effects. Consideration of inertia also requires the consideration of the mass of the object in motion; hence, dislocation mass is presented. Intuitively, obstacles and interactions aside, dislocations will not perpetually remain in motion. Energy dissipation is expressed as dislocation "drag", a form of damping, which we present in the DTM-DD as temperature dependent.

4.1.1 Equation of Motion and the Viscous Drag Law

Dislocation motion is characterized into three distinct regimes: thermally-activated, drag-controlled, and relativistic behavior [12]. The thermal activation regime is associated with low applied stresses (and low strain-rates up to $\dot{\varepsilon} = 10^3\ s^{-1}$) whereupon dislocation motion is hindered by the intrinsic resistance of the crystal lattice [10, 70]. In contrast, the relativistic regime is associated with ultra-high strain rates, typically in the excess of $10^{10}\ s^{-1}$, where dislocation velocities approach the transverse speed of sound and the effect of the change of mass is referred to as relativistic behavior [10]. In this thesis, particular interested is paid to the intermediary strain-rates between $\dot{\varepsilon} = 10^3$ to $10^5\ s^{-1}$ where the glissile motion of dislocations in crystalline metals is, in the same manner as fluid motion, impeded by a viscous drag force in a drag-controlled regime [10]. Dissipation of energy through transfer of momentum occurs when phonons and conduction electrons in metals are scattered through interactions with moving dislocations [5].

The motion of dislocation α is described as viscous-drag controlled using the phenomenological equation of motion

$$m^{\alpha}\dot{\mathbf{v}}^{\alpha} + \mathbf{B} \cdot \mathbf{v}^{\alpha} = \mathbf{F}^{\alpha} \tag{4.1}$$

where m^α is the mass of dislocation α; $\mathbf{B} = \mathbf{B}(\mathbf{x}^\alpha, \Theta(\mathbf{x}^\alpha, t))$ is the tensor of dislocation drag which is dependent on the temperature at the location of dislocation α, $\mathbf{x}^\alpha$; $\mathbf{F}^\alpha$ is the force per unit length that must be applied to dislocation α to maintain a uniform velocity of $\mathbf{v}^\alpha$; and $\dot{\mathbf{v}}^\alpha$ is the acceleration of dislocation α. The conventional formulation of dislocation motion as used in [6, 10, 47] is quasi-static which assumes that motion is overdamped. The inertial term $\dot{\mathbf{v}}^\alpha$ in (4.1) is neglected and the force-velocity is linear, i.e. $\mathbf{B} \cdot \mathbf{v}^\alpha = \mathbf{F}^\alpha$.

In the three-dimensional DD simulations by Wang et al. [61], and also earlier in two-dimensions by Roos et al. [13], the fully dynamic dislocation equation of motion in (4.1) was implemented and compared to conventional quasi-static formulation for a range of strain-rates. For the lower end of drag-controlled strain rates between $10^2\ s^{-1}$ and $10^3\ s^{-1}$, results from the fully dynamic and quasi-static simulations were found to be minimally different. However, at strain-rates between $10^3\ s^{-1}$ and $10^6\ s^{-1}$, Wang et al. [61] observed that the inclusion of inertial terms for dislocation motion captures dislocation motion much more accurately than the overdamped approximation. They conclude that the finite time required for dislocations to change velocities under an applied force is non-negligible for high strain-rate simulations. Thus, the full equation of motion with inertial terms was adopted in this investigation.

A first-order explicit Forward Euler scheme was adopted following Wang et al. [61] to determine dislocation velocity and subsequently displacement, i.e.

$$\begin{aligned} \dot{\mathbf{v}}^\alpha_{s+1} &= (m^\alpha)^{-1} \left(\mathbf{F}^\alpha_s - \mathbf{B} \cdot \mathbf{v}^\alpha_s\right) \\ \mathbf{v}^\alpha_{s+1} &= \mathbf{v}_s + \dot{\mathbf{v}}^\alpha_{s+1} \Delta s \\ \mathbf{d}^\alpha_{s+1} &= \mathbf{d}^\alpha_s + \frac{1}{2}(\mathbf{v}^\alpha_s + \mathbf{v}^\alpha_{s+1})\Delta s \end{aligned} \tag{4.2}$$

where Δs denotes the size of the time step; the subscripted s indicates the time, i.e. $(\bullet)_{s\pm1}$ denotes time $s \pm \Delta s$; and the superimposed dot represents the material time derivative.

4.1.2 The Peach-Koehler Force

The force acting on a defect singularity within a continuum is influenced by both externally applied loads as well as the internal stress fields generated by other such singularities within the medium [26]. The eponymous Peach-Koehler force expresses the force on a dislocation in a continuum in its most general form: the force $\mathbf{F}$ for the unit length of a dislocation line δs is

$$\mathbf{F} = -\bar{\boldsymbol{\xi}} \times (\bar{\boldsymbol{\sigma}} \cdot \mathbf{b}) \delta s \tag{4.3}$$

where $\bar{\boldsymbol{\xi}}$ is a unit vector along the dislocation line s, $\bar{\boldsymbol{\sigma}}$ is the stress at δs from all sources except self-stress along δs, and $\mathbf{b}$ is the Burgers vector [42].

Eshelby [55] (and independently by Cherepanov [71]), developed a surface integral to determine the force on a singularity for the generalized three-dimensional case. Rice's path-independent J-integral reduces the surface integral to a two-dimensional contour integral (4.4) [72]. The J-integral has been extensively used in fracture mechanics applications, particularly with crack-tip propagation. The Eshelby tensor – also known as the energy-momentum tensor – is integrated over a path-independent contour enclosing the singularity:

$$F_l = \int_{\Gamma_c} \left(\frac{1}{2} \sigma_{ij} \varepsilon_{ij} \delta_{kl} - \sigma_{ik} u_{i,l} \right) n_k d\Gamma \tag{4.4}$$

where Γ_c is any closed contour around a dislocation core with an outward normal $\mathbf{n}$ [42,72].

For a plane crack extension problem, the J-integral is equivalent to the strain energy release rate per unit fracture surface area, i.e.

$$J \equiv G = -\frac{\partial U}{\partial A} \tag{4.5}$$

where U is the potential energy available for crack growth, and A is the crack area (or length for two-dimensional problems). In a simply connected domain, i.e. if the domain contains no stress singularities, the J-integral evaluates to zero. Physically, the J-integral represents the force driving a crack to propagate [73]. In the case of a dislocation, the J-integral is the change in potential elastic energy with respect to the change in dislocation position, and is equivalent to the Peach-Koehler force.

Kishimoto et al. [73] provide an extension to Rice's original definition of the path-independent J-integral. Their extended path-independent $\hat{J}$-integral (4.6) accounts for thermal strains, body forces, and inertial forces. The $\hat{J}$-integral represents the energy release rate in an arbitrary material during crack extension and is equivalent to the Peach-Koehler force in a dynamic and thermoelastic system. [73]. The Peach-Koehler force acting on dislocation α is defined as

$$F_k^\alpha = \hat{J}_k = \int_{\Gamma_C^\alpha} \left\{ W^e n_k - T_i \frac{\partial u_i}{\partial X_k} \right\} d\Gamma_c^\alpha + \int_{\Omega^\alpha} \left\{ \sigma_{ij} \frac{\partial \varepsilon_{ij}^*}{\partial X_k} + (\rho \ddot{u}_i - F_i) \frac{\partial u_i}{\partial X_k} \right\} d\Omega^\alpha \tag{4.6}$$

where W^e is the elastic strain energy density function (4.8). The first integral on the right-hand-side reflects the coupled elasto-static contribution; and the second term, contributions from additional forms of strain energy, inertia, and body force. The strain tensor ε_{ij} is decomposed into elastic and eigen-strain components ε_{ij}^e and ε_{ij}^*, respectively, as in (4.7).

Eigen-strains are inelastic and stress-free, and are inclusive of thermal or plastic strain components [73].

$$\varepsilon_{ij} = \varepsilon^e_{ij} + \varepsilon^*_{ij} \tag{4.7}$$

$$W^e = \int_0^{\varepsilon^e_{ij}} \sigma_{ij} d\varepsilon^e_{ij} \tag{4.8}$$

We assume that the eigen-strains of the system is wholly exemplified by elastic thermal strains in the form $\varepsilon^*_{ij} = \gamma_{ij}\Theta$, where for an isotropic assumption $\gamma_{ij} = \delta_{ij}\gamma_1\Theta$ [73]. In the case of plane strain, $\gamma_1 = (1+\nu)\gamma$, where ν is Poisson's ratio and γ is the coefficient of linear thermal expansion. The thermo-coupling in the system is incorporated in two ways. First, the elastic strain in the energy density function (4.8) is replaced with thermo-coupled strain, which results in an elastic strain energy density function in the form of (4.12). Second, the thermal contribution to the $\hat{J}$-integral in (4.6) translates to a domain integral

$$F^\Theta_k = \hat{J}^\Theta_k = \int_{\Omega^\alpha} \gamma_1 \delta_{ij} \sigma_{ij} \Theta_{,k} d\Omega^\alpha = \int_{\Omega^\alpha} \gamma_1 \sigma_{ii} \Theta_{,k} d\Omega^\alpha \tag{4.9}$$

Similarly, body force contributions are in the form of a domain integral

$$F^{\text{body}}_k = \hat{J}^{\text{body}}_k = -\int_{\Omega^\alpha} g_i u_{i,k} d\Omega^\alpha \tag{4.10}$$

The extension of the crack tip is time dependent: the crack tip area and boundary, A and Γ, respectively, translate with the crack tip. Then (4.6) expands to the following form:

$$\begin{aligned} F^\alpha_k &= \hat{J}_k \\ &= \int_{\Gamma^\alpha_c} \{W^e - \sigma_{ik} u_{i,k} + \frac{1}{2}\rho \dot{u}_i \dot{u}_i\} n_k d\Gamma^\alpha_c + \int_{\Omega^\alpha} \{\rho \ddot{u}_i u_{i,k} - \rho \dot{u}_i \dot{u}_{i,k}\} d\Omega^\alpha + \hat{J}^\Theta_k + \hat{J}^{\text{body}}_k \end{aligned} \tag{4.11}$$

$$W^e = \frac{1}{2}\left(\sigma_{ij}\left(\varepsilon_{ij} - \delta_{ij}\gamma_1\Theta\right)\right) \tag{4.12}$$

where Γ^α_c is any closed contour about the core of dislocation α; Ω^α is the area bounded by Γ^α_c; $\mathbf{n}$ is the outwards unit normal to Γ^α_c; the superimposed dots on u represent the material time derivatives. Inertial effects are incorporated within the contour integral as well as through the additional domain integral.

4.1.3 Dislocation Mass

The effective mass of a moving edge dislocation m^α was defined by Hirth et al. [74] based on expressions of total energy Π, kinetic energy Π_K, and strain energy Π_s for a unit length of dislocation. The total energy Π is a function of dislocation drag B which, if temperature effects are considered, is implicitly a function of temperature. Although temperature dependence was recognized by Hirth et al. [74], B as well as other material elastic constants are assumed to be temperature independent in the definition of dislocation mass.

The thermodynamic inertial force F is defined as a function of velocity where

$$F(v) = \frac{1}{v}\left(\frac{d\Pi}{dv}\right)\frac{dv}{dt} \equiv m^\alpha \frac{dv}{dt} \tag{4.13}$$

where m^α is the effective mass for a moving dislocation. For an edge dislocation moving at a velocity v [74],

$$m^\alpha(v) = \frac{\Pi_0 C_t^2}{v^4}(-9\gamma_l - 20\gamma_l^{-1} + 4\gamma_l^{-3} + 7\gamma + 25\gamma^{-1} - 11\gamma^{-3} + 3\gamma^{-5}) \tag{4.14}$$

where Π_0 is energy of the stationary system or the "rest energy factor" (4.15); C_t and C_l is the transverse and longitudinal sound velocity, respectively (4.16); $\gamma_l = (1 - v^2/C_l^2)^{1/2}$; and $\gamma = (1 - v^2/C_t^2)^{1/2}$.

$$\Pi_0 = \frac{\mu b^2}{4\pi} ln\left(\frac{R}{r_0}\right) \tag{4.15}$$

$$C_t = \left(\frac{\mu}{\rho_0}\right)^{1/2} \qquad C_l = \left(\frac{\lambda + 2\mu}{\rho_0}\right)^{1/2} \tag{4.16}$$

where μ is the shear modulus, b is the magnitude of the Burgers vector, and R and r_0 are the outer and inner radii in the integration of energy terms [5]. Typically, $r_0 = b$ is chosen to exclude the dislocation core; and R, to make $\Pi_0 = \mu b^2$.

At small velocities (v up to $0.1C_t$), the effective mass of an edge dislocation simplifies to

$$m^\alpha = \frac{\mu b^2}{C_t^2} \cdot \left(1 + \frac{C_t^4}{C_l^4}\right) \tag{4.17}$$

4.1.4 Temperature Dependence of the Drag Coefficient

At high strain-rates, dislocation motion is described as viscous-drag controlled as in (4.1), and viscous forces are described by the viscous drag coefficient, B [75]. The characterization of parameter B in close-packed metals has been accomplished through three main types of experimental techniques: indirectly through the measurement of internal friction, and of stress versus strain-rate; and directly through the measurement of dislocation displacement. For a good overview of these experimental techniques and theories of viscous drag, we refer to [75] and [76]. Most of the literature on drag and temperature dependence refer to single- and poly-crystalline aluminum.

The attenuation of the vibrations in a dislocation network is indirectly used to measure B with the internal friction method. A dislocation network is vibrated using low amplitude alternating stresses. The energy dissipated through viscous damping is reflected by the decay in the stress amplitude, and B is then determined from the energy decrement between cycles [75]. Although this method does not require presupposition of the geometry of the dislocation network, for example knowledge of the pinning points along dislocation lengths, it requires an assumption of the mobile dislocation density, ρ_m [75,77]. Using measurements of internal friction, Mason & Rosenberg [78], Mason [79], and Sylwestrowicz [80] investigated single crystal aluminum; and Hutchinson & Rogers [81], poly-crystals. Similarly, Alers & Thompson [82] investigated single crystal copper; results were subsequently refined by Mason [78] and Jassby & Vreeland [75]. The dislocation velocities prompted by this technique are typically less than 10^{-1} m/s, which correspond to low strain-rate loading.

Conversely, B may also be indirectly determined through the measurement of stress and strain. Particularly for high strain-rate experiments (10^3 to 10^5 s^{-1}), dislocation velocity typically exceed 10 m/s and is controlled by drag only. Then B is determined through the linear relationship $B = \alpha\rho_m b^2$ [75], where parameter α is experimentally determined through a linear relationship between stress and strain-rate as identified by Kumar & Kumble [83]. Again, ρ_m is an estimated value and is here independent of stress [84]. Yoshida & Nagata [85] investigated B via measurements of stress and strain-rate for high strain-rate single- and polycrystal copper and noted that, for $T < 293K$, drag decreases with decreasing temperature. Ferguson et al. [84] report values for single crystal aluminum obtained at strain rates of 10^4 s^{-1}; and Nadgornyi [86], for high velocity dislocations.

In contrast, B may be directly determined through the measurement of dislocation displacement as a result of an applied stress pulse with known duration and amplitude. Torsional stress pulses have been particularly effective for obtaining results for copper, as in the results by Jassby & Vreeland [75,87]. The amplitude of the stress pulse must be sufficiently

large to produce viscous-controlled velocity. Thus, this method requires that the applied stress is significantly greater than both internal and critical unpinning stresses otherwise B is overestimated. Additionally, this technique becomes impractical when dislocation density high and difficult to employ when dislocation velocities reach the speed of sound. Paramswaran et al. [88] and Gorman et al. [77] report measurements for single crystal aluminum using a direct displacement measurement technique.

Hikata et al. [89, 90] utilize a variant of the internal friction method by measurement of ultrasonic attenuation changes resulting from a "dynamic bias stress".This method does not require knowledge of dislocation density or features of the dislocation network *a priori*. Olmsted [91] conducted MD simulations replicating trials by Hikata et al. [89, 90]. Experimental results from the various discussed techniques for aluminum and copper, as well as the MD simulation results by [91] are replicated in Fig. 4.1.

As noted by Jassby & Vreeland [75] and Parmeswaran et al. [88], the absolute values of B measured by the various investigators differ by an order of 10^2, which is too large to be ascribed to experimental error. Generally for $T \gtrsim 100K$, B increases with increasing temperature. At low temperatures however, ex. $T \lesssim 100K$, experimental results may be grouped into three main behavioural trends. First, Mason & Rosenberg [78], Mason [79], Ferguson et al. [84], and Hutchinson & Rogers [81] are in qualitative agreement with the behaviour predicted using theory of electron drag as presented by [78]: at low temperatures, B increases with decreasing temperature. A key assumption of this theory is that the wavelength of lattice strain is significantly less than the mean free path of an electron. This assumption is violated at a moving dislocation core where most of the energy is dissipated [88]. However, the same trend is also reported in the results by Parmeswaran et al. [88] which uses the displacement measurement technique as opposed to internal friction. Additionally, [88] report this behaviour in dislocations within other fcc-type materials including lead and potassium. Comparatively, the trends of results from Alers & Thomspon [82], Gorman et al. [77, 92], and Vreeland [93] appear to qualitatively agree with the theory of phonon drag by Mason & Rosenberg [78] where, at low temperatures, B is expected to decrease with decreasing temperatures. Lastly, Hikata et al. [89] find no temperature dependence of B at low temperatures.

Thus, the behaviour of B at low temperatures is directly contradictory between experimental techniques, and cannot be theoretically verified using the current understanding of drag mechanisms [75]. In this thesis, investigations are performed at moderate temperatures above $100K$ where experimental trends are more consistent. Mobility is assumed to be temperature dependent, analogous to the electro-mechanical DD model by [6]. Following experimental trends, the drag coefficient of dislocation α, B^α, was assumed to be positively

correlated to temperature change. For simplicity, a linear correlation was assumed:

$$B^{\alpha} = B_0 + B_1\Theta(t) \tag{4.18}$$

where B_0 is the dislocation drag corresponding to the reference temperature Θ_0; B_1 is the rate the drag coefficient grows with the increase in temperature ($B_1 \geq 0$); $\Theta_{\alpha}(t)$ is the temperature rise with respect to Θ_0 at the position of dislocation α, $\mathbf{x}_{\alpha}$, at time t; and $\Theta(t) = \Theta_{\alpha}(t) + \Theta_0$. In implementation, each dislocation is subjected to a different value of drag. The characterization of B^{α} can be refined using a non-linear description of its temperature dependence.

A significantly larger set of experimental data is required to fully characterize parameter B_1. However, due to the limited relevant experimental data, the statistics of the available data were considered indicative of the magnitude of drag-temperature dependence. In particular, the experimental data for aluminum was utilized as it forms a larger fraction of the available data. Linear regression was performed on each set of experimental data in Fig. 4.1a, for a subset of each data set with $T > 100K$. The data set from Ferguson et al. [84] was considered an outlier due to the negative temperature-drag dependence as compared to the positive dependence observed in all other sampled data. A linear temperature dependence of B_1 in the order of $10^{-7}\ Pa \cdot s$ with maximum and minimum values of $8 \cdot 10^{-7}\ Pa \cdot s/K$ and $0.2 \cdot 10^{-7}\ Pa \cdot s/K$, respectively, was observed. Collectively, the experimental subsets yield a mean and standard deviation for B_1 of $1.70 \cdot 10^{-7}\ Pa \cdot s/K$ and $2.63 \cdot 10^{-7}\ Pa \cdot s/K$ with an average R^2 value of 0.942.

At room temperature, Kubin et al. [40] report values of $B = 5 \cdot 10^{-5}\ Pa \cdot s$ and $10^{-4}\ Pa \cdot s$ for the simulation of copper and aluminum, respectively. However, a value of $B = 10^{-4}\ Pa \cdot s$ is generally assumed as a representative parameter for copper, ex. [6, 27, 94]. For the purpose of this thesis, a value of $B_0 = 10^{-4}\ Pa \cdot s$ was similarly assumed for copper for temperature independent models, i.e., $B_1 = 0$. In comparison, we assume $B_0 = 5 \cdot 10^{-5}\ Pa \cdot s$ for the temperature dependent models. The sensitivity of the dependence relationship with respect to material response may be investigated by performing a parametric study on B_1, as in Sec. 5.3.3.

4.2 Dislocations as a Heat Source

A feature of the thermomechanical DD model proposed by Skiba [6] is the treatment of dislocations as individual heat sources. The heat generated by each moving dislocation α, s^{α}, is described by the rate of work done by the Peach-Koehler force on the dislocation,

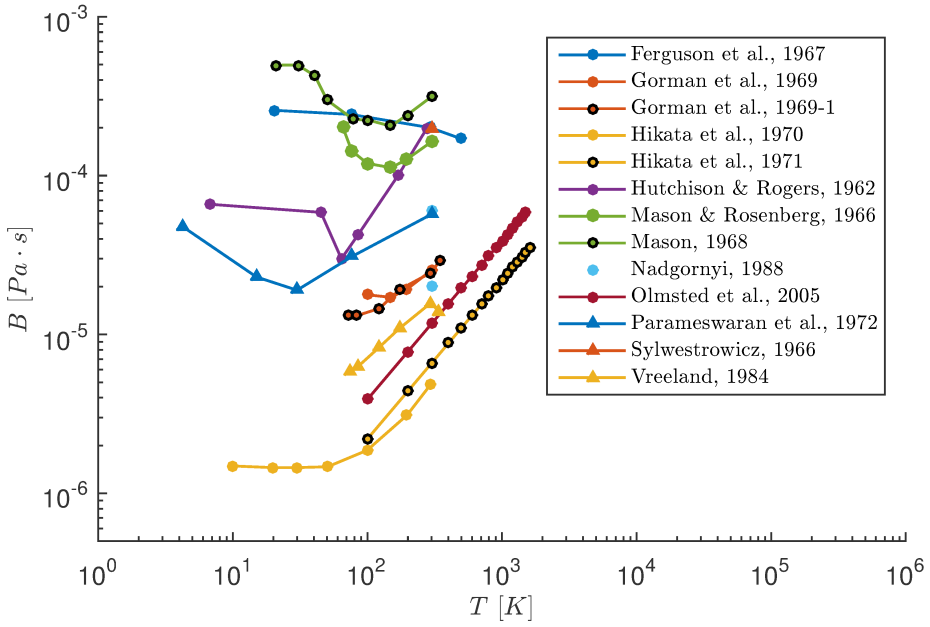

(a)

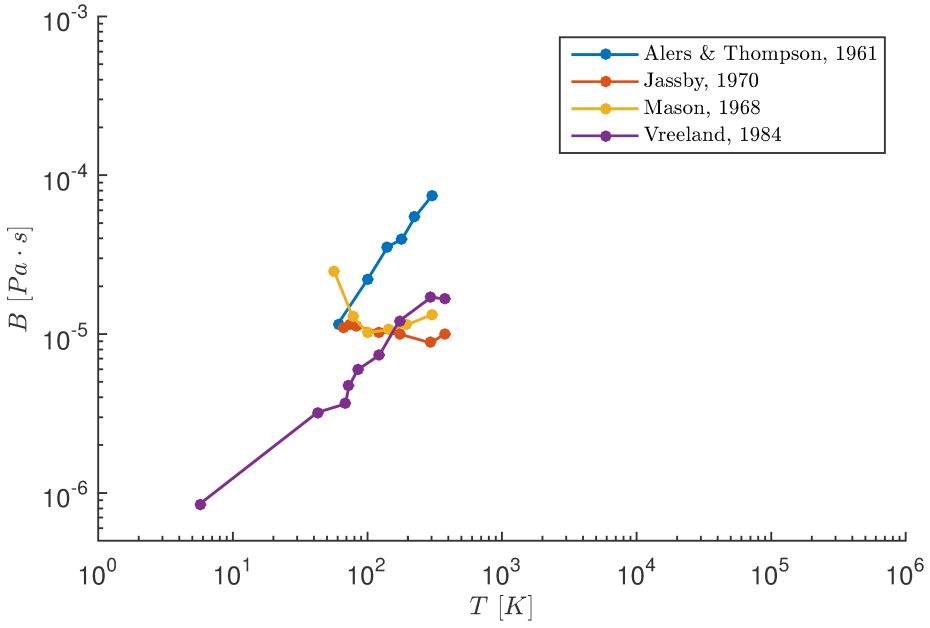

(b)

Figure 4.1: Experimental and simulation test data for temperature dependence of the drag coefficient for (a) Aluminum and (b) Copper.

i.e.,

$$s^{\alpha} = \beta \left(\mathbf{F}^{\alpha}(t) \cdot \mathbf{v}^{\alpha}(t) \right) \tag{4.19}$$

where $\mathbf{v}^{\alpha}$ is the velocity and $\mathbf{F}^{\alpha}$ is the Peach-Koehler force on dislocation α, respectively. The initial rate of work for all simulations is assumed to be zero due to the assumption that all dislocations are initially static.

The fraction of plastic work done that is converted into heat is described by coefficient β. Continuum studies, for example [95], indicate that this fraction is strain and strain-rate dependent. In the current work, β is assumed to be strain-rate independent with a a value between 0.8 and 1.0, inclusive, based on the observations of [96, 97].

4.3 Nucleation

The Frank-Read source was introduced as the method of dislocation nucleation in Sec. 2.1.4. The Frank-Read source itself is a dislocation segmented pinned at its ends. As such, in the DTM-DD sources are modeled as points on dislocations in the same manner as dislocations. In simulation, they are randomly generated at a prescribed density ρ_{src} on dislocation slip planes. The Frank-Read process is activated when the resolved shear stress acting on a Frank-Read source exceeds the critical activation stress (or *nucleation strength*), i.e. $|\tau| \geq \tau_{nuc}^{FR}$, and occurs over a time of t_{nuc}. The nucleated dislocation dipole is characterized by the size of the critical configuration L_{nuc}^{FR} and the orientation of the Burgers vectors based on the sign of the stress state on the source. Neglecting thermal effects, L_{nuc}^{FR} is approximated as

$$L_{nuc}^{FR} = \frac{E}{4\pi(1-\nu^2)} \cdot \frac{b}{\tau_{nuc}^{FR}} \tag{4.20}$$

where E is the material Young's modulus, ν is Poisson's ratio, b is the magnitude of Burgers vector of the Frank-Read source, and τ_{nuc}^{FR} is the nucleation strength [27].

Nucleation strength was assumed to be temperature dependent. Yield strength-temperature dependence, an observable material parameter, was used as an indicator towards the temperature dependence of nucleation strength, which is a simulation parameter. Experimentally determined yield strength of polycrystalline copper with average grain diameters between 0.020 mm and 0.120 mm is reported from [98–100] in Fig. 4.2 and display an overall negative relationship between yield strength and temperature. This trend is also observed by [101] in a numerical investigation of the nucleation rate of dislocations in bulk copper as a function of temperature and stress from a thermodynamic perspective using a

MD framework. They report a similar negative relationship between nucleation stress and temperature under constant shear loading at $\dot{\gamma} = 10^{-3}\ s^{-1}$.

The relationship between nucleation strength and temperature was assumed to be a N-th order polynomial, i.e.

$$\left\{\tau_{nuc}^{FR}\right\}^{N} = \tau_{N}^{FR}\Theta_{\alpha}^{N}(t) + \tau_{N-1}^{FR}\Theta_{\alpha}^{N-1}(t) + ... + \tau_{1}^{FR}\Theta_{\alpha}(t) + \tau_{0}^{FR} \tag{4.21}$$

where τ_0^{FR} is the critical activation stress corresponding to the reference temperature Θ_0; $\Theta_\alpha(t)$ is the temperature rise with respect to Θ_0 at the position of dislocation α $\mathbf{x}_\alpha$ at time t; and τ_{N-i}^{FR} is the rate the critical activation stress grows with the increase in the $(N-i)^{th}$ degree of temperature, Θ_α^{N-i}, for $0 \leq i \leq N-1$. Polynomial regression was performed on the data in Fig. 4.2 and $N = 3$ was found to provide a good fit for the data with a coefficient of determination of $R^2 = 0.8817$. Using a third order polynomial regression, the yield stress tends towards a constant value for temperatures below $273K$ and above $1000K$ as the material reaches its melting point, which we intuitively expect.

A value of 50 MPa is used as a representative value for nucleation strength in [6, 27, 40, 94, 102]. In order to prevent sources from simultaneously nucleating in simulation, sources are assigned a nucleation strength from a distribution function: traditionally Gaussian, as in [6, 15, 94, 102], with average $\bar{\tau}_{nuc}$ and standard deviation $\bar{\sigma}_{nuc}$; or log-normal, in [103, 104]. In this thesis, the nucleation strength of a Frank-Read source is described as a third-order polynomial:

$$\tau_{nuc}^{FR} = \tau_{3}^{FR}\Theta^{3}(t) + \tau_{2}^{FR}\Theta^{2}(t) + \tau_{1}^{FR}\Theta_{(}t) + \tau_{0}^{FR} \tag{4.22}$$

where $\Theta(t) = \Theta_\alpha(t) + \Theta_0$; $\tau_3^{FR} = 0.1476$; $\tau_2^{FR} = -258.87$; $\tau_1^{FR} = 64,123$; and τ_0^{FR} is assumed to have a Gaussian distribution with an average and standard deviation of $\bar{\tau}_{nuc} = 50 \cdot 10^6\ Pa$ and $\bar{\sigma}_{nuc} = 1 \cdot 10^6\ Pa$, respectively. The sensitivity of the material response on the nucleation strength may be investigated by performing a parametric study on the coefficients in (4.22) as in Sec. 5.3.4.

4.4 Interaction and Obstacles

Two forms of dislocation interaction mechanisms were implemented in the DTM-DD: (1) the interaction between dislocations; and (2), between dislocations and obstacles. Two edge dislocations with Burger's vectors equal in magnitude but opposite in sign, i.e. a dipole, will annihilate, presumably due to self-stresses, when sufficiently close to one another. This was implemented by assigning a material-dependent critical distance $L_e = 6b$, where b is the magnitude of the Burgers vector [27].

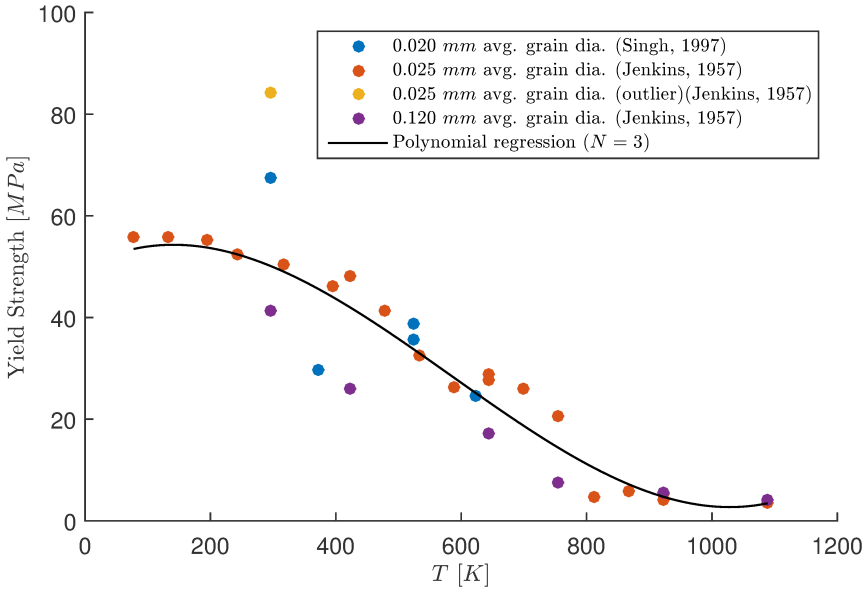

Figure 4.2: Experimental yield strength of copper fitted using third-order polynomial regression.

Obstacles or inclusions within the medium serve to obstruct the motion of dislocations along their slip plane. The leading dislocation – that is, the one closest to the obstacle – is "pinned" against the obstacle. Due to the obstruction of movement, a queue of dislocations form against an obstacle; this phenomena is termed *dislocation pileup* [5]. Pileup can also occur against grain boundaries in polycrystalline specimens. The leading dislocation is acted on by externally applied stresses, as well as by the cumulative forces from the dislocations in the queue. Pileup continues until the force on the leading dislocation is sufficient to overcome the barrier to pass through the obstacle.

In the DTM-DD, obstacles are modeled as points and are randomly generated at a prescribed density ρ_{obs} on dislocation slip planes. Obstacles are characterized by critical strength τ_{obs}. The pileup mechanism continues until the stress on the leading dislocation is sufficient to overcome τ_{obs}. The dislocation then passes through the obstacle over a time period of t_{pile}.

Dislocation position within a pile-up is highly unstable and introduces significant oscillatory behaviour to dislocation velocity [105]. Following Agnihotri & Van der Giessen [104], the shear wave speed $C_t = \sqrt{\mu/\rho}$ (where μ is the shear modulus and ρ is the density of the material) was utilized as a cut-off for dislocation velocity to moderate this artefact.

4.5 Computational Algorithm

The fully dynamic coupled thermo-mechanical problem is solved with the following computational algorithm.

BEGIN:

compute $\mathbf{M}^{uu}$, $\mathbf{C}^{uu}$, $\mathbf{C}^{\Theta\Theta}$, $\mathbf{K}^{uu}$, $\mathbf{K}^{u\Theta}$, $\mathbf{K}^{\Theta\Theta}$ using (3.21) to (3.26)

enforce initial thermal and mechanical conditions from (3.4) to (3.7).

for each time step n to $nsteps$, DO:

Compute $\mathbf{F}^{u,ext}$ and $\mathbf{F}^{\alpha}$ using (3.27), (3.30)

compute $\mathbf{F}^{\Theta,ext}$ and $\mathbf{F}^{TM}$ using (3.28), (3.29)

solve $\ddot{\mathbf{u}}$, $\dot{\mathbf{u}}$, $\mathbf{u}$, $\dot{\boldsymbol{\Theta}}$, $\boldsymbol{\Theta}$

solve dislocation mechanisms

compute the Peach-Koehler Force using (4.11)

update B^{α} using $\boldsymbol{\Theta}$

compute s^{α} given the Peach-Koehler Force and B^{α}

solve $\dot{\mathbf{v}}^{\alpha}$, $\mathbf{v}^{\alpha}$, $\mathbf{d}^{\alpha}$

apply dislocation interaction rules (nucleation, annihilation, pile-up)

end for

END

Chapter 5

Simulations and Discussion

In the following chapter, the effect of inertia, temperature, and strain-rate on the two-dimensional high strain-rate simulation of single crystal specimens are investigated. First, the DTM-DD is used to study wave effects resulting from an elastodynamic description of a specimen's mechanical behaviour. Next, the implications of a dynamic description of dislocation motion is studied. Then, in the context of extension load testing, the sensitivity of temperature- and strain-rate dependence of dislocation parameters is explored. Finally, the DTM-DD is extended to investigate loading rate effects through the simulation of the nano-indentation of a thin film sample.

For the simulations presented in this section, all specimens are assumed to be isotropic single fcc crystals of a copper-like substance, with material properties listed in Table 5.1. Accordingly, simulations are in the $\{111\}$ plane; and dislocation slip planes are oriented with inclinations $\alpha = (-60°, 0, 60°)$ from the horizontal. Specimens are assumed to be initially stress-free and void of dislocations.

Table 5.1: Material parameters for copper-like substance

Property	**Symbol**	**Units**	**Value**
Elastic modulus	E	GPa	117
Poisson's ratio	ν	-	0.36
Density	ρ	kg/m^3	8960
Specific heat capacity	C_p	$J(kgK)^{-1}$	385
Coefficient of linear thermal expansion	α	K^{-1}	$17(10^{-6})$
Thermal conductivity	k	$W(mK)^{-1}$	385

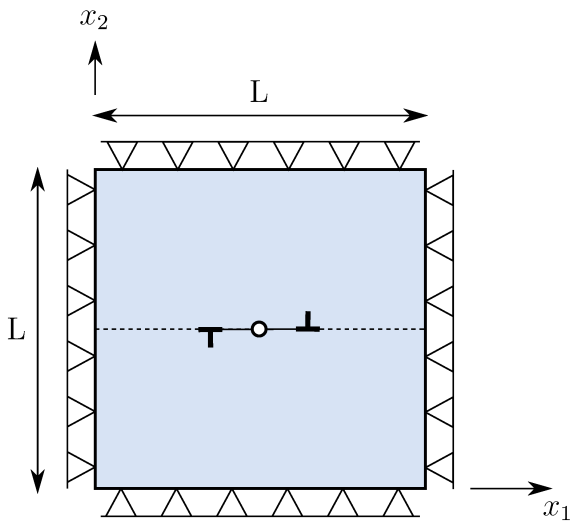

Figure 5.1: Schematic of square specimen under thermal load containing one inclined slip plane with one Frank-Read source.

5.1 Wave Propagation from Dislocation Nucleation

First, the capacity of a dynamic implementation to capture wave effects is illustrated through a simple example of dislocation nucleation. Consider a two-dimensional square specimen with sides of length $L = 1\ \mu m$ initially at $T_0 = 0K$. The specimen is pinned on all edges and, for simplicity, contains one slip plane parallel to the x_1 axis. The slip plane passes through the center of the specimen where a single Frank-Read source with Burgers vector of magnitude of $b = 0.25\ nm$ is located (Fig. 5.1). The domain is discretized into a regular mesh of 151 by 151, 4-node bilinear quadrilateral elements.

A temperature change of $\Theta = 500K$ is imposed over the entire domain. Thermal strains are induced due to the displacement limitations at the boundaries. The specimen is assumed to possess no material damping. Dislocation drag B and critical nucleation strength τ_{nuc}^{FR} were both assumed to be temperature independent, i.e. $B = B_0$ and $\tau_{nuc}^{FR} = \tau_0^{FR} = 50\ MPa$. A shear-only stress state is generated by allowing non-physical thermal shear strain. This is accomplished by prescribing the coefficient of thermal expansion α in the x_1- and x_2-drections as zero; and in the shear x_{12}-direction, $\alpha_{12} \neq 0$. As the slip plane is oriented parallel to the x_1-axis, the resolved shear state acting on the Frank-Read source is equivalent to the shear state of the domain. A dislocation dipole is instantaneously nucleated, i.e. $t_{nuc} = 0$, at a prescribed distance of $L_{nuc} = 0.2L$ once the resolved shear

stress acting on the Frank-Read source reaches τ_{nuc}^{FR}. For this example, nucleation was restricted to occur only once to isolate the effects of a single nucleation event, and the nucleated dipole was assumed to be permanently pinned.

Subsequent to nucleation, nodal enrichments are introduced to the elements intersecting the newly activated slip plane. Displacement and velocity, as well as stress concentrations, are initially localized at enriched nodes (Fig. 5.2). Elastic fields propagate radially outwards from the nucleation position outwards towards the domain boundary, and are then reflected inwards once reaching specimen boundaries (Fig. 5.3 & 5.4). Interference of wave patterns occur between the waves of neighbouring dislocations, as well as between the primary emitted waves and secondary reflected waves. Interference is substantially compounded due to the small size of the domain. The propagation speed of an elastic wave is $3.6 \cdot 10^3\ m/s$ based on a first-order estimation, $C = \sqrt{E/\rho}$. As such, the time required for a wave to traverse the domain in this example is on the order of of $10^{-1}\ ns$. However, for simulations presented in the latter sections of this chapter, simulation time is on the order of $10^3\ ns$. In this way, elastic waves have ample time to repeatedly reflect from one boundary edge to another such that original wave patterns are smeared into indistinguishable "noise" (Fig. 5.3c, 5.4c).

Additionally, the propagation speed of an elastic wave exceeds the average velocity of a moving dislocation. In this way, an unpinned dislocation traversing the domain may feel the effect of the reflection of waves generated at its nucleation. For the subsequent examples in this chapter, the ensuing wave interactions from recurring nucleation events generating an evolving distribution of dipoles, as well as the nonuniform movement of dislocations, further adds to the complexity of interference patterns. Consequently, the length of simulation time, dislocation density, and dislocation movement if any, contribute to the highly oscillatory nature of simulation results.

Non-physical oscillations is observed both preceding and following the wave front which arise due to Gibb's phenomenon in Fig. 5.3 and 5.4. For high-frequency transient waves, the presence of these spurious oscillations cannot be effectively removed through mesh refinement [106]. The simulation of dynamic wave propagation using XFEM, particularly in discontinuous domains, often requires artificial damping or stress smoothing to provide smooth, meaningful results. Numerical methods, for example the Phantom Node-Generalized FEM by [106] address the suppression of spurious oscillations without the use of artificial numerical damping or other post-processing. Here, for simplicity, nominal artificial damping of 6% critical was provided to dissipate the non-physical wave behaviour. The damped solution (Fig. 5.5) converges to the steady state solution as $t \to \infty$ [5].

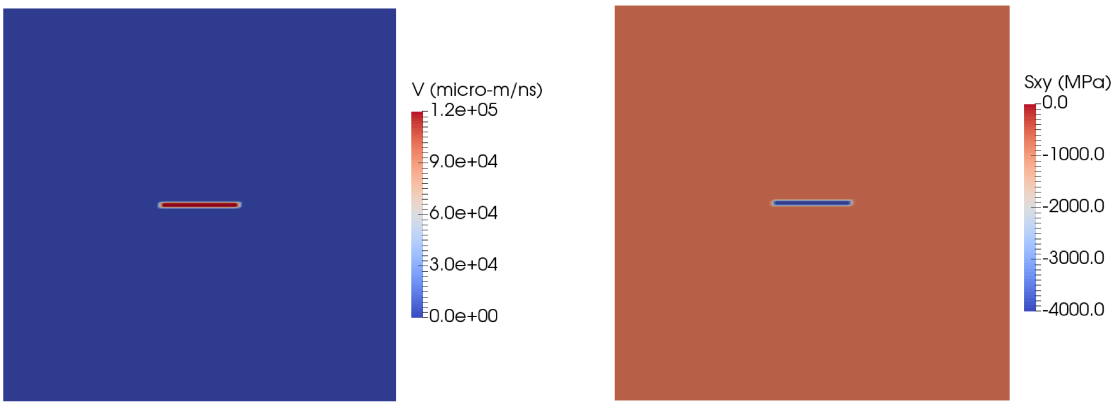

(a) (b)

Figure 5.2: Localization of (a) velocity (magnitude) and (b) shear stress (σ_{xy}) immediately after nucleation correspond to enriched elements.

5.2 Dynamic Dislocation Motion

In this section, the dynamic effects on dislocation motion is studied. Suppose that the nucleated dipole in the simulation setup described previously in Sec. 5.1 is instead assumed to be free to move along its slip plane which is parallel to the x_1-axis. A Peach-Koehler force of $|F^{PK}|= 1\ N/m$ is artificially imposed on the dislocations to study, under an idealized load, their behaviour as they reach steady-state velocity. The characterization of dislocation motion using a viscous drag-controlled phenomenological equation of motion is discussed in detail in Section 4.1.1. In a dynamic implementation, the effective mass of each dislocation α is calculated as a function of its velocity based on (4.14).

The displacement, velocity, and acceleration profiles of the right-hand-side dislocation are presented in Fig. 5.6 for simulation time step sizes of $\Delta t = 10^{-3}$, 10^{-4}, and $10^{-5}\ ns$. Time $t = 0\ ns$ corresponds to the dislocation initially at rest just after it has been nucleated. Dislocations were observed to approach steady state velocity – which is limited by the transverse wave speed $C_t = \sqrt{\mu/\rho} = 2.191\ \mu m/ns$ – in a logarithmic fashion. The velocity rise time corresponds to the exponential decay of acceleration.

As is intuitively expected, the solution converges as the simulation time step size is reduced from $\Delta t = 10^{-3}$ to $10^{-5}\ ns$. The profiles at $\Delta t = 10^{-4}$ to $10^{-5}\ ns$ are nearly indistinguishable. A time step size $\Delta t \leq 10^{-4}\ ns$ is presumably required for a converged and

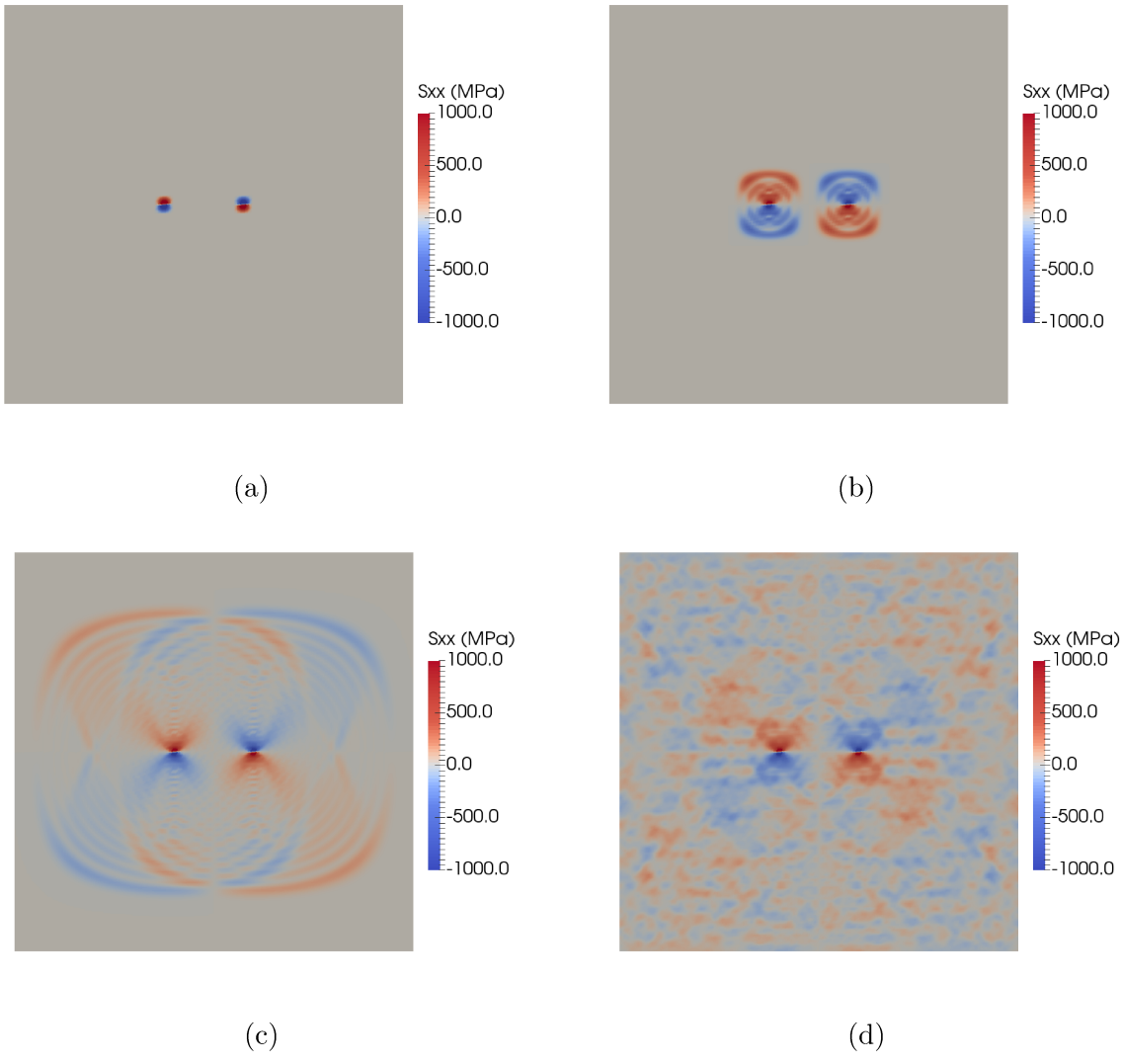

Figure 5.3: Evolution of stress (σ_{xx}) field subsequent to a nucleation event at (a) $t = 0.0368\ ns$; (b) $t = 0.0589\ ns$; (c) $t = 0.1475\ ns$; and (d) $t = 1.8400\ ns$.

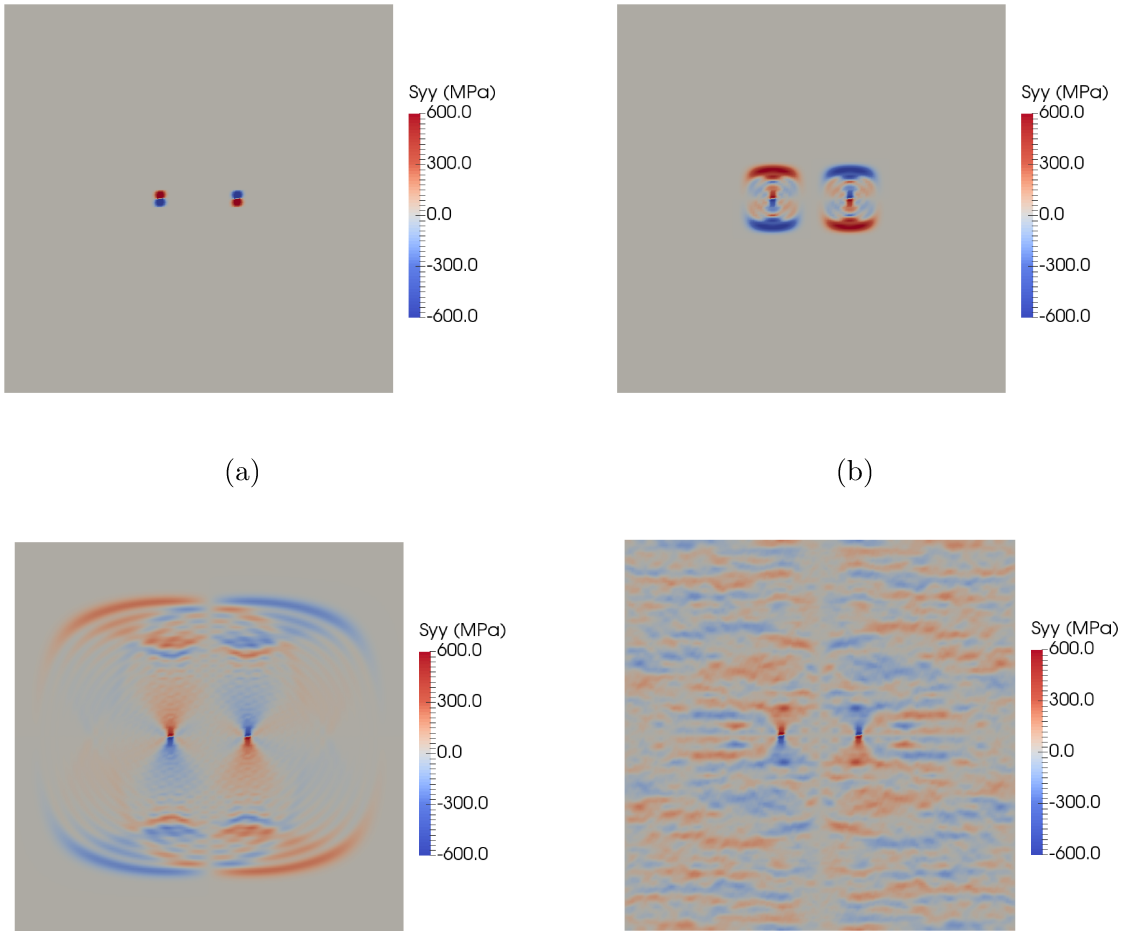

Figure 5.4: Evolution of stress (σ_{yy}) field subsequent to a nucleation event at (a) $t = 0.0368\ ns$; (b) $t = 0.0589\ ns$; (c) $t = 0.1475\ ns$; and (d) $t = 1.8400\ ns$.

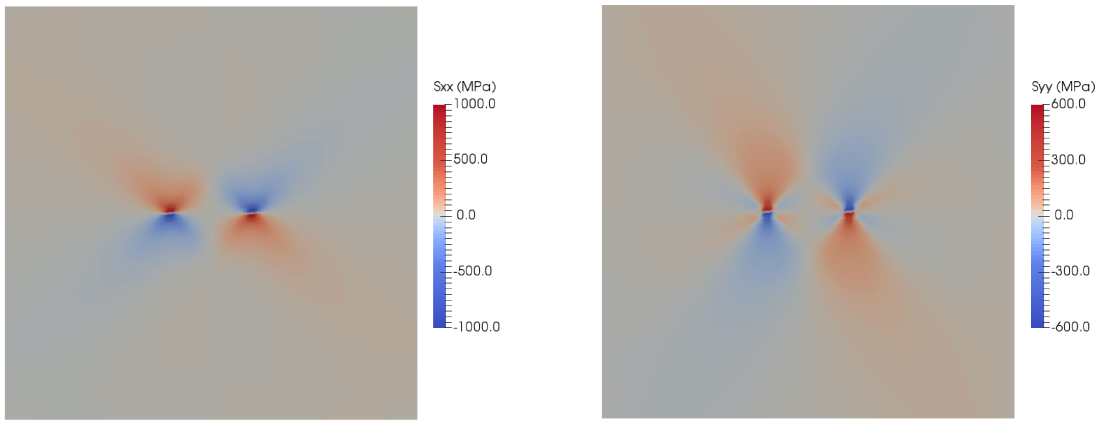

(a) σ_{xx} (b) σ_{yy}

Figure 5.5: Steady state solution of the damped system at $t = 1.8400\ ns$

accurate depiction of dislocation motion. This result is comparable to that by [61] in their investigation of dynamic dislocation motion. In comparison, the time step size required for the stability of the simulations presented in the latter examples is in the order of $10^{-3}\ ns$.

In a quasi-static implementation, velocity is linearly related to the Peach-Koehler force, i.e. $\mathbf{v} = \mathbf{B}^{-1}\mathbf{F}$. There is no rise time; rather, instantaneous velocity change is applied over one time step. In this way, overall dislocation response is artificially hastened in a quasi-static implementation versus a dynamic one. At $\Delta t = 10^{-3}\ ns$, approximately 80% of the velocity rise time is reached within the first time step. In this way, the dynamic effects in simulations with larger time step sizes are effectively limited to just a few time steps following nucleation. A dynamic implementation using larger time steps cannot capture the incremental changes in velocity rise. Consider a conservative estimate of velocity rise time in the order of $10^{-2}\ ns$. Assume a 1 μm specimen is subjected to extension loading to a meaningful strain, for example, conventional engineering yield at $\varepsilon = 0.2\%$. The fraction of rise time to simulation time is presented in Table 5.2. The rise time represents an increasingly large fraction of the total simulation time as strain-rate is increased. As such, it is qualitatively expected that the effect of dislocation mass increases in significance as strain-rate is increased, as in the results by [61].

The relationship between dislocation motion and strain-rate is complex. The criticality of dynamic effects of dislocation motion is dependent on the influence of existing dislocation and obstacle structure, material behaviour of the medium, as well as the strain-rate depen-

Table 5.2: Constant velocity rise time versus total simulation time.

Strain rate	**Simulation time**	**Rise time/Simulation time**
	ns	%
10^3	2000	0.0005
10^4	200	0.005
10^5	20	0.05

dency of these factors. In Wang et al. [61], stress-strain behaviour is observed to be harder for dynamic motion than for the quasi-static approximation in tensile test simulations. The delay in response captured by a dynamic implementation theoretically increases the amount of time required for dislocations to traverse the domain. The overall decreased rate of dislocation slip using dynamic dislocation motion may explain the overall harder material response. The increased length of their presence within the domain impedes sources from nucleating which the reduces the dislocation density of the dynamic implementation versus the quasi-static one. Additionally, the corresponding dislocation density was observed to be lower for dynamic motion than for quasi-static motion. As well, the impact of dynamic terms in dislocation motion was qualitatively observed to increase with increasing strain-rate for material response.

A quasi-static implementation of dislocation motion, on one hand, neglects velocity rise time and suffers from reduced simulation accuracy; but on the other, allows for the use of larger time steps. In comparison, a dynamic implementation captures the rise time which improves the accuracy of simulated material reponse. However, the cost associated is the reduction of the time step size for convergence of the dislocation motion. Thus, the challenge here lies in finding a balance between simulation accuracy and computational tractability.

5.3 High Strain-Rate Tensile Extension

In this section, dislocation parameters are investigated in the context of tensile extension. Consider a rectangular single crystal specimen with edge dimensions $L = 1.5\ \mu m$ and $W = 0.5\ \mu m$ (Fig. 5.7). Rollers along the $x_1 = 0$ boundary, as well as a pin at $(x_1, x_2) = (0, 0)$ are provided to prevent rigid body motion. The specimen is loaded uniaxially in the tensile direction (x_1) following similar studies by [6,94,102]. The domain is discretized into a regular mesh of 60 by 20 ($L \times W$), 4-node bilinear quadrilateral elements.

Plasticity assumed to be confined within the middle two-thirds of the specimen to prevent

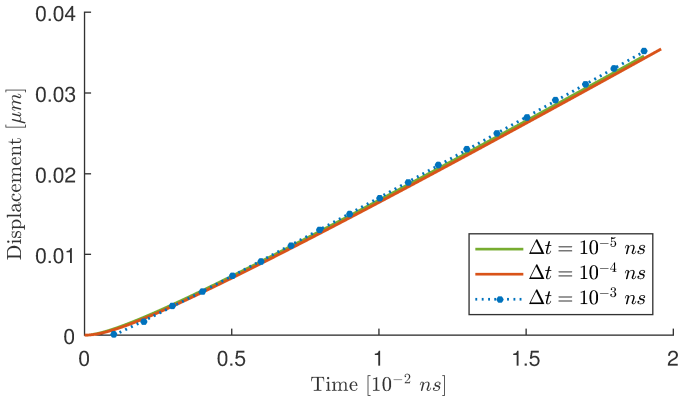

(a)

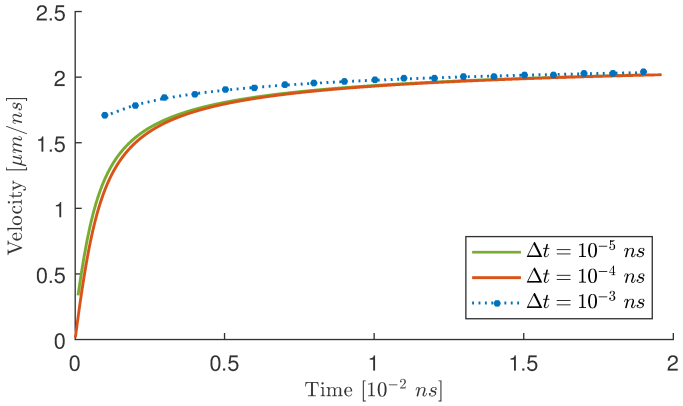

(b)

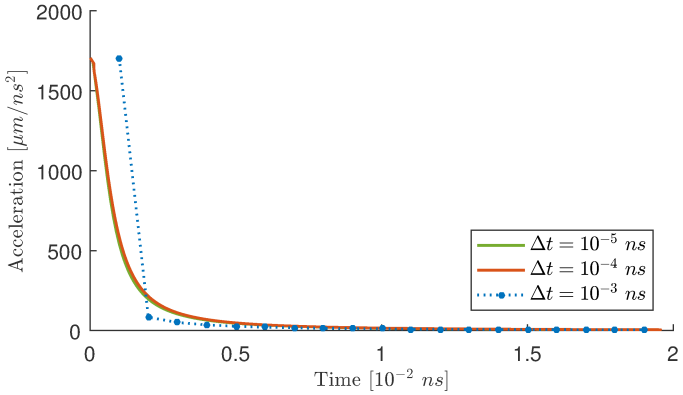

(c)

Figure 5.6: Profile of dislocation with respect to initial dislocation position at time $t = 0\ ns$ (a) Displacement; (b) Velocity; and (c) Acceleration.

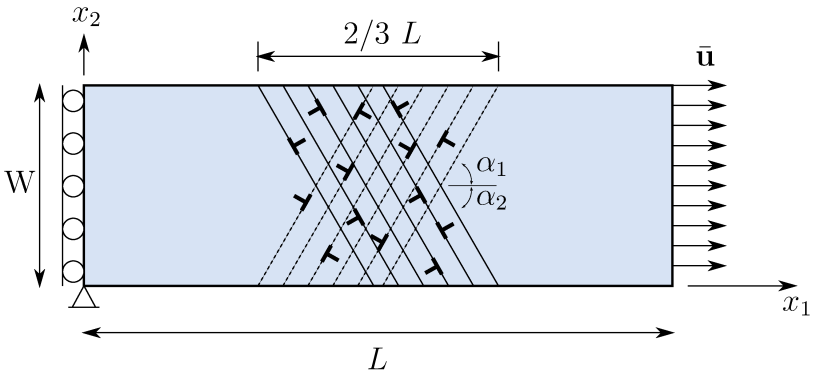

Figure 5.7: Schematic of rectangular specimen under uniaxial extension loading.

the interaction of dislocation mechanisms with support conditions [102]. For this reason, the fcc crystal structure is further simplified to only two potentially active slip systems inclined at $||\alpha_1||= ||\alpha_2||= 60°$ from the horizontal x_1 axis. The third system oriented at $0°$ from the horizontal is not simulated as slip planes would intersect the supports at the left boundary. Each slip system contains parallel slip planes spaced at $100b$ apart, where $b = 0.25\ nm$ is the magnitude of the Burgers vector [27].

The crystal is assumed to contain an initial distribution of dislocation sources and obstacles randomly generated based on specified density of $\rho_{src} = 30\ \mu m^{-2}$ and $\rho_{obs} = 30\ \mu m^{-2}$, respectively, for each slip system. Dislocation sources are assumed to be of the Frank-Read type with Burgers vector of magnitude of $b = 0.25\ nm$. Sources are randomly assigned a base nucleation strength (τ_0^{FR}) from a Gaussian distribution with an average and standard deviation of $\bar{\tau}_{nuc} = 50\ MPa$ and $\bar{\sigma}_{nuc} = 1\ MPa$, respectively [6, 27, 94, 102]. A uniform nucleation time of $t_{nuc} = 15\ ns$ and pile-up time $t_{pile} = 15\ ns$ was assumed for all sources and obstacles, respectively. Critical annihilation distance was assumed to be $L_e = 6b$ [27]. Dislocation mechanisms are assumed to be self-contained within each slip system, i.e., nucleation, annihilation, as well as the interactions between dislocations and obstacles are assumed to be restricted within each slip system. Unless noted otherwise, nominal material damping of 4% crticial was provided to dissipate the spurious oscillations related to Gibb's phenomenon as discussed in Sec. 5.1. Plastic work done by dislocation motion was assumed to be fully converted to heat, i.e. $\beta = 1.0$.

In the following examples, aspects of thermal dependence and strain-rate sensitivity is studied in isolation. To reduce the number of mechanisms at work, it was assumed that (1) dislocation parameters are temperature independent unless otherwise noted, i.e. $B = B_0 = 1 \cdot 10^{-4}\ Pa \cdot s$ and $\tau_{nuc}^{FR} = \tau_0^{FR}$; and (2) dislocation motion is quasi-static. A dynamic

description of dislocation motion is converged at a time step size of $\Delta t = 10^{-12}\ s$ at $\dot{\varepsilon} = 10^4\ s^{-1}$ (Fig. 5.8). This corresponds to the convergence results by [61] in their study of dislocation motion. As such, a time step size of $\Delta t = 10^{-12}\ s$ was sufficient to resolve the quasi-static motion assumed in this example.

5.3.1 Role of Boundary Conditions on Thermal Effects

Temperature effects are captured by the thermo-coupled formulation of the DTM-DD and its character is determined by the choice of thermal boundary conditions. In this example, the influence of the choice of thermal boundary conditions on material response was investigated.

The thermal boundary condition can be defined by temperature or by flux. For simplicity, mixed conditions were not considered. Three types of thermal conditions were investigated:

1. The heat generated by dislocation motion was assumed to be fully dissipated at the surface of specimen such that the specimen maintains its initial reference temperature at the surface. Accordingly, a constant temperature condition is enforced at the boundaries throughout the simulation time, i.e. $T = T_0$ on $\Gamma = \Gamma_T$.

2. The heat generated by dislocation motion was assumed to be fully retained within an ideally insulated specimen. A zero flux condition (which is refered to as *adiabatic*) is enforced, i.e. $q = 0$ on Γ_h.

3. The heat generated by dislocation motion is dissipated at the surface of the specimen via convection. A non-zero flux condition dependent on the temperature differential between the specimen and the ambient temperature is enforced, i.e. $q = h(\Theta - \Theta_\infty)$ where h is the convection or heat transfer coefficient, Θ is the temperature of the specimen at the boundary, and Θ_∞ is the ambient temperature.

In reality, the thermal boundaries are at some intermediate stage between fully dissipative and fully insulated, i.e. $T \neq T_0$ and $q \neq 0$, and may be mixed.

Extension loading was applied at a constant strain-rate of $\dot{\varepsilon} = 10^4\ s^{-1}$ at an initial temperature of $T_0 = 300K$. Thermo-coupled and fully dynamic material response was obtained using the three boundary conditions is compared in Fig. 5.9. For reference, the uncoupled (purely mechanical) dynamic and quasi-static response is also provided. The behaviour of the material response is highly dependent on the chosen thermal boundary condition. In the adiabatic case, the heat generated is completely retained and cumulative; and so, the

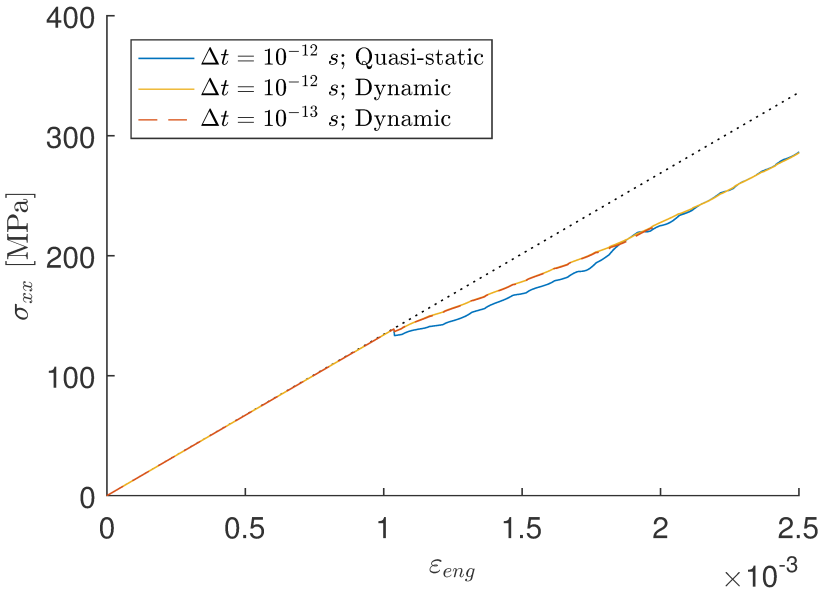

(a)

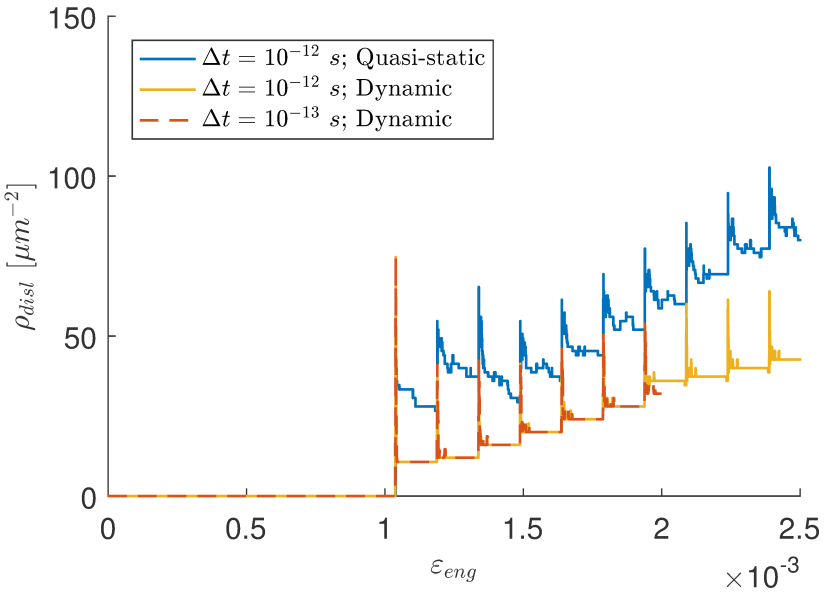

(b)

Figure 5.8: Extension loading test response at $\dot{\varepsilon} = 10^4\ s^{-1}$ with dynamic dislocation motion: (a) Stress-strain response, and (b) Dislocation density.

average temperature in the domain constantly rises over the duration of the simulation. This is reflected in the saturation of the temperature field in the domain as compared to the constant temperature case (Fig. 5.10). The asymmetry in the temperature field is attributed to the asymmetric distribution of sources, obstacles, and dislocations, as well as the asymmetry in the resulting interfering elastic waves. Unconstrained temperature increase – which promotes dislocation activity in a positive feedback mechanism – is translated in to significant thermal expansion of the specimen. As such, the simulated material response using the zero flux condition enters into an unphysical state of compression: thermal expansion, which causes compression at the supports, dominates over the tensile force of the extension load (Fig. 5.9a). The average domain temperature as σ_{xx} enters the compressive regime for the zero flux condition approaches $\Theta_q = 410K$; whereas for the constant temperature condition as the same strain, $\Theta_T = 302K$.

The material response using a convection boundary condition is similar to that of the adiabatic condition. The heating in the domain is from dislocation motion; and heat is highly localized to the location of individual dislocations. First, heat must be conducted through the specimen. Then, heat is dissipated only at the boundaries and the rate of dissipation is restricted to the temperature differential between the temperature of the specimen at the boundary and the ambient temperature of the environment. Due to the asymmetry of the temperature field, heat dissipation is also not constant along the entire boundary.

It is necessary to include thermal considerations as it impacts material response. However, as is clearly evident in this study, it is crucial to choose appropriate thermal boundary conditions as improper selection may lead to unphysical results. In the remainder of this chapter, a constant temperature condition is utilized to be conservative regarding thermal effects.

5.3.2 Role of Inertia on Material Response

In this section, the role of inertial effects on material response is investigated in the framework of the extension test setup. Extension loading was applied at constant strain-rates $\dot{\varepsilon} = 5 \cdot 10^3$, 10^4, and 10^5 s^{-1}. Note that due to limits in computational time, simulated strain is reduced with strain-rate. An initial temperature of $T_0 = 300K$ was assumed for the specimen. Thermo-coupled quasi-static and fully elastodynamic stress-strain behaviour and dislocation density were obtained at each strain-rate in Figs. 5.11, 5.12, and 5.13.

Frank-Read sources initially nucleate over a range of nucleation strength τ_{nuc} described by a Gaussian distribution. Due to a constant t_{nuc}, subsequent nucleation occurs in periodic

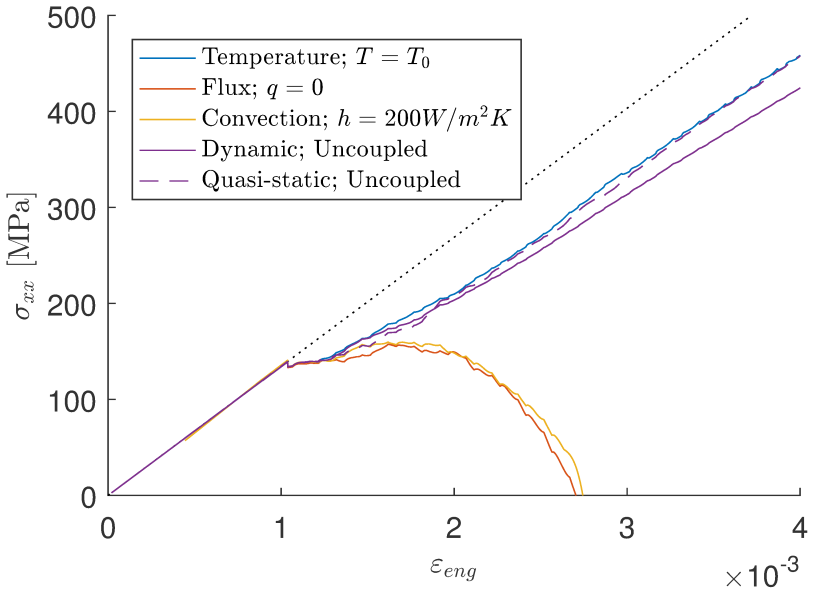

(a)

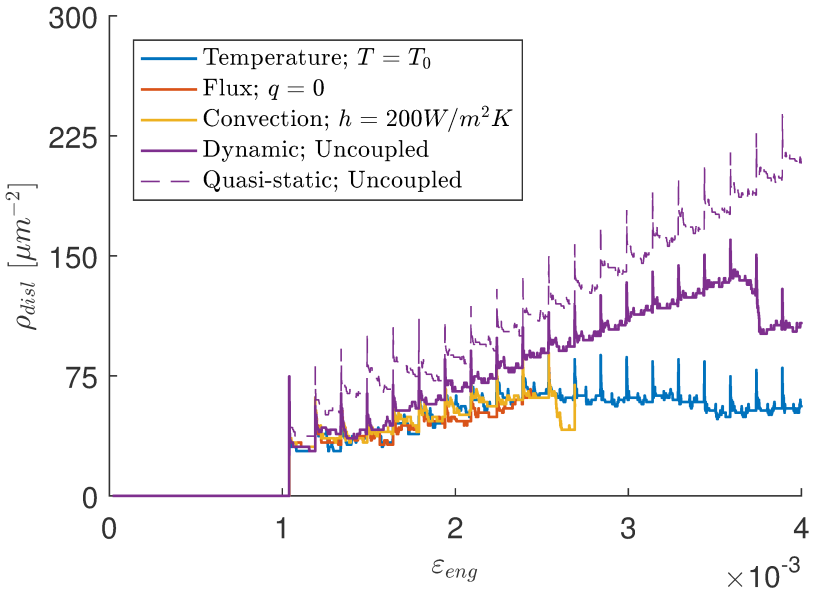

(b)

Figure 5.9: Effect of thermal boundary condition at $\dot{\varepsilon} = 10^4\ s^{-1}$: (a) Stress-strain response, and (b) Dislocation density. Note: Flux and Convection curves are truncated at ε_{eng} where σ_{xx} enters into compression.

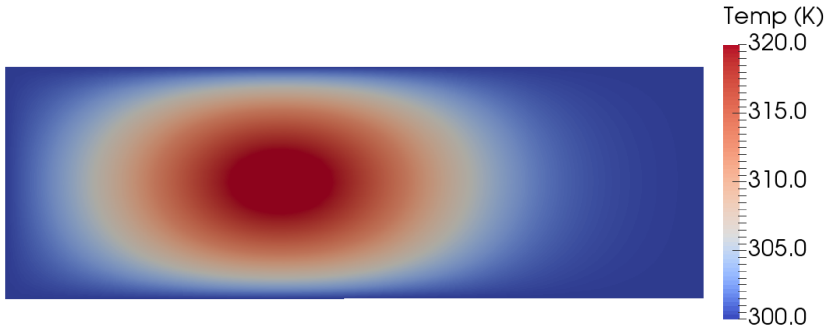

(a)

(b)

Figure 5.10: Temperature field at $\dot{\varepsilon} = 10^4\ s^{-1}$ for thermal boundary conditions governed by (a) Temperature, $T = T_0$ on Γ_t, at $t = 313\ ns$; and (b) Flux, $q = 0$ on Γ_h, at $t = 164\ ns$.

bursts [94,102]. Each nucleation "cycle" coincides with a sharp spike and subsequent decay in dislocation activity as reflected in the behaviour of dislocation density ρ_{disl}. Increased strain-rate reduces the number of cycles within a simulation, but serves to increase the period length of each cycle. Less dislocation activity is expected with increasing strain-rate due to the lower amount of active dislocations produced in fewer cycles. The rate at which ρ_{disl} increases with each cycle is indicative of competing rates of dislocation generation and removal [94]. Considering this rate balance, it is expected that the sensitivity of nucleation parameters decreases with increasing strain-rate. Increasing the strain-rate of loading has a similar effect as reducing specimen width, as in the size effect studies by Balint et al. [94].

An initial drop in the stress-strain curve indicates the first occurrence of nucleation. The standard deviation assigned to the base nucleation strength, i.e. $\tau_0^{FR} = \bar{\tau}_{nuc} \pm \bar{\sigma}_{nuc}$, reduces the intensity of the initial stress drop [102]. The onset of dislocation nucleation and subsequent activity signals the transition from elastic to plastic behaviour as, without dislocation effects, the material response simulated in the DTM-DD is based on linear-elastic constitutive laws. The stress-strain behaviour after the initial yielding is oscillatory even in the quasi-static case [94]. Due to a constant nucleation time t_{nuc}, plasticity mechanisms emerge at a higher strain (ε_{eng}) with increasing strain-rate. Increasing strain-rate also corresponds with increasing flow stress, as observed in the experimental trials of [70].

Periodicity is also reflected in stress fluctuations. Dislocation effects with increasing strain-rate are reduced due to lower dislocation activity (as reflected in the behaviour of ρ_{disl}) and become more isolated within each cycle due to increasing cycle length. As such, a significant change in the stress-strain behaviour is observed particularly as strain-rate is increased from $\dot{\varepsilon} = 10^4$ to 10^5 s^{-1}: material behaviour tends towards linear-elastic behaviour and periodicity in both the stress-strain response and dislocation behaviour is readily apparent. Also, the the sensitivity of mobility parameters is expected to decrease with increasing strain-rate due to decreasing dislocation activity.

At $\dot{\varepsilon} = 5 \cdot 10^3$ s^{-1}, the material response and dislocation behaviour of the dynamic and quasi-static cases are comparable. The dynamic solution is expected to converge to the quasi-static one as strain-rate is reduced. At $\dot{\varepsilon} = 10^5$ s^{-1}, dynamic and quasi-static material response is also comparable due limited dislocation activity. Thermal effects are most significant at $\dot{\varepsilon} = 10^4$ s^{-1}. A comparison between the maximum average temperature Θ_{max} attained in the dynamic and quasi-static simulation at each strain-rate is indicative of the degree of influence of thermal effects. The temperature reached in the dynamic case is consistently higher than the quasi-static case for all tested strain-rates. At $\dot{\varepsilon} = 5 \cdot 10^3$ and 10^5 s^{-1}, the domain experiences a maximum average temperature increase of 10% of T_0 or less for the quasi-static and dynamic cases. As well, the Θ_{max} between the two cases are comparable by a few degrees. In comparison at $\dot{\varepsilon} = 10^4$ s^{-1}, the domain experiences

a maximum average temperature increase of 44% and 48% of T_0 for the quasi-static and dynamic case, respectively.

The role of inertia significantly alters the character of the evolution of dislocation density. For all tested strain-rates, the dynamic dislocation density is consistently lower than the quasi-static case. The quasi-static ρ_{disl} curve exhibits a positive linear trend for both the coupled and uncoupled cases at the three tested strain-rates. In contrast, the dynamic ρ_{disl} curve is observed to flatten. This implies that dislocation generation and removal rates are in a state of quasi-equilibrium. As well, thermal effects appear to influence the behaviour of dislocation density: coupling of the quasi-static solution yields a softened response as observed in [6]. Here, we see a competition between thermal and inertial effects. The addition of dynamics reduces ρ_{disl} which is expected to harden material response, but also increase thermal effects which is expected for softening.

5.3.3 Temperature Dependence of Dislocation Drag

In this section, the temperature and strain-rate sensitivity of dislocation drag B is investigated. In the DTM-DD, heat is generated in the domain from dislocation motion, and temperature effects are captured by thermo-coupled formulation. Thermal effects influence dislocation mobility through a temperature-dependent description of drag, specifically through the temperature dependence of drag parameter B_1.

The extension loading test setup was repeated with the assumption of a linear relationship between drag and temperature as discussed in Sec. 4.1.4, i.e. $B^\alpha = B_0 + B_1\Theta$, where B^α is the drag, and Θ is the temperature at the location occupied by dislocation α. The specimen was loaded at a strain-rate of $\dot{\varepsilon} = 10^4\ s^{-1}$ at an initial temperature of $T_0 = 300K$. A value of $B_0 = 5 \cdot 10^{-5}\ Pa \cdot s$ was assumed, and B_1 was varied from $B_1 = 0$, $2 \cdot 10^{-7}$, and $7 \cdot 10^{-7}\ Pa \cdot s/K$. For clarity in the discussion, these temperature-dependent cases are referred to as *TD-0*, *TD-1*, and *TD-2*, respectively. Case *TD-1* and *TD-2* approximately correspond to the mean value of B_1 presented in Sec. 4.1.4, and two standard deviations from the mean, respectively. Stress-strain and dislocation density behaviour was obtained for strain-rates $\dot{\varepsilon} = 10^4$ and $10^5\ s^{-1}$ (Figs. 5.14 & 5.15). For comparison, results for the conventional temperature-independent definition $B = B_0 = 1 \cdot 10^{-4}\ Pa \cdot s$, referred to as Case *TI-0*, at $\dot{\varepsilon} = 10^4\ s^{-1}$ is included in Figure 5.14.

Temperature in the domain tends to increase due to the heat generated via dislocation motion. Given $B_1 \geq 0$, B increases with temperature. By the phenomenological equation of motion described by (4.1), it follows that dislocation velocity decreases with increasing drag and temperature. As thermal effects tend to increase through the course of a simulation

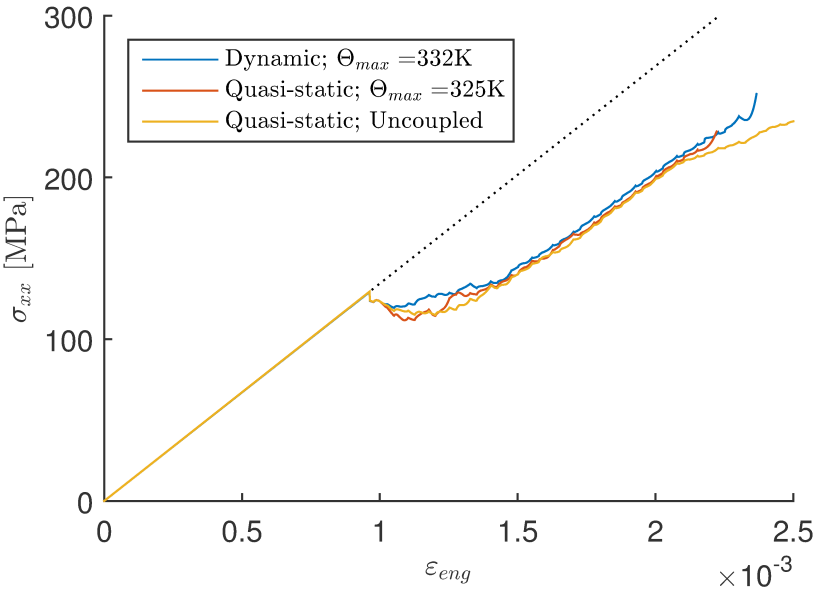

(a)

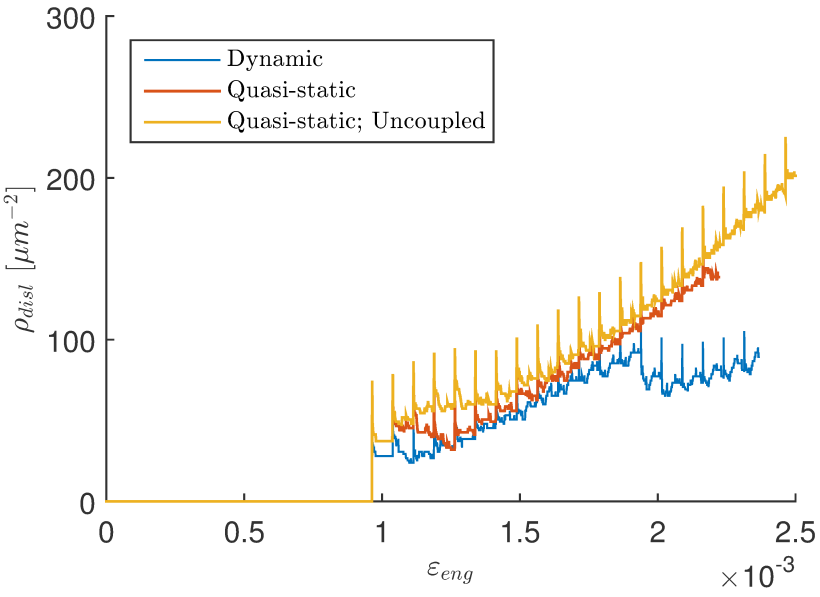

(b)

Figure 5.11: Extension loading test response at $\dot{\varepsilon} = 5 \cdot 10^3\ s^{-1}$: (a) Stress-strain response, and (b) Dislocation density.

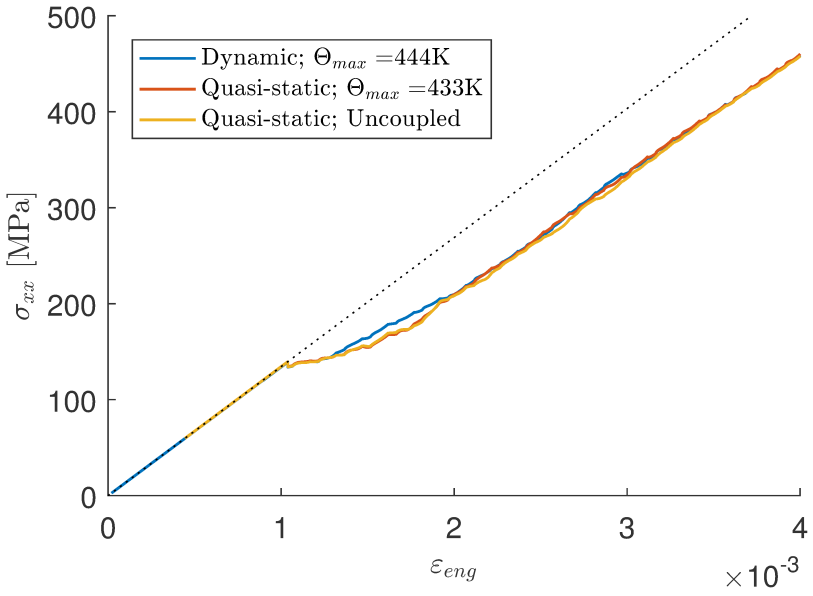

(a)

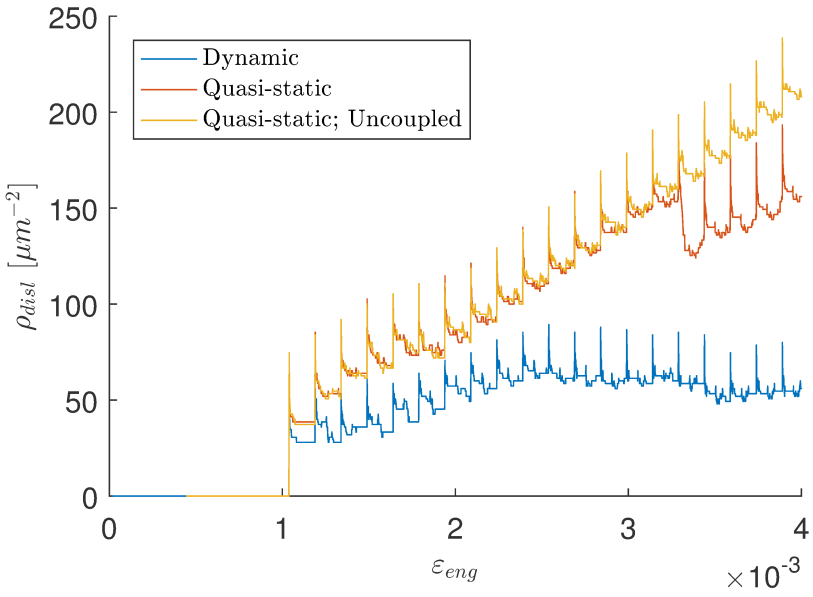

(b)

Figure 5.12: Extension loading test response at $\dot{\varepsilon} = 10^4\ s^{-1}$: (a) Stress-strain response, and (b) Dislocation density.

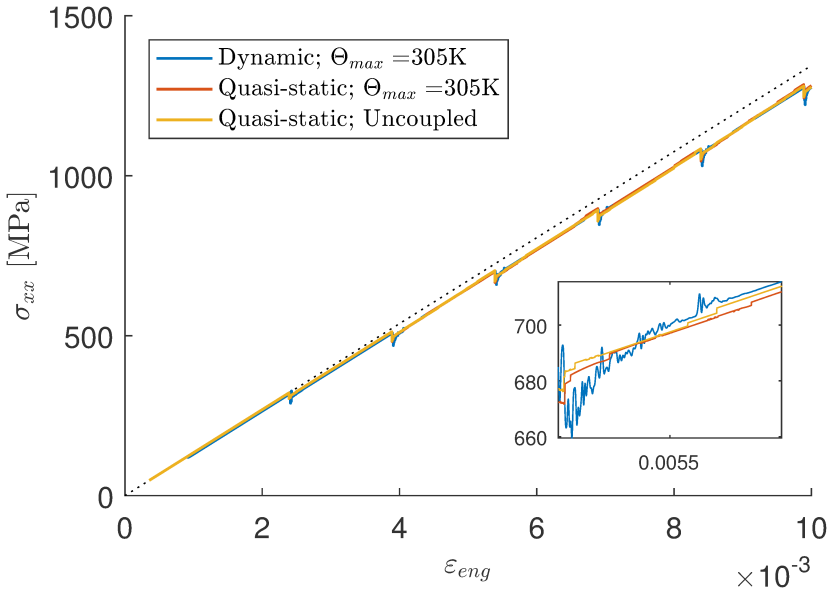

(a)

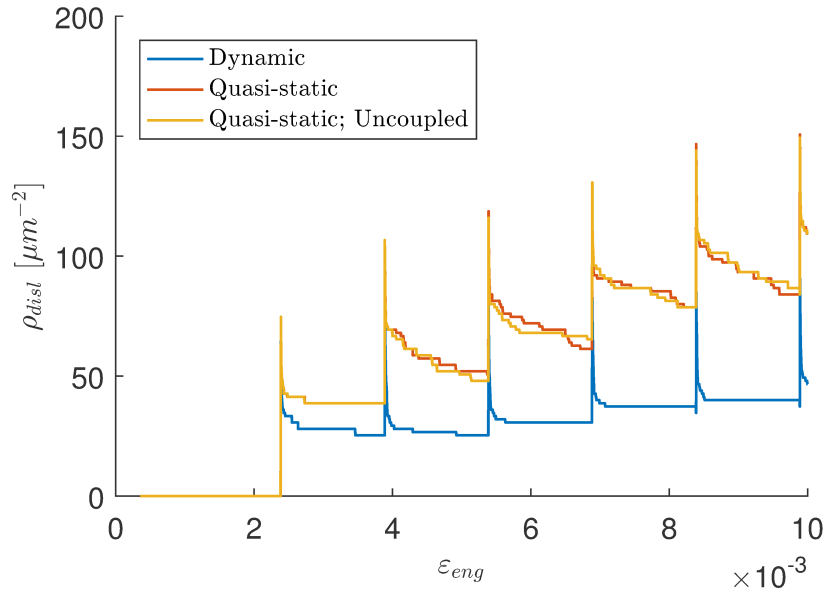

(b)

Figure 5.13: Extension loading test response at $\dot{\varepsilon} = 10^5\ s^{-1}$: (a) Stress-strain response, and (b) Dislocation density.

due to the accumulation of active dislocations, drag effects are expected to become more prominent at higher strains. Dislocations traversing the domain at a slower rate increases the back-stress on Frank-Read sources and reduces nucleation. As such, it is expected that increasing drag corresponds to lower dislocation density which, as discussed in Sec. 5.3.2, results in the increasing hardness of the material response. Case *TD-0* exhibits the softest response of the temperature-dependent cases; and *TD-2*, the hardest. A temperature increase of $\Delta\Theta = 70K$ at the location occupied by a dislocation is required for an equivalent B between the conventional temperature-independent definition in Case *TI-0* and the temperature-dependent Case *TD-2*. The first instance of this magnitude of temperature change occurs at $\varepsilon = 1.6{\cdot}10^{-3}$. As such, the stress-strain response of Case *TD-2* approaches Case *TD-0*.

As discussed in Sec. 5.3.2, less dislocation activity is expected with increasing strain-rate. Accordingly, the effect of B decreases with increasing strain-rate as its influence is only manifested through dislocation activity. The temperature rise in a specimen is a direct consequence of dislocation activity. Consequently, the role of B_1 increases in significance with decreasing strain-rate. The overall hardening due to drag-temperature dependence, and also the hardening between varying parameter B_1, becomes more apparent as strain-rate is reduced from $\dot{\varepsilon} = 10^5$ to 10^4 s^{-1}.

5.3.4 Temperature Dependence of Dislocation Nucleation

In this section, the temperature and strain-rate sensitivity of the critical nucleation strength of Frank-Read sources, τ_{nuc}^{FR}, is investigated. Thermal effects influence material response through the characterization of τ_{nuc}^{FR} as temperature dependent.

The extension loading test setup was repeated with a temperature-dependent implementation of nucleation strength, described by a third-order polynomial (4.22) as discussed in Sec. 4.3. Reference temperature was varied from $T_0 = 300$ to $700K$. Stress-strain and dislocation density behaviour were obtained for strain-rates $\dot{\varepsilon} = 10^4$ and 10^5 s^{-1} (Figs. 5.16 & 5.17).

Due to this particular characterization of nucleation strength, a non-linear reduction in τ_{nuc}^{FR} is expected with increasing temperature. At $T_0 = 300K$, the distribution of τ_{nuc}^{FR} is approximately 50 ± 1 MPa based on (4.22). This is comparable to the conventional temperature-independent description, i.e. $\tau_{nuc}^{FR} = \tau_0^{FR}$ described in Sec. 4.3 with a Gaussian distribution of average and standard deviation $\bar{\tau}_{nuc} = 50$ MPa and $\bar{\sigma}_{nuc} = 1$ MPa, respectively. In comparison, at $T_0 = 500K$ the average value of τ_{nuc}^{FR} shifts to approximately 36 MPa; and at $T_0 = 700K$, 19 MPa. The activation criteria of the Frank-Read sources is

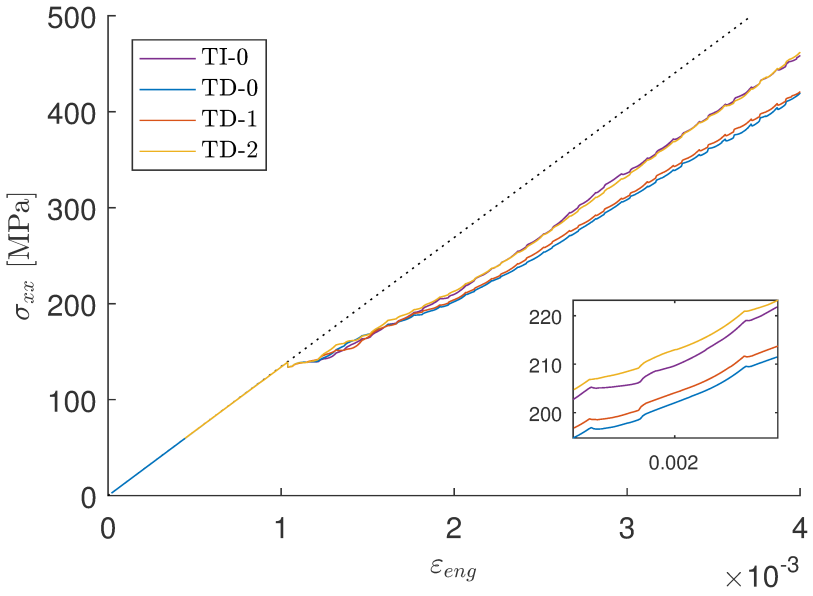

(a)

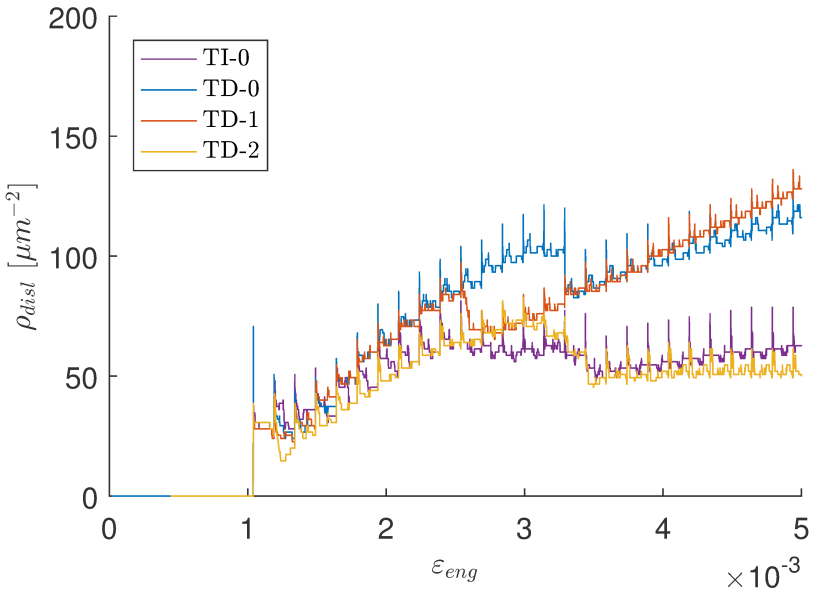

(b)

Figure 5.14: Temperature dependence of drag parameter B_1 at $\dot{\varepsilon} = 10^4\ s^{-1}$ under extension loading: (a) Stress-strain response, and (b) Dislocation density.

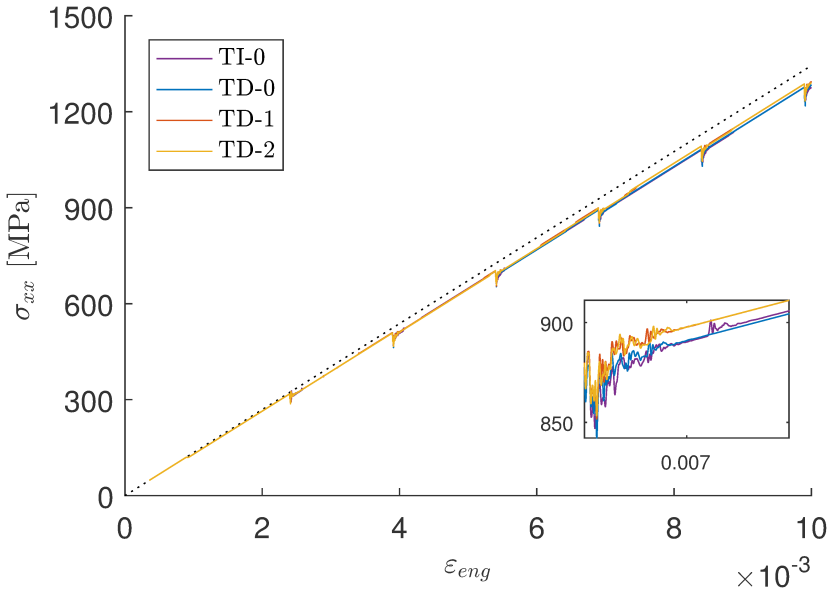

(a)

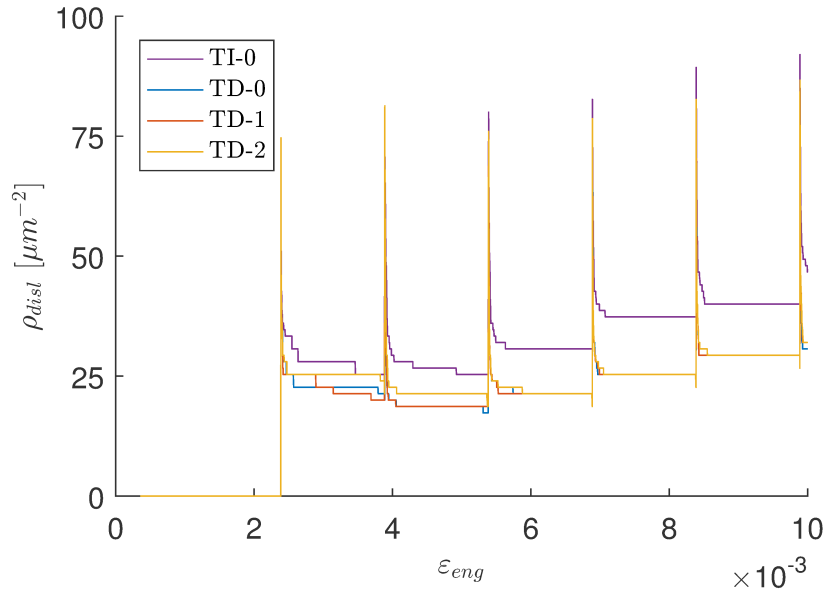

(b)

Figure 5.15: Temperature dependence of drag parameter B_1 at $\dot{\varepsilon} = 10^5\ s^{-1}$ under extension loading: (a) Stress-strain response, and (b) Dislocation density.

lowered: sources have more opportunity to be activated, dislocation nucleation then occurs earlier in the simulation, and ultimately, more dislocations are generated within the simulation time. This is expected to translate into plasticity and manifested in the softening of the material response. The implementation of the temperature dependence of τ_{nuc}^{FR} softens material response at both tested strain-rates. With increasing reference temperature T_0, dislocation effects begin earlier and the softening effect increases.

As discussed in Sec. 5.3.2, dislocation activity is expected to decrease with increasing strain-rate. This is reflected in dislocation density: harder curves correspond to lower ρ_{disl}. As dislocation activity directly translates to increased thermal effect, it is also expected that the influence of the thermal dependence of τ_{nuc}^{FR} increases with decreasing strain-rate. As such, the softening effect is observed to be more pronounced at $\dot{\varepsilon} = 10^4$ as compared to at 10^5 s^{-1}.

5.4 Nano-indentation of Thin Film

In the last two decades, the characterization of the material properties of thin films has been a focus of scientific and engineering inquiry due to the extensive development of MEMS and the trend towards miniaturization in commercial technology [103]. Experimental nano-indentation techniques are used extensively to study the material properties of bulk and thin-film materials where conventional testing methods are not feasible [107]. Loading is applied via an indenter and the penetration depth under the surface is measured. Load application in experimental testing is typically load-controlled and at a constant quasi-static rate. The elastic modulus, hardness of the material, or the "stiffness" of the contact, i.e. the rate of change of load versus penetration depth, is typically recovered from the procedure [108]. Common types of indenters include spherical, conical, Vickers, Berkovich etc., which influence the material response. The contact mechanics between the indenter and film vary based on the choice of indenter and indenter geometry. In experimental testing, indenters are fashioned from materials significantly more rigid than the film. The tip width or radius of a new indenter is typically in the range of $50 - 100$ nm [108].

The experimental studies of bulk iron-silicon [109], gold [110], and tungsten single crystals [111]; and polycrystalline copper [107] suggest the mechanism of indentation-induced deformation is described by dislocation nucleation and slip, initially localized at the indenter-film contact area [112]. In this example, the loading rate effects on the evolution of dislocation nucleation and slip is investigated in the framework of the nano-indentation of a thin-film specimen. The high-rate nano-indentation of a thin film is simulated in two-dimensions using the DTM-DD.

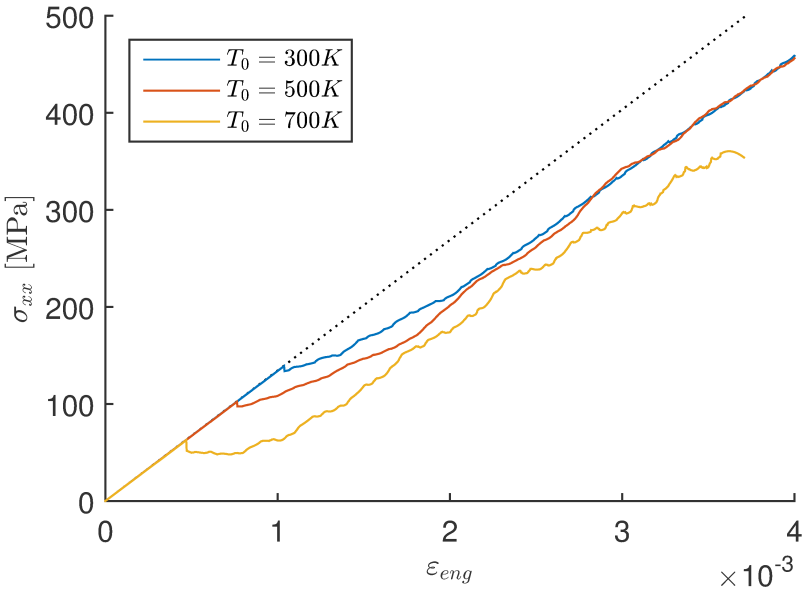

(a)

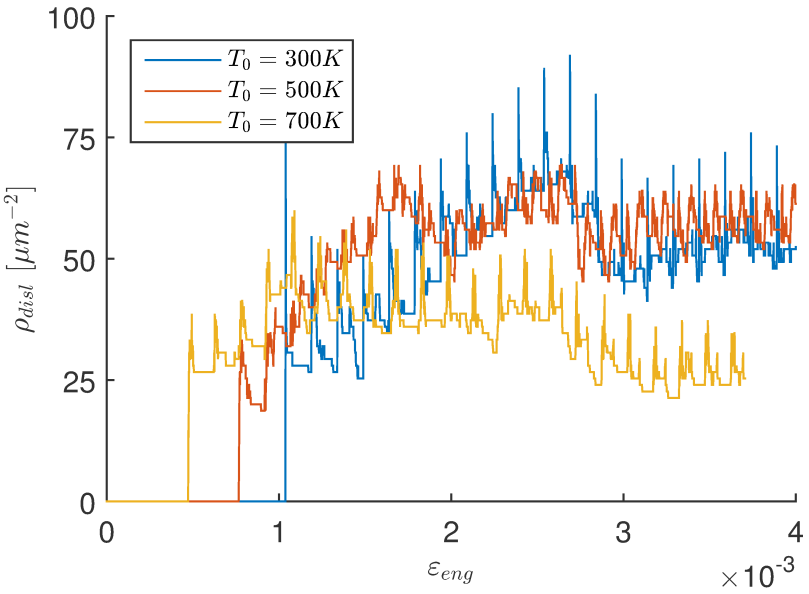

(b)

Figure 5.16: Temperature dependence of nucleation strength τ_{nuc}^{FR} at $\dot{\varepsilon} = 10^4\ s^{-1}$ under extension loading: (a) Stress-strain response, and (b) Dislocation density.

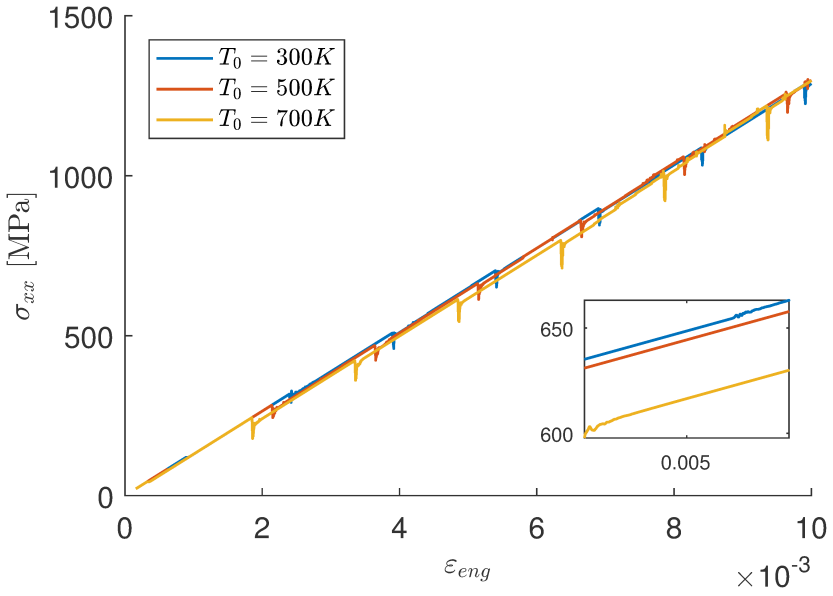

(a)

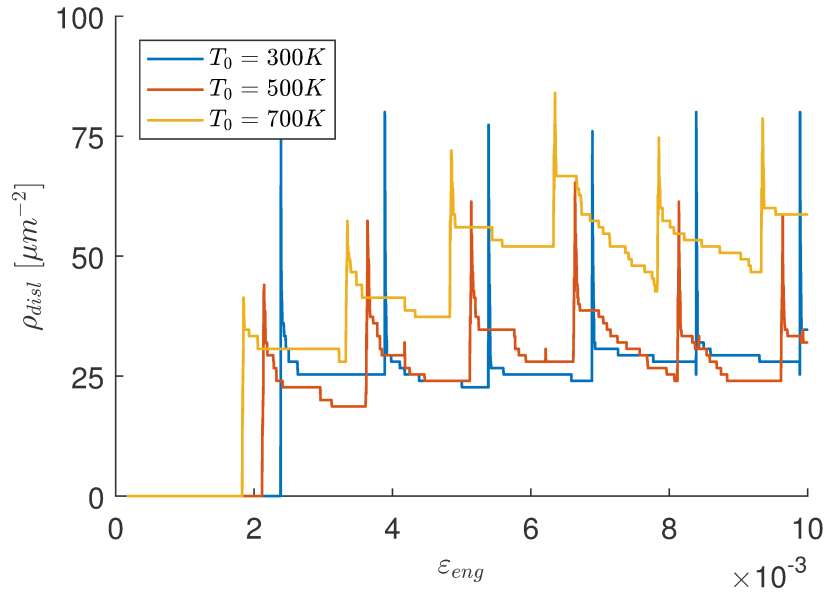

(b)

Figure 5.17: Temperature dependence of nucleation strength τ_{nuc}^{FR} at $\dot{\varepsilon} = 10^5\ s^{-1}$ under extension loading: (a) Stress-strain response, and (b) Dislocation density.

Let the contact between the indenter and film be considered as between a flat-ended, rigid planar punch and an elastic half-space (Fig. 5.18). The indenter and film are assumed to maintain full contact during the indentation process. The film is also assumed to be initially stress- and dislocation-free. Furthermore, the elastic contact is assumed to be non-Hertzian, with no extraneous surface forces, for example, friction or adhesion.

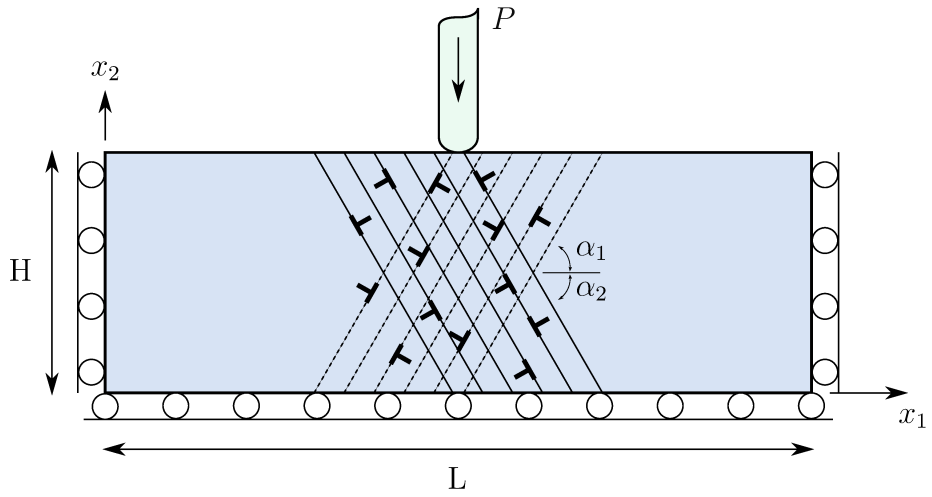

Figure 5.18: Schematic of nano-indentation test setup with the configuration of film and indenter

The thin film is limited to a finite rectangular cross-section of length $L = 1.5\ \mu m$ and depth $H = 0.6\ \mu m$. The indenter is flat-ended with width $2a$ and extending infinitely in the out-of-plane direction. A value of $2a = 50\ nm$ is assumed, keeping with a similar ratio between H and the radius of the circular indenter as in the experimental trials by [107]. The indenter is aligned at the centerline of the cross-section and displacement-controlled loading is applied to the top surface. Contact occurs directly under the width of the punch; theoretically, stress singularities occur at the shoulders of the punch [113]. The pressure distribution p generated by applied force P is:

$$p(x) = \frac{P}{\pi} \left\{ a^2 - x^2 \right\}^{-1/2} \tag{5.1}$$

where $0 \leq x \leq a$ (Fig. 5.19) [113]. The mean pressure over the contact width is

$$p_m = \frac{P}{2a} \tag{5.2}$$

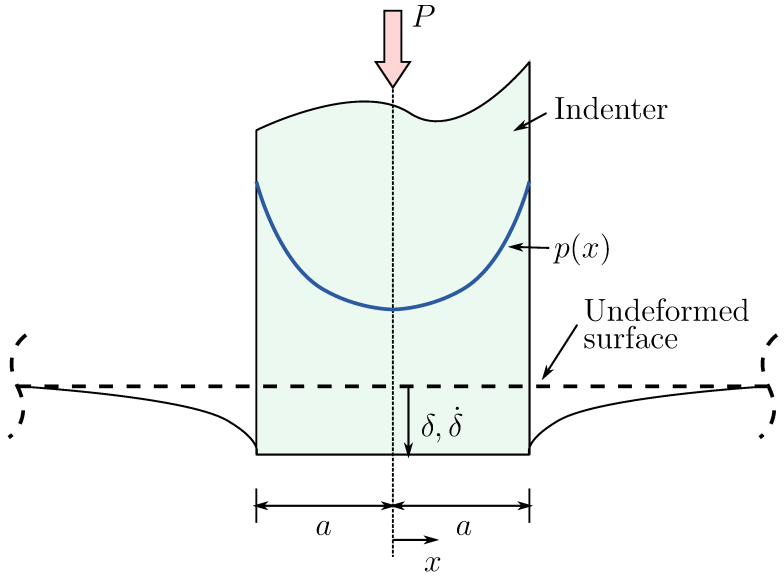

Figure 5.19: Schematic of the contact between indenter (flat-ended planar punch) and film (elastic half-space).

The film is assumed to be of a copper-like material with properties listed in Table 5.1. The indenter was chosen to have diamond-like material properties with $E_i = 1140\ GPa$ and $\nu_i = 0.07$ such that it is significantly more rigid than the film [107]. The domain is discretized into a regular mesh of 100 by 40 ($L \times H$), 4-node bilinear quadrilateral elements. Roller supports are provided on all boundaries except for the contact edge to prevent translation in the x_1 and x_2 directions for the vertical and horizontal edges, respectively. The simulation parameters from Sec. 5.3 are replicated in this study. Two slip systems inclined at $\alpha = \{60°, -60°\}$ are provided within the middle two thirds of the specimen. Dislocation parameters are assumed to be temperature dependent. Dislocation drag is characterized by parameters $B_0 = 5 \cdot 10^{-5}\ Pa \cdot s$ and $B_1 = 2 \cdot 10^{-7}\ Pa \cdot s/K$. Nucleation strength is defined as in (4.22). Dislocation motion was assumed to be fully dynamic.

Displacement-controlled loading was applied via the indenter at a rate of $\dot{\delta} = 5 \cdot 10^{-3}$, $1 \cdot 10^{-2}$, $5 \cdot 10^{-2}$, and $1 \cdot 10^{-1}\ m/s$. Loading was limited to a maximum displacement of 1% of the specimen depth H for small-strain deformation. Note that due to limits in computational time, simulated indentation depth is reduced with the rate of indentation. Nominal material damping of 4% critical was provided. A time step size of $\Delta t = 10^{-12}\ s$ was used to resolve dynamic dislocation motion. The indenter load versus indentation

depth $P - h$ and dislocation density behaviour ρ_{disl} is provided in Figs. 5.20 and 5.21. The elastic FEM solution is also provided for reference. The datum for indentation depth measurements was assumed to be the undeformed geometry of the top boundary ($x_2 = H$). Indentation depth d is normalized by the film thickness H as a measure of effective strain, i.e. $\varepsilon^* = ||\delta||/H$; and its rate of change, an effective strain-rate, $\dot{\varepsilon}^*$. As such, loading rates $\dot{\delta} = 5 \cdot 10^{-3}$, $1 \cdot 10^{-2}$, $5 \cdot 10^{-2}$, and $1 \cdot 10^{-1}$ m/s correspond to an average effective strain-rate of $\dot{\varepsilon}^* = 8.33 \cdot 10^3$, $1.67 \cdot 10^4$, $8.33 \cdot 10^4$, and $1.67 \cdot 10^5$ s^{-1}, respectively.

Loading rate dependent material behaviour similar to the strain-rate dependence exhibited in the extension test simulations in Sec. 5.3 was observed. The stress-strain response at $\dot{\delta} = 1 \cdot 10^{-1}$ m/s ($\dot{\varepsilon}^* = 1.67 \cdot 10^5$ s^{-1}) resembles the extension response at $\dot{\varepsilon} = 10^5$ s^{-1}. Material response softens as the loading rate $\dot{\delta}$ (and $\dot{\varepsilon}^*$) is reduced. A similar softening occurs as $\dot{\varepsilon}$ is reduced in extension testing. Additionally, similar character and periodicity in the stress-strain and dislocation behaviour was observed here as in the extension loading simulations. Most notably, ρ_{disl} decreases with increasing loading rate. Addition of dynamics in dislocation motion also reduces ρ_{disl}, as observed by [61]. Correspondingly, material response using a dynamic description of dislocation motion is harder.

During linear-elastic deformation, i.e. before the first nucleation event, displacement and stress fields is symmetric in magnitude about the line of load application (shear stress field σ_{xy} is pictured in Fig. 5.22a). Elastic fields are concentrated along the contact width at the top boundary and diminish radially. Naturally, this induces Frank-Read sources nearer the contact zone to nucleate before those further away. Dislocation nucleation localized near the indenter-film contact area generates concentrations in the stress fields, ex. σ_{xy} in Fig. 5.22b. Under sufficient load, increasingly distant sources from the contact zone are activated. In this way, a plastic front advances outwards from the contact zone. The asymmetry of the stress concentrations is due the random arrangement of Frank-Read sources, obstacles, and dislocations along the predefined slip planes, as well as the interactions of asymmetric wave patterns. The localization of shear stress at the contact zone transitions to bands of shear stress concentrations along dislocation slip planes (Fig. 5.22c).

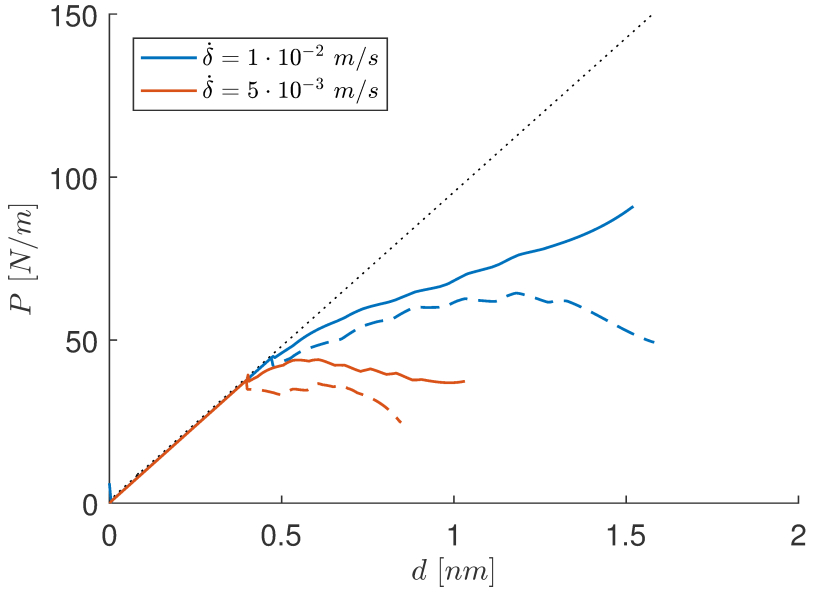

(a)

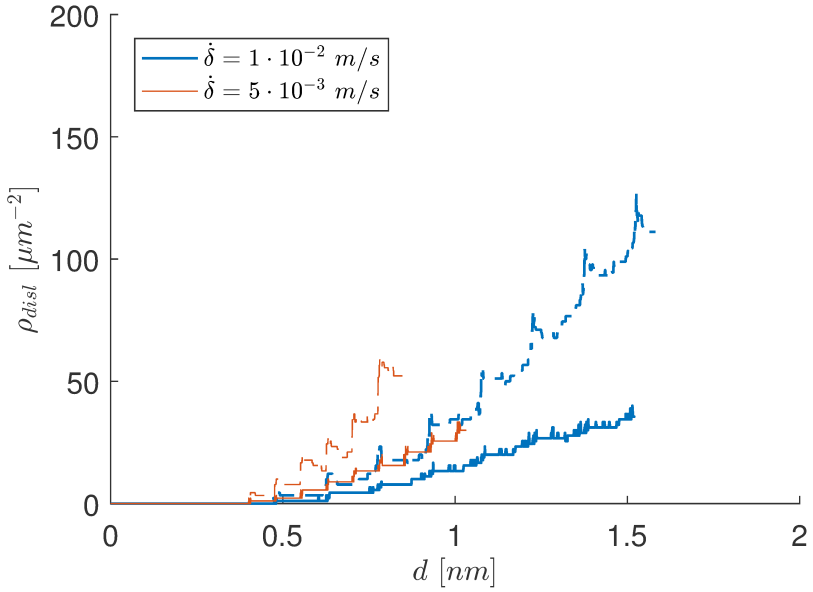

(b)

Figure 5.20: Nano-indentation simulation response at $\dot{\delta} = 5 \cdot 10^{-3}$ and $1 \cdot 10^{-2}\ m/s$ (a) Load versus indentation depth; and (b) Active dislocation density versus indentation depth. Dashed lines denote the solution resolved with quasi-static dislocation motion.

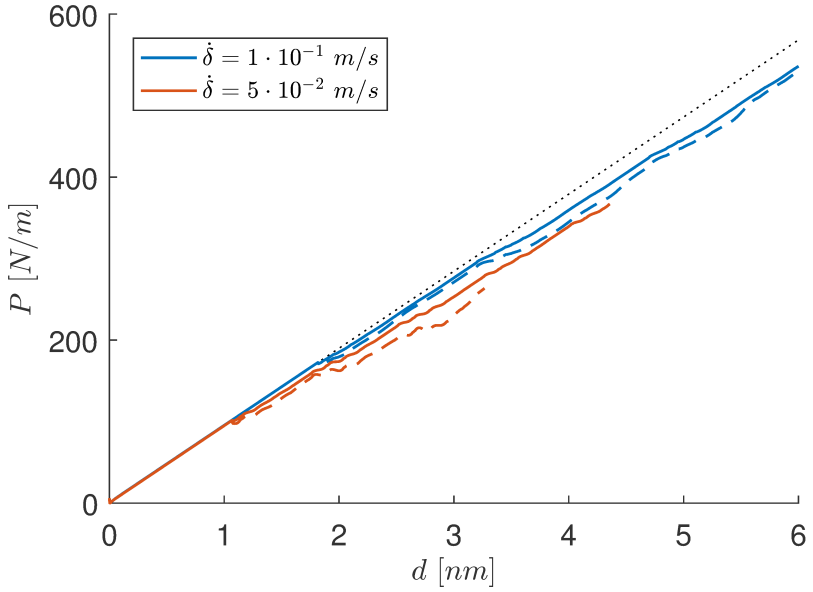

(a)

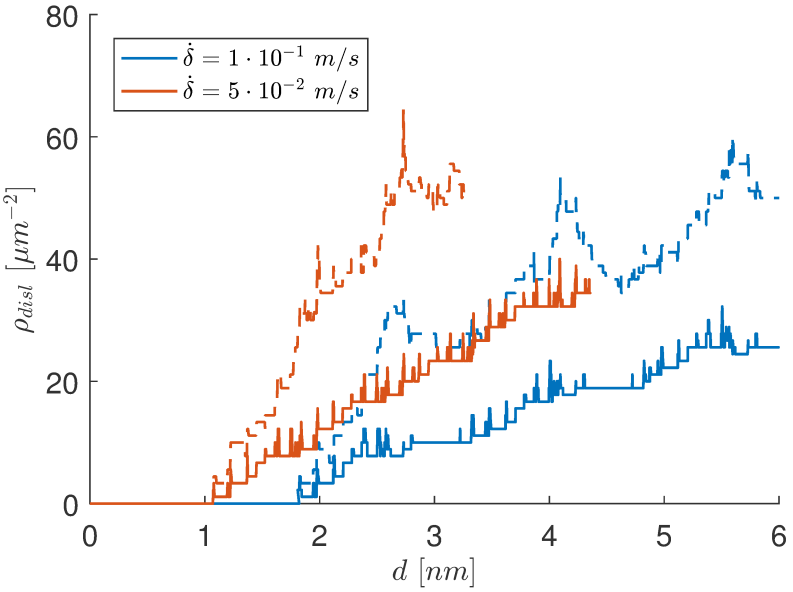

(b)

Figure 5.21: Nano-indentation simulation response at $\dot{\delta} = 5 \cdot 10^{-2}$ and $1 \cdot 10^{-1}\ m/s$ (a) Load versus indentation depth; and (b) Active dislocation density versus indentation depth. Dashed lines denote the solution resolved with quasi-static dislocation motion.

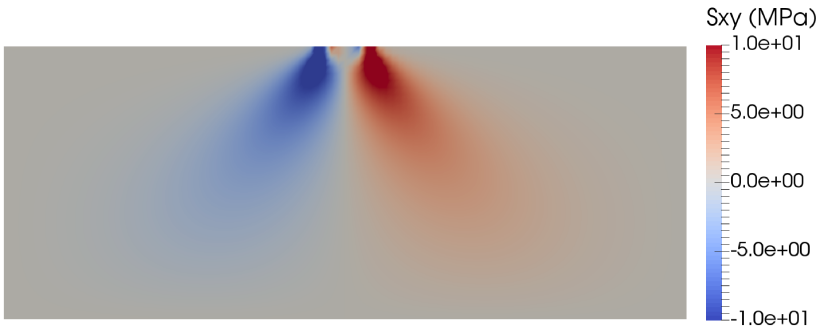

(a)

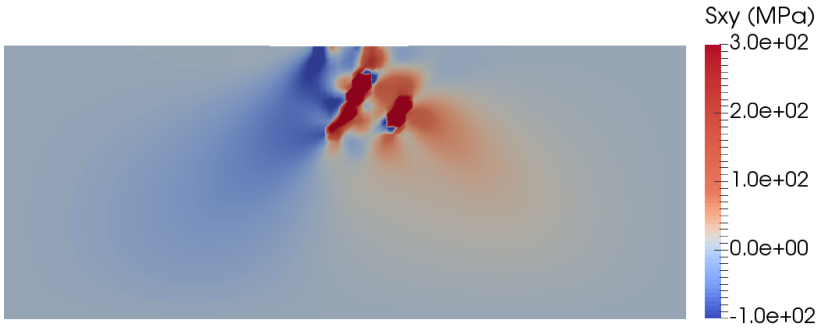

(b)

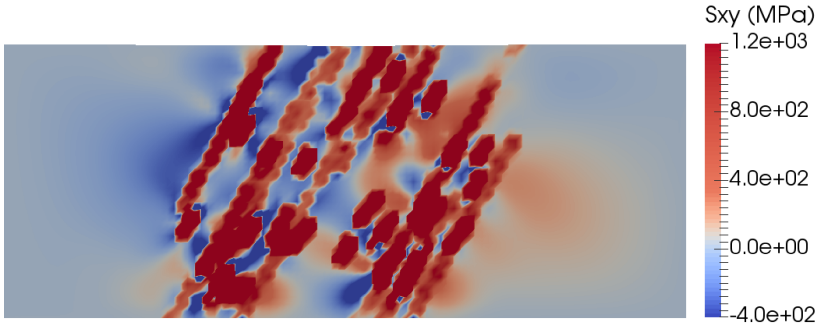

(c)

Figure 5.22: Shear stress field (σ_{xy}) of nano-indentation simulation at $\dot{\delta} = 1 \cdot 10^{-2}\ m/s$ at (a) elastic deformation, (b) first nucleation and onset of plasticity, (c) plastic deformation.

Chapter 6

Conclusion and Future Research

In this chapter, a summary of the developed DTM-DD model and the main conclusions drawn from simulation results are presented, which represent the successful completion of the research objectives for this thesis as outlined in Sec. 1.1. Recommendations are provided to address the limitations of- and extensions to the model presented in this thesis as guidance for the direction of future research.

6.1 Conclusion

The DTM-DD was developed to address two main limitations in conventional DD models. The dynamic formulation of the DTM-DD has the ability to capture the inertial effects which are particularly relevant to high loading rates; and the thermo-coupled formulation, localized thermal effects. Using the DTM-DD, the influence of thermal and inertial effects on high strain-rate plastic behaviour of metals was investigated at the mesoscale.

1. Formulation and development of the DTM-DD

The initial boundary value problem which describes the fully dynamic thermo-mechanically coupled system was formulated. Relevant mechanical, thermal, coupled thermo-mechanical constitutive relationships and boundary conditions were identified. The discrete form was then derived using the eXtended Finite Element Method. A collection of edge dislocations in the continuum was considered based on the Volterra description of the dislocation. The fully Dynamic coupled Thermo-Mechanical Dislocation Dynamics Model (DTM-DD) was

implemented in MATLAB^{TM} using a sequential solution strategy.

2. Formulation and development of dislocation mechanisms for the DTM-DD

As part of the DD family of models, dislocation behaviour is explicitly simulated in the DTM-DD. A planar simplification of the physical system reduced the scope of simulatable types of dislocations and dislocation interactions. A set of dislocation mechanisms was developed to characterize and regulate the behaviour of a collection of edge dislocations in a continuum. Dislocations were assumed to nucleate from Frank-Read type sources via a temperature-dependent nucleation process. The motion of a dislocation was characterized as fully dynamic to capture inertial effects. Motion of a dislocation is induced by the Peach-Koehler force, and governed by a velocity-dependent effective mass and a temperature-dependent viscous drag. Dislocations were characterized as independent moving heat sources based on its work done. Dislocation interactions were implemented which include: (1) annihilation of dislocation dipoles, and (2) formation of pile-ups against obstacles. A sequential solution scheme was adopted to resolve dislocation motion and interactions in parallel to the thermo-mechanically coupled domain response.

3. Utilize the DTM-DD to investigate thermal and inertial effects on high strain-rate material behaviour

The developed DTM-DD was utilized to investigate the influence of thermal and inertial effects on the high strain-rate plastic behaviour of metallic solids. The elastodynamic formulation of the DTM-DD allows for externally-induced and dislocation-generated wave behaviour to be captured in simulation. The interaction of dislocation-generated elastic waves was studied through an example of thermally-induced dislocation nucleation. Spurious oscillations due to Gibb's phenomenon and significant interference patterning was observed. The dynamic formulation of dislocation motion allows for the rise time in velocity to be captured in simulation. The impact of dynamic dislocation motion with respect to strain-rate was investigated. A limit for the simulation time step size was obtained for the convergence of dynamic dislocation motion. The sensitivity of dislocation parameters to strain-rate and temperature dependence was studied through parameter studies in the framework of extension load testing. In particular, the effect of thermal boundary conditions, inertia, and the temperature dependence of dislocation drag and nucleation strength was investigated. Finally, the DTM-DD was extended to investigate loading rate effects through the simulation of the nano-indentation of a thin film: dislocation behaviour and nucleation under contact-induced loading was studied. Ultimately, the interplay between thermal and inertial factors form a highly complex system due to opposing effects

on material behaviour.

6.2 Recommendations

One of the greatest challenges in materials simulation is the development of a constitutive model with the ability to accurately depict material response for any loading scenario and boundary conditions. Although the research presented in this thesis focuses on material response in the strain-rate regime from 10^3 to 10^5 s^{-1}, a clear direction for future research is to extend the range of investigated strain-rates.

As with other numerical studies, the comparison of numerical trends from the DTM-DD to experimental results poses a significant challenge [101]. So-called high-rate experimental tests are at $\dot{\varepsilon} = 10^3$ s^{-1} which is at the low end of mesoscale simulation rates. The current implementation of the DTM-DD uses an explicit solution strategy to determine the response of the coupled thermo-mechanical domain as well as to resolve dynamic dislocation motion. As such, simulation time step is strictly restricted for system stability and for the convergence of dislocation motion. In this way, using the DTM-DD to simulate at lower rates, i.e. sub-10^4 s^{-1}, is particularly challenging with respect to computational tractability. Consequently in future research, it is particularly desirable to address computational savings through improvements of the solution scheme and other methods of increasing computation efficiency. For example, an implicit solution strategy may be adopted to reduce limitations on the size of time steps; or computational parallelization may be explored. In this way, it will be possible to extend the current investigation to survey a fully comprehensive range of strain-rates.

Dislocation behaviour in the DTM-DD is regulated by the set of key mechanisms described in Ch. 4. The DTM-DD may be further refined with respect to dislocation behaviour through the development of subroutines to increase the complexity and robustness of the depiction of dislocation behaviour.

Furthermore, existing dislocation parameters can be refined and updated based on emerging trends from new research. Currently, the implementation of temperature dependence in the DTM-DD is limited to only two dislocation parameters: drag B and nucleation strength τ_{nuc}^{FR}. Realistically, most dislocation and material parameters in a thermo-mechanical model exhibit temperature dependence, for example, t_{nuc}, t_{pile}, k, α, among others. The temperature dependence of many of these dislocation and material parameters were neglected in the research presented in this thesis because the dependence is either weak, or as in most cases, there exists a lot of uncertainty regarding the exact nature of the temperature dependence. As the next step, a linear relationship to temperature, similar to that for viscous

drag (i.e. (4.18)), may be established for these parameters and implemented in the DTM-DD. Then, these relationships may be studied in isolation via parameter studies similar to those presented in Ch. 5, and be further refined using a higher-order approximation.

However, the greatest limitation of the DTM-DD in its current state is its two-dimensional implementation. Like other two-dimensional models, the DTM-DD is a useful tool to explore the qualitative trends in material behaviour. Inherently, the simplification to two-dimensions reduces the scope of applicable dislocation mechanisms and the complexity of their implementation which affects the quantitative accuracy of simulation results. In reality, dislocations exist in three-dimensions. It logically follows that a model which explicitly simulates dislocation evolution should be in three-dimensions to maximize realism and accuracy. Thus, the highest priority in future research is to extend the DTM-DD to a fully three-dimensional form.

References

[1] N. Marzari, "Materials modelling: The frontiers and the challenges," *Nature Materials*, vol. 15, pp. 381–382, Apr. 2016.

[2] M. Gad-el Hak, *The MEMS Handbook*. CRC Press, Sept. 2001.

[3] P. S. Peercy, "The drive to miniaturization," *Nature*, vol. 406, no. 6799, pp. 1023–1026, 2000.

[4] P. A. Kelly, "Solid Mechanics Part III: Engineering Solid Mechanics - small strain," Apr. 2015.

[5] J. P. Hirth and J. Lothe, *Theory of Dislocations*. John Wiley & Sons, 1982.

[6] O. Skiba, *Multiphysical dislocation dynamics models for high strain rate plastic deformation*. PhD thesis, 2015.

[7] E. Van der Giessen, "Multiscale Plasticity: Reduction or Emergence?," *Procedia IUTAM*, vol. 10, pp. 442–446, 2014.

[8] E. Van der Giessen, "Plasticity in the 21st century," in *Mechanics for a New Mellennium*, pp. 413–428, Springer, 2001.

[9] O. Cazacu, *Multiscale modeling of heterogenous materials*. Wiley-ISTE, 2010.

[10] B. Gurrutxaga-Lerma, D. S. Balint, D. Dini, D. E. Eakins, and A. P. Sutton, "Dynamic Discrete Dislocation Plasticity," in *Advances in Applied Mechanics*, vol. 47, Academic Press, Nov. 2014.

[11] P. S. Follansbee, G. Regazzoni, and U. F. Kocks, "The transition to drag controlled deformation in copper at high strain rates," in *Third international conference on mechanical properties of materials at high strain rates* (J. Harding, ed.), vol. 3 of

Conference series (Institute of Physics (Great Britain)) ; no. 21, 47, 70, (London), pp. 71–80, Institute of Physics, 1984.

[12] G. Regazzoni, U. F. Kocks, and P. S. Follansbee, "Dislocation kinetics at high strain rates," *Acta Metallurgica*, vol. 35, pp. 2865–2875, Dec. 1987.

[13] A. Roos, J. T. M. De Hosson, and E. Van der Giessen, "High-speed dislocations in high strain-rate deformations," *Computational Materials Science*, vol. 20, pp. 19–27, Jan. 2001.

[14] M. A. Shehadeh, H. M. Zbib, and T. Diaz de la Rubia, "Modelling the dynamic deformation and patterning in fcc single crystals at high strain rates: dislocation dynamics plasticity analysis," *Philosophical Magazine*, vol. 85, pp. 1667–1685, May 2005.

[15] B. Gurrutxaga-Lerma, D. S. Balint, D. Dini, D. E. Eakins, and A. P. Sutton, "A dynamic discrete dislocation plasticity method for the simulation of plastic relaxation under shock loading," *Proc. R. Soc. A*, vol. 469, p. 20130141, Aug. 2013.

[16] J. Weertman and J. R. Weertman, *Elementary Dislocation Theory*. New York: Oxford University Press, Nov. 1990.

[17] N. M. Ghoniem, S.-H. Tong, and L. Z. Sun, "Parametric dislocation dynamics: a thermodynamics-based approach to investigations of mesoscopic plastic deformation," *Physical Review B*, vol. 61, no. 2, p. 913, 2000.

[18] J. R. Hook and H. E. Hall, *Solid State Physics*. Chichester ; New York: Wiley, 2 edition ed., July 1995.

[19] V. Volterra, "On the equilibrium of multiply-connected elastic bodies," *Ann. Ec. Norm*, vol. 24, no. 3, pp. 401–517, 1907.

[20] G. I. Taylor, "The Mechanism of Plastic Deformation of Crystals. Part I. Theoretical," *Proceedings of the Royal Society of London. Series A, Containing Papers of a Mathematical and Physical Character*, vol. 145, no. 855, pp. 362–387, 1934.

[21] E. Orowan, "Zur Kristallplastizitt. I," *Zeitschrift fr Physik*, vol. 89, pp. 605–613, Sept. 1934.

[22] E. Orowan, "Zur Kristallplastizitt. II," *Zeitschrift fr Physik*, vol. 89, pp. 614–633, Sept. 1934.

[23] E. Orowan, "Zur Kristallplastizitt. III," *Zeitschrift fr Physik*, vol. 89, pp. 634–659, Sept. 1934.

[24] M. Polanyi, "ber eine Art Gitterstrung, die einen Kristall plastisch machen knnte," *Zeitschrift fr Physik*, vol. 89, pp. 660–664, Sept. 1934.

[25] D. Hull and D. J. Bacon, *Introduction to Dislocations*. Butterworth-Heinemann, July 2001.

[26] J. Weertman, *Dislocation Based Fracture Mechanics*. World Scientific, Jan. 1996.

[27] E. Van der Giessen and A. Needleman, "Discrete dislocation plasticity: a simple planar model," *Modelling and Simulation in Materials Science and Engineering*, vol. 3, no. 5, p. 689, 1995.

[28] NDT Education Resource Center, "Dislocation direction."

[29] E. Schmid and W. Boas, "Plasticity of crystals," 1950.

[30] A. Arsenlis, W. Cai, M. Tang, M. Rhee, T. Oppelstrup, G. Hommes, T. G. Pierce, and V. V. Bulatov, "Enabling strain hardening simulations with dislocation dynamics," *Modelling and Simulation in Materials Science and Engineering*, vol. 15, no. 6, p. 553, 2007.

[31] B. Devincre and L. P. Kubin, "Mesoscopic simulations of dislocations and plasticity," *Materials Science and Engineering: A*, vol. 234, pp. 8–14, Aug. 1997.

[32] K. W. Schwarz, "Simulation of dislocations on the mesoscopic scale. I. Methods and examples," *Journal of Applied Physics*, vol. 85, pp. 108–119, Jan. 1999.

[33] H. M. Zbib, M. Rhee, and J. P. Hirth, "On plastic deformation and the dynamics of 3d dislocations," *International Journal of Mechanical Sciences*, vol. 40, pp. 113–127, Feb. 1998.

[34] S. S. Shishvan, S. Mohammadi, and M. Rahimian, "A dislocation-dynamics-based derivation of the FrankRead source characteristics for discrete dislocation plasticity," *Modelling and Simulation in Materials Science and Engineering*, vol. 16, no. 7, p. 075002, 2008.

[35] R. J. Amodeo and N. M. Ghoniem, "Dislocation dynamics. I. A proposed methodology for deformation micromechanics," *Physical Review B*, vol. 41, pp. 6958–6967, Apr. 1990.

[36] A. N. Gulluoglu and C. S. Hartley, "Simulation of dislocation microstructures in two dimensions. I. Relaxed structures," *Modelling and Simulation in Materials Science and Engineering*, vol. 1, no. 1, p. 1, 1992.

[37] A. N. Gulluoglu and C. S. Hartley, "Simulation of dislocation microstructures in two dimensions. II. Dynamic and relaxed structures," *Modelling and Simulation in Materials Science and Engineering*, vol. 1, no. 4, p. 383, 1993.

[38] L. Kubin and G. Canova, "The modelling of dislocation patterns," *Scripta Metallurgica et Materiala*, vol. 27, no. 8, pp. 957–962, 1992.

[39] R. Gracie and T. Belytschko, "An adaptive concurrent multiscale method for the dynamic simulation of dislocations," *International Journal for Numerical Methods in Engineering*, vol. 86, pp. 575–597, Apr. 2011.

[40] L. P. Kubin, G. Canova, M. Condat, B. Devincre, V. Pontikis, and Y. Brchet, "Dislocation Microstructures and Plastic Flow: A 3d Simulation," *Solid State Phenomena*, vol. 23-24, pp. 455–472, 1992.

[41] T. Belytschko and R. Gracie, "On XFEM applications to dislocations and interfaces," *International Journal of Plasticity*, vol. 23, pp. 1721–1738, Oct. 2007.

[42] R. Gracie, G. Ventura, and T. Belytschko, "A new fast finite element method for dislocations based on interior discontinuities," vol. 69, pp. 423–441, Jan. 2007.

[43] N. M. Ghoniem and X. Han, "Dislocation motion in anisotropic multilayer materials," *Philosophical Magazine*, vol. 85, pp. 2809–2830, Aug. 2005.

[44] X. Han and N. M. Ghoniem, "Stress field and interaction forces of dislocations in anisotropic multilayer thin films," *Philosophical Magazine*, vol. 85, pp. 1205–1225, Apr. 2005.

[45] X. Han, N. M. Ghoniem, and Z. Wang, "Parametric dislocation dynamics of anisotropic crystals," *Philosophical Magazine*, vol. 83, pp. 3705–3721, Oct. 2003.

[46] M. Rhee, J. S. Stolken, V. V. Bulatov, T. M. de la Rubia, H. M. Zbib, and J. P. Hirth, "Dislocation stress fields for dynamic codes using anisotropic elasticity: methodology and analysis," *Materials Science and Engineering: A*, vol. 309310, pp. 288–293, July 2001.

[47] V. Bulatov and W. Cai, *Computer Simulations of Dislocations*. OUP Oxford, Nov. 2006.

[48] T. Belytschko and T. Black, "Elastic crack growth in finite elements with minimal remeshing," *International Journal for Numerical Methods in Engineering*, vol. 45, pp. 601–620, June 1999.

[49] N. Mos, J. Dolbow, and T. Belytschko, "A finite element method for crack growth without remeshing," *International Journal for Numerical Methods in Engineering*, vol. 46, pp. 131–150, Sept. 1999.

[50] N. Sukumar, N. Mos, B. Moran, and T. Belytschko, "Extended finite element method for three-dimensional crack modelling," *International Journal for Numerical Methods in Engineering*, vol. 48, pp. 1549–1570, Aug. 2000.

[51] N. Mos and T. Belytschko, "Extended finite element method for cohesive crack growth," *Engineering fracture mechanics*, vol. 69, no. 7, pp. 813–833, 2002.

[52] J.-H. Song, P. M. A. Areias, and T. Belytschko, "A method for dynamic crack and shear band propagation with phantom nodes," *International Journal for Numerical Methods in Engineering*, vol. 67, pp. 868–893, Aug. 2006.

[53] A. R. Khoei, *Extended finite element method: theory and applications.* Chichester, West Sussex: John Wiley & Sons, Inc, 2015.

[54] I. Babuska and J. M. Melenk, "The Partition of Unity Method," *International Journal of Numerical Methods in Engineering*, vol. 40, pp. 727–758, 1996.

[55] J. D. Eshelby, "The Force on an Elastic Singularity," *Philosophical Transactions of the Royal Society of London A: Mathematical, Physical and Engineering Sciences*, vol. 244, pp. 87–112, Nov. 1951.

[56] G. Ventura, B. Moran, and T. Belytschko, "Dislocations by partition of unity," *International Journal for Numerical Methods in Engineering*, vol. 62, pp. 1463–1487, Mar. 2005.

[57] R. Gracie, J. Oswald, and T. Belytschko, "On a new extended finite element method for dislocations: Core enrichment and nonlinear formulation," *Journal of the Mechanics and Physics of Solids*, vol. 56, pp. 200–214, Jan. 2008.

[58] G. Ventura, R. Gracie, and T. Belytschko, "Fast integration and weight function blending in the extended finite element method," *International Journal for Numerical Methods in Engineering*, vol. 77, pp. 1–29, Jan. 2009.

[59] T. Belytschko, N. Mos, S. Usui, and C. Parimi, "Arbitrary discontinuities in finite elements," *International Journal for Numerical Methods in Engineering*, vol. 50, pp. 993–1013, Feb. 2001.

[60] J. S. Langer, E. Bouchbinder, and T. Lookman, "Thermodynamic theory of dislocation-mediated plasticity," *Acta Materialia*, vol. 58, pp. 3718–3732, June 2010.

[61] Z. Q. Wang, I. J. Beyerlein, and R. Lesar, "Dislocation motion in high strain-rate deformation," *Philosophical Magazine*, vol. 87, pp. 2263–2279, June 2007.

[62] R. W. Armstrong and S. M. Walley, "High strain rate properties of metals and alloys," *International Materials Reviews*, vol. 53, pp. 105–128, May 2008.

[63] Y. Fan, Y. N. Osetsky, S. Yip, and B. Yildiz, "Onset Mechanism of Strain-Rate-Induced Flow Stress Upturn," *Physical Review Letters*, vol. 109, p. 135503, Sept. 2012.

[64] P. Agnihotri and E. Van der Giessen, "Rate sensitivity according to discrete dislocation plasticity," in *6th International Conference on Multiscale Materials Modeling (MMM12)*, (Bipolis, Singapore), pp. 15–19, Oct. 2012.

[65] S. N. Medyanik, W. K. Liu, and S. Li, "On criteria for dynamic adiabatic shear band propagation," *Journal of the Mechanics and Physics of Solids*, vol. 55, pp. 1439–1461, July 2007.

[66] N. Ranc, L. Taravella, V. Pina, and P. Herve, "Temperature field measurement in titanium alloy during high strain rate loadingAdiabatic shear bands phenomenon," *Mechanics of Materials*, vol. 40, pp. 255–270, Apr. 2008.

[67] T. Belytschko, B. Moran, and M. Kulkarni, "On the Crucial Role of Imperfections in Quasi-static Viscoplastic Solutions," *Journal of Applied Mechanics*, vol. 58, pp. 658–665, Sept. 1991.

[68] J. Crank, "A practical method for numerical evaluation of solutions of partial differential equations of the heat-conduction type," *Advances in Computational Mathematics*, vol. 6, pp. 207–226, Dec. 1996.

[69] T. J. R. Hughes, *The Finite Element Method: Linear Static and Dynamic Finite Element Analysis*. Courier Corporation, May 2012.

[70] P. S. Follansbee and U. F. Kocks, "A constitutive description of the deformation of copper based on the use of the mechanical threshold stress as an internal state variable," *Acta Metallurgica*, vol. 36, pp. 81–93, Jan. 1988.

[71] G. P. Cherepanov, "Crack propagation in continuous media," *Journal of Applied Mathematics and Mechanics*, vol. 31, pp. 503–512, Jan. 1967.

[72] J. R. Rice, "Tensile crack tip fields in elastic-ideally plastic crystals," *Mechanics of Materials*, vol. 6, no. 4, pp. 317–335, 1987.

[73] K. Kishimoto, S. Aoki, and M. Sakata, "On the path independent integral-J," *Engineering Fracture Mechanics*, vol. 13, no. 4, pp. 841–850, 1980.

[74] J. P. Hirth, H. M. Zbib, and J. Lothe, "Forces on high velocity dislocations," *Modelling and Simulation in Materials Science and Engineering*, vol. 6, no. 2, p. 165, 1998.

[75] K. M. Jassby and T. Vreeland, "An experimental study of the mobility of edge dislocations in pure copper single crystals," *Philosophical Magazine*, vol. 21, pp. 1147–1168, June 1970.

[76] F. R. N. Nabarro, *Theory of crystal dislocations*. Clarendon Pr., 1967.

[77] J. A. Gorman, D. S. Wood, and T. Vreeland, "Mobility of Dislocations in Aluminum," *Journal of Applied Physics*, vol. 40, pp. 833–841, Feb. 1969.

[78] W. P. Mason and A. Rosenberg, "Phonon and electron drag coefficients in single-crystal aluminum," *Physical Review*, vol. 151, no. 2, p. 434, 1966.

[79] W. P. Mason, "Dislocation Dynamics," (Seattale and Harrison), p. 487, McGraw-Hill New York, 1967.

[80] W. D. Sylwestrowicz, "Mechanism of Ultrasonic Loss in Silicon and Aluminum," *Journal of Applied Physics*, vol. 37, pp. 535–541, Feb. 1966.

[81] T. S. Hutchison and D. H. Rogers, "Ultrasonic Damping at Kilocycle Frequencies in Aluminum at Low Temperatures," *Journal of Applied Physics*, vol. 33, pp. 792–799, Mar. 1962.

[82] G. A. Alers and D. O. Thompson, "Dislocation Contributions to the Modulus and Damping in Copper at Megacycle Frequencies," *Journal of Applied Physics*, vol. 32, pp. 283–293, Feb. 1961.

[83] A. Kumar and R. G. Kumble, "Viscous Drag on Dislocations at High Strain Rates in Copper," *Journal of Applied Physics*, vol. 40, pp. 3475–3480, Aug. 1969.

[84] W. G. Ferguson, A. Kumar, and J. E. Dorn, "Dislocation Damping in Aluminum at High Strain Rates," *Journal of Applied Physics*, vol. 38, pp. 1863–1869, Mar. 1967.

[85] N. Nagata and S. Yoshida, "Deformation of Copper Single Crystals and Polycrystals at High Strain Rates," *Transactions of the Japan Institute of Metals*, vol. 13, no. 5, pp. 332–338, 1972.

[86] E. Nadgornyi, "Dislocation dynamics and mechanical properties of crystals," *Progress in Materials Science*, vol. 31, pp. 1–530, Jan. 1988.

[87] K. M. Jassby and T. Vreeland, "Dislocation mobility in copper and zinc at 44 K," *Scripta Metallurgica*, vol. 5, no. 11, pp. 1007–1011, 1971.

[88] V. R. Parameswaran, N. Urabe, and J. Weertman, "Dislocation Mobility in Aluminum," *Journal of Applied Physics*, vol. 43, pp. 2982–2986, July 1972.

[89] A. Hikata, R. A. Johnson, and C. Elbaum, "Interaction of Dislocations with Electrons and with Phonons," *Physical Review B*, vol. 2, no. 12, p. 4856, 1970.

[90] A. Hikata, R. A. Johnson, and C. Elbaum, "Interaction of Dislocations with Electrons and with Phonons," *Physical Review B*, vol. 4, pp. 674–674, July 1971.

[91] D. L. Olmsted, L. G. HectorJr, W. A. Curtin, and R. J. Clifton, "Atomistic simulations of dislocation mobility in Al, Ni and Al/Mg alloys," *Modelling and Simulation in Materials Science and Engineering*, vol. 13, pp. 371–388, Apr. 2005.

[92] J. A. Gorman, D. S. Wood, and T. Vreeland, "Mobility of dislocations in aluminum at 74 and 83K," *Journal of Applied Physics*, vol. 40, pp. 903–904, Feb. 1969.

[93] T. Vreeland, "Dislocation drag in close-packed metals," *Scripta metallurgica*, vol. 18, no. 7, pp. 645–651, 1984.

[94] D. S. Balint, V. S. Deshpande, A. Needleman, and E. Van der Giessen, "Size effects in uniaxial deformation of single and polycrystals: a discrete dislocation plasticity analysis," *Modelling and Simulation in Materials Science and Engineering*, vol. 14, pp. 409–422, Apr. 2006.

[95] P. Rosakis, A. J. Rosakis, G. Ravichandran, and J. Hodowany, "A thermodynamic internal variable model for the partition of plastic work into heat and stored energy in metals," *Journal of the Mechanics and Physics of Solids*, vol. 48, pp. 581–607, Mar. 2000.

[96] R. Kapoor and S. Nemat-Nasser, "Determination of temperature rise during high strain rate deformation," *Mechanics of Materials*, vol. 27, pp. 1–12, Jan. 1998.

[97] A. Needleman and V. Tvergaard, "Analysis of a brittle-ductile transition under dynamic shear loading," *International Journal of Solids and Structures*, vol. 32, pp. 2571–2590, Sept. 1995.

[98] W. D. Jenkins, T. G. Digges, and C. R. Johnson, "Tensile Properties of Copper, Nickel, and 70-Percent-Copper-30-Percent-Nickel and 30-Percent-Copper-70-Percent-Nickel Alloys at High Temperatures," *Journal of Research of the National Bureau of Standards*, vol. 58, pp. 201–211, Apr. 1957.

[99] S. J. Zinkle and W. S. Eatherly, "Effect of Test Temperature and Strain Rate on the Tensile Properties of High-Strength, High-Conductivity Copper Alloys," Tech. Rep. DOE/ER–0313/21, Oak Ridge National Lab., TN (United States), Apr. 1997.

[100] B. N. Singh, D. J. Edwards, M. Eldrup, and P. Toft, "Effects of heat treatments and neutron irradiation on microstructures and physical and mechanical properties of copper alloys," *Journal of Nuclear Materials*, vol. 249, pp. 1–16, Sept. 1997.

[101] S. Ryu, K. Kang, and W. Cai, "Entropic effect on the rate of dislocation nucleation," *Proceedings of the National Academy of Sciences*, vol. 108, pp. 5174–5178, Mar. 2011.

[102] V. S. Deshpande, A. Needleman, and E. Van der Giessen, "Plasticity size effects in tension and compression of single crystals," *Journal of the Mechanics and Physics of Solids*, vol. 53, pp. 2661–2691, Dec. 2005.

[103] S. S. Shishvan and E. Van der Giessen, "Distribution of dislocation source length and the size dependent yield strength in freestanding thin films," *Journal of the Mechanics and Physics of Solids*, vol. 58, pp. 678–695, May 2010.

[104] P. Agnihotri and E. Van der Giessen, "On the rate sensitivity in discrete dislocation plasticity," *Mechanics of Materials*, vol. 90, pp. 37–46, Nov. 2015.

[105] H. H. M. Cleveringa, E. Van der Giessen, and A. Needleman, "A discrete dislocation analysis of bending," *International Journal of Plasticity*, vol. 15, no. 8, pp. 837–868, 1999.

[106] M. Komijani and R. Gracie, "An enriched finite element model for wave propagation in fractured media," *Finite Elements in Analysis and Design*, vol. 125, pp. 14–23, Mar. 2017.

[107] S. Suresh, T.-G. Nieh, and B. W. Choi, "Nano-indentation of copper thin films on silicon substrates," *Scripta Materialia*, vol. 41, pp. 951–957, Aug. 1999.

[108] A. C. Fischer-Cripps, "Nanoindentation Testing," in *Nanoindentation* (F. L. Frederick, W. O. Winer, A. E. Bergles, G. A. Klutke, K. K. Wang, I. Finnie, J. R. Welty, M. D. Bryant, H. T. Yang, V. C. Mow, F. A. Leckie, and D. Gross, eds.), pp. 21–37, New York, NY: Springer New York, 2011.

[109] W. Zielinski, H. Huang, S. Venkataraman, and W. W. Gerberich, "Dislocation distribution under a microindentation into an iron-silicon single crystal," *Philosophical Magazine A*, vol. 72, pp. 1221–1237, Nov. 1995.

[110] S. G. Corcoran, R. J. Colton, E. T. Lilleodden, and W. W. Gerberich, "Anomalous plastic deformation at surfaces: Nanoindentation of gold single crystals," *Physical Review B*, vol. 55, pp. R16057–R16060, June 1997.

[111] T. W. Wu, C. Hwang, J. Lo, and P. Alexopoulos, "Microhardness and microstructure of ion-beam-sputtered, nitrogen-doped NiFe films," *Thin Solid Films*, vol. 166, pp. 299–308, Dec. 1988.

[112] W. W. Gerberich, S. K. Venkataraman, H. Huang, S. E. Harvey, and D. L. Kohlstedt, "The injection of plasticity by millinewton contacts," *Acta Metallurgica et Materialia*, vol. 43, pp. 1569–1576, Apr. 1995.

[113] J. A. Williams and R. Dwyer Joyce, "Contact mechanics," in *A Handbook on Modern Tribology*, CRC Publications, Dec. 2000.